Development of functional optical coherence tomography (fOCT) for monitoring environmental effects on plants

(植物への環境影響モニタリングのための機能的 OCT の開発)

２０１５年３月

埼玉大学大学院理工学研究科（博士後期課程）

理工学専攻（主指導教員　門野　博史）

LIYANAARACHCHI KANKANAMGE THANUJA SRIMAL

Development of functional optical coherence tomography (fOCT) for monitoring environmental effects on plants

植物への環境影響モニタリングのための機能的OCTの開発

A thesis submitted in fulfillment of the requirements for the degree
of Doctor of Philosophy in
Environmental Science and Infrastructure Engineering

LIYANAARACHCHI KANKANAMGE THANUJA SRIMAL

11DE058

Supervisors: Prof. Hirofumi Kadono
               Assoc. Prof. Makato Miwa
               Assoc. Prof. Nobukazu Yoshikawa

Optical Sensing Laboratory
Graduate School of Science and Engineering
Saitama University
Saitama - Japan

ACKNOWLEDGEMENTS

I would like to thank my parents, wife, and son for the persistent encouragement given to me, to make this project a success. Eventually I may be pardon if I have inadvertently omitted the names of others to who my thanks are due.

TABLE OF CONTENT

V

TABLE OF FIGURES

X

CHAPTER 1

1. General Introduction

1.1. Introduction

Tomographic imaging techniques such as x-ray computer tomography (CT) [1], magnetic resonance imaging (MRI) [2], and ultrasonography [3] have found widespread applications in medicine. Each of these technique measures a different physical property and has a resolution and penetration range that prove advantageous for specific applications. Optical coherence tomography (OCT) [4,5], it is possible to perform noninvasive cross-sectional imaging of internal tissue structures in biology by measuring their optical back scattering.

Table 1.1. Summary of Some commonly known tomographic methods.

Name of method	Resolution	Disadvantages
Computer Tomography **(CT)**	300~600µm	Harmful radiation resolution is not enough
Magnetic resonance Imaging **(MRI)**	800µm	Expensive, resolution not enough
Ultrasonography	10~500µm	Contact method
Confocal Laser Scanning Microscopy **(CLSM)**	1µm	Very limited penetration
Optical coherence tomography **(OCT)**	1~20 µm	Limited penetration

Both low-coherence light and ultrashort laser pulses can be used to measure internal structure in biological samples. An optical signal that is scattered through or reflected from a biological tissue will contain time-of-flight information, which in turn yields spatial information about tissue microstructure. Time-resolved transmission spectroscopy has been used to measure absorption and scattering properties in tissues and has been demonstrated as a noninvasive diagnostic measure of hemoglobin oxygenation in the brain [6]. Optical ranging measurements of microstructure have been performed in the eye and the skin with femtosecond laser pulses [7]. Time gating by means of coherent [8] as well as noncoherent [9] techniques has been used to preferentially detect directly transmitted light and obtain transmission images in turbid tissue. Low-coherence reflectometry has been used for ranging measurements in optical components [10,11], for surface contour mapping in integrated circuits [12], and for ranging measurements in the retina [13,14] and other eye structures [15,16].
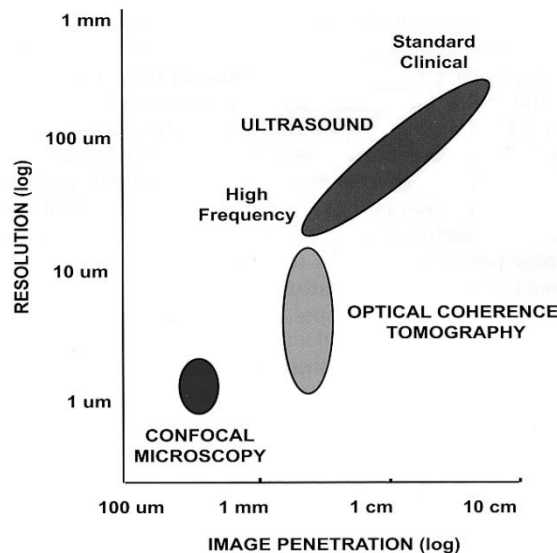
Figure 1.1. Resolution vs. Image penetration in common tomographyic methods.

In contrast to time domain techniques, low coherence reflectometry can be performed with continuous-wave light without the need for ultrashort pulse laser sources. Furthermore, recent technological advances in low-coherence reflectometry have allowed the construction of compact and modular systems that use diode light sources and fiber optics and have achieved micrometer spatial resolutions and high detection sensitivity.

In OCT, low-coherence reflectometry has been extended to obtain tomographic images of biological systems. Since low-coherence reflectometry is used, the coherence property of light reflected from a sample provides information on the time-of-flight delay from the reflective boundaries and backscattering sites in the sample. The delay information is then used to determine the longitudinal location of the reflection sites.

Light from the low coherence source is splitted into sample and reference (usually a mirror) arms. The reflected light from the sample and reference arms are combined to interfere. The electric signals detected at the photoreceiver are processed to get an A-scan, representing the depth resolved reflectance profile of the sample with the mirror in the reference arm scanning in Time Domain OCT (TD-OCT) [17]. A two-dimensional cross-sectional image of the sample, called B-scan is achieved by scanning the probing beam in the sample arm. This TD-OCT requires a mechanical scanning for A-scan. To overcome this difficulty, a spectral domain OCT (SD-OCT) [18] was proposed and is commonly used nowadays.

In SD-OCT, which is used in our study, the reference arm length is fixed at a position approximately corresponding to the probing position of the sample. The spectral interference pattern between the light returned from the reference and that from the sample is acquired by a line scan camera in a spectrometer. Finally, a depth profile of the sample is obtained by taking a

Fourier transforming the spectral interference pattern. Hence, mechanical scanning of the reference mirror can be eliminated to achieve A-scan [19].

The OCT technique has generated numerous biological applications, most commonly in the fields of ophthalmology [20,21] and dermatology [22]. The imaging depth of OCT is limited by optical absorption and scattering coefficients of the sample, and morphological features as depth as 3 mm can be imaged depending on the tissues [23]. More recently, OCT has also been used in the area of botany to visualize the inner structure of botanical samples [24,25] and to study the physiological changes in plants suffering from a pathogen attack with conventional structural OCT imaging [26].

However, its potential in monitoring functional changes, in other words, biological activities inside tissue was not well developed. Processes such as cytoplasmic steaming, organelle movement, cell growth and division, and biochemical reactions are responsible for functional changes [27].
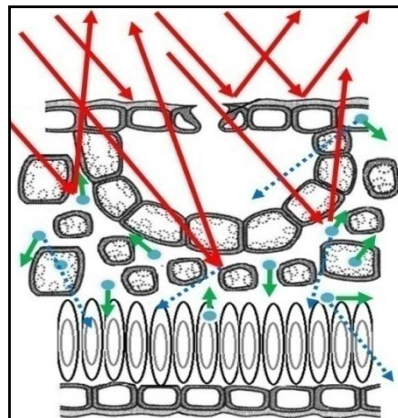
Figure 1.2. Light back reflections, back scattering, and partial scattering in a leaf sample.
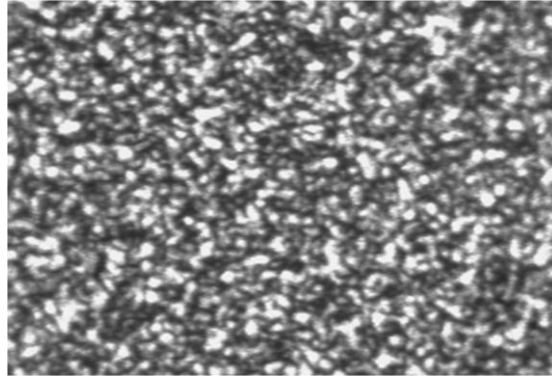
Figure 1.3. Speckle pattern when laser light illuminates a live leaf surface.

Since we wanted to monitor those functional changes, we proposed to utilize a biospeckle signal to achieve a functional OCT (fOCT) [28-31], and fOCT biospeckle imaging technique was developed and applied well in this study. Biospeckle is optical information that has been getting attention during last fifteen years for evaluation of properties of biological materials [33]. Laser speckle is a random interference pattern of backscattered light observed (Figure 1.3), for example by a CCD camera, at some distance from the illuminated object. If the sample does not show activity, the speckle pattern is stable in time. However, in the case of biological samples, the speckle pattern consists of two components: static, from non moving elements, and variable in time, from moving organelles and particles within the sample. This dynamic speckle pattern is characteristic for biological tissues and has been called a biospeckle [32]. Processes related to movements of the scattering centers in the tissue are responsible for biospeckle activities [34]. The biospeckle arising out of dynamic motion of organelles and particles (Figure 1.2) can reflect the biological activities of a living substance. Figure 1.4 shows conventional OCT cross-sectional image and Figure 1.5 shows corresponding fOCT biospeckle image of back surface of a Koshihikari rice leaf. Vain structure in more deeper area is clearly visible in biospeckle image (Figure 1.5).

5
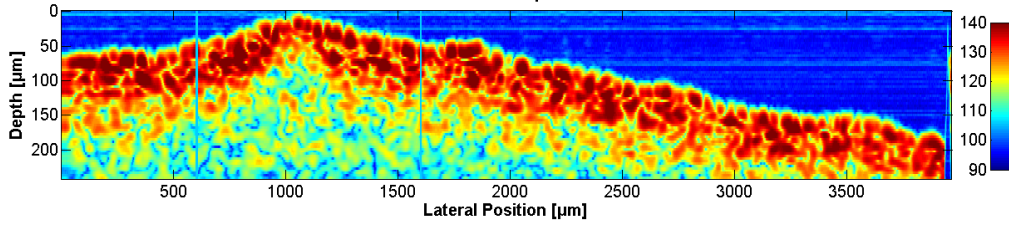
Figure 1.4. Conventional OCT cross-sectional image of back surface of Koshihikari rice leaf.
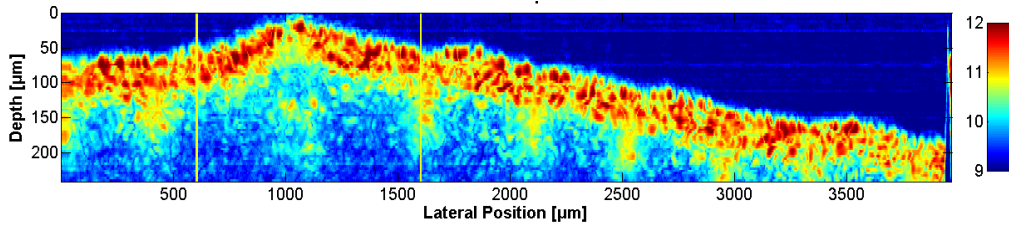
Figure 1.5. Corresponding fOCT biospeckle image of back surface of Koshihikari rice leaf.

To examine the fOCT biospeckles, OCT cross-sectional images were acquired successively at a time period (0.1 seconds). Two different approaches were employed to analyze biospeckle signals coming from different spatial positions of the OCT cross-sectional image. In first approach, magnitude of biospeckle signal, in other words, standard deviation (SD) of the signal was calculated along time axis of each spatial position from the array of OCT cross-sectional images. Then a fOCT biospeckle image was constructed from the SDs of biospeckle signals. In our second approach, temporal characteristics of the biospeckle signals were analyzed by acquiring biospeckle signals of different depth positions at fixed lateral positions. Autocorrelation functions of fOCT biospeckle signals coming from different depth positions on the plant leaf were calculated and correlation lengths (CLs) were calculated to quantify the characteristics. SD and CL of the time varying biospeckle signal were proposed as measures to evaluate the change in biological activity against ozone (O_3), and water stresses on plants.

O_3 is generally conceived as occurring only in the form of beneficial stratospheric O_3, a natural screen from the harmful effects of ultraviolet (UV) radiation. Tropospheric (ground level) O_3 is one of the major air pollutant worldwide, causing more damage to plants than all other air pollutants combined [35]. The discovery of the phytotoxicity of O_3 during the mid 1950s [36] prompted widespread studies on the effects of O_3 on plant growth and final yield. This O_3 is formed by complex photochemical reactions involving nitrogen oxides (NOx), volatile organic compounds (VOC) and carbon monoxide (CO) [37], which are called ozone precursors. Motor vehicle exhaust, industrial emissions, and chemical solvents are the major sources of these chemicals. Although these precursors often originate in urban areas, winds can carry NOx hundreds of kilometers, causing ozone formation to occur in less populated regions as well. Methane, a VOC whose atmospheric concentration has increased tremendously during the last century, contributes to ozone formation but on a global scale rather than in local or regional photochemical smog episodes. In situations where this exclusion of methane from the VOC group of substances is not obvious, the term Non-Methane VOC (NMVOC) is often used.

The chemical reactions involved in tropospheric ozone formation are a series of complex cycles in which carbon monoxide and VOCs are oxidised to water vapour and carbon dioxide. The reactions involved in this process are illustrated bellow with CO but similar reactions occur for VOC as well. The oxidation begins with the reaction of CO with the hydroxyl radical ($^{\bullet}OH$) [38]. The radical intermediate formed by this reacts rapidly with oxygen to give a peroxy radical $HO_2^{\bullet}$

$^{\bullet}OH + CO \rightarrow {}^{\bullet}HOCO$

$^{\bullet}HOCO + O_2 \rightarrow HO_2^{\bullet} + CO_2$
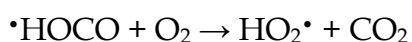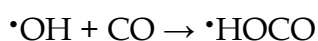
Peroxy radicals then go on to react with NO to give NO_2 which is photolysed to give atomic oxygen and through reaction with oxygen a molecule of ozone:

$$HO_2{}^\bullet + NO \rightarrow {}^\bullet OH + NO_2$$

$$NO_2 + h\nu \rightarrow NO + O(^3P)$$

$$O(^3P) + O_2 \rightarrow O_3$$
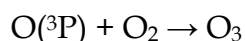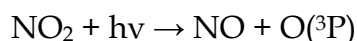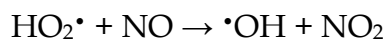
The balance of this sequence of chemical reactions is:

$$CO + 2O_2 + h\nu \rightarrow CO_2 + O_3$$

Adverse effects of elevated O_3 on agricultural crops and forest trees have been documented and results from experiments and field observations were summarized in numerous articles. In many species, elevated O_3 exposure reduces CO_2 assimilation in various ways:

- O_3 decreases stomatal conductance by affecting stomatal guard cells [39];

- O_3 reduces photosynthetic activity by reducing the levels and activity of Rubisco [40];

- O_3 leads to chloroplast degradation and accelerated leaf senescence [41]

O_3 enters the mesophyll via stomata where it immediately interacts with water and other cellular components to generate reactive oxygen species (ROS) such as superoxide radicals ($O_2{}^-$), hydroxyl radicals (OH^-), and hydrogen peroxide (H_2O_2) [42-44]. The half life time of these radicals varies in microsecond to millisecond time scale. Superoxide ($O_2{}^-$) radicals have half life of 2-4µs. Hydrogen peroxide (H_2O_2) radicals have half life of 1ms [45]. Plants

always try to keep the equilibrium between the production and the scavenging of ROS however sudden increase in intracellular levels of ROS which can cause significant damage to cell structures [45]. Without having a reliable technique, researchers unable to detect the effect of ROS on the changes in plants instantly. Various mechanisms of tolerance to O_3 have been suggested. Generally a weak antioxidative defense system may enhance the susceptibility of photosynthetic tissues to damage. In general, higher activities of scavenger antioxidant enzymes or substances may protect from oxidative stress [46].

Plants cannot select or move their living conditions as animals can, and thus must live responding to their surrounding environment. Whenever environmental components, such as temperature, water in the soil, nutrients or air pollutants, either exceeds the range to which the plants can adapt or become limiting, the plant develops abnormal visual symptoms, growth, and yield. Leaf growth taken place because of the cells expansion and cells differentiation [47,48]. Genetic and environmental factors have an immense impact on plant size and form such a way that crops can be categorized in to three groups according to the sensitivity of O_3 such as O_3 sensitive crops, moderately sensitive crops and O_3 resistant crops.

In order to assess the O_3 stress, most researchers measured biomass (µg~mg), height change (µm~mm), counting, chemical analysis, that all required long waiting periods to arrive at a definite result on O_3 influence as they were done from post-harvest [49-51]. The majority of methods for investigating internal structure of plants are invasive. They caused to damage the tissue under study, thereby limiting their application for *in-vivo* monitoring. An example of such a destructive approach is conventional light microscopy which requires a destruction of sample and a subsequent analysis, thus plants responses to external stress are inferred indirectly. In addition, the analysis

cannot be performed in real time. There is a need of fast and reliable method to assess the structural (functional) changes in plants against O_3 stress.

To overcome these limitations, we proposed fOCT biospeckle imaging and signal analysis method to monitor the effect of O_3 on plants well. In the experiments, *Allium tuberosum*, commonly known as Chinese chives was exposed to 0, 80, 120, and 240ppb O_3 concentrations, and the effects to both back and front side of the leaf were observed to validate the developed fOCT biospeckle imaging and signal analysis for functional changes inside the leaf. Here, first approach was employed to analyze biospeckle signals. In addition, separate experiments were conducted with Chinese chive under 240ppb of O_3 exposure and biospeckle signals of different depth positions were analyzed with our second approach.

Water is one of the most important compounds in the life of plants, because it forms the environment in which most of the biochemical reactions of the cell occur. Even a slight water imbalance inside the plant or water contamination can cause malfunctioning of many cellular processes. Plants absorbed most of the water from soil through their root system. The soil is a source of water and oxygen for the plant, but also a source of different types of contaminants, such as metallic elements, arsenic or high salt concentration. All these pollutants cause stress to plants and through the root system this stress is communicated to the rest of the plant. Different pollutants can cause both physiological and morphological changes in plants and these changes have been studied extensively in the past two decades.

References

1. Houndsfield G N, (1973) "Computerized transverse axial scanning (tomography: Part I. Description of system," Br. J. Radiol. 46, 1016.

2. Damadian R, Goldsmith M, Minkoff L, (1977) "NMR in cancer: XVI. FONAR image of the live human body," Physiol. Chem. Phys. 9, 97.

3. Wild and J J, Reid J M, (1952) "Application of Echo-Ranging Techniques to the Determination of Structure of Biological Tissues ," Science 115, 226.

4. Huang D, Swanson E A, Lin C P, Schuman J S, Stinson W G, Chang W, Hee M R, Flotte T, Gregory K, Puliafito C A, Fujimoto J G, (1991) "Optical coherence tomography," Science 254(5035), 1178-1181.

5. Fercher A F, (1996) "Optical Coherence Tomography," Journal of Biomedical Optics 1(2), 157-173.

6. Chance B et al., (1988) "Comparison of time-resolved and -unresolved measurements of deoxyhemoglobin in brain," Proc. Natl. Acad. Sci. U.S.A. 85, 4971.

7. Fujimoto J G et al., (1989) Opt. Lett. 16, 487.

8. Spears K G et al., (1990) IEEE Trans. Biomed. Eng. 36, 1210.

9. Anderson-Engels S et al., (1990) Opt. Lett. 15, 1179.

10. Wang L, Ho P P, Liu C, Zhang G, Alfano R R, (1991) "High-resolution tomographic imaging of a human cerebellum: comparison of absorption and grating-based phase contrast," Science 253, 769.

11. Youngquist R C, Carr S, Davies D E M, (1987) Opt. Lett. 12, 158.

12. Kino G S, Chim S S C, (1990) Appl. Opt. 29, 3775.

13. Fercher A F, Mengedoht K, Werner W, (1988) Opt. Lett. 13, 186.

14. Hitzenberger C K, (1991) Inv. Ophthalmo. Vis. Sci. 32, 616.

15. Huang D et al., (1991) Lasers Surg. Med. 11, 5.

16. Gilgen H H et al., (1989) J. Lightwave Technol. 7, 1255.

17. Wojtkowski M, (2010) "High-speed optical coherence tomography: basics and applications," Appl. Opt. 49(16), D30-D61.

18. Leitgeb R A, Drexler W, Unterhuber A, Hermann B, Bajraszewski T, Le T, Stingl A, Fercher A F, (2004) "Ultrahigh resolution Fourier domain optical coherence tomography," Opt. Express 12(10), 2156-2165.

19. Fujimoto J G, Drexler W, (2008) "Optical Coherence Tomography: Technology and Applications," Springer-Verlag.

20. Drexler W, Morgner U, Ghanta R K, Kartner F X, Schuman J S, Fujimoto J G, (2001) "Ultrahigh-resolution ophthalmic optical coherence tomography," Nat. Med. 7(4), 502-506.

21. Wojtkowski M, Leitgeb R, Kowalczyk A, Szewski B, Fercher A F, (2002) "In vivo human retinal imaging by Fourier domain optical coherence tomography," Journal of Biomedical Optics 7(3), 457-463.

22. Gambichler T, Moussa G., Sand M, Sand D, Altmeyer P, Hoffmann K, (2005) "Applications of optical coherence tomography in dermatology," J. Dermatol. Sci. 40(2), 85-94.

23. Fujimoto J G, Brezinski M E, Tearney G J, Boppart S A, Bouma B, Hee M R, Southern J F, Swanson E A, (1995) "Optical biopsy and imaging using optical coherence tomography," Nat. Med. 1(9), 970-972.

24. Hettinger J W, Mattozzi M D P, Myers W R, Williams M E, Reeves A, Parsons R L, Haskell R C, Petersen D C, Wang R Y, Medford J I, (2000) "Optical coherence microscopy. A technology for rapid, in vivo, non-destructive visualization of plants and plant cells," Plant Physiol. 123(1), 3-15.

25. Reeves A, Parsons R L, Hettinger J W, Medford J I, (2002) "In vivo three-dimensional imaging of plants with optical coherence microscopy microscopy," J. Microsc. 208(3), 177-189.

26. Boccara M, Schwartz W, Guiot E, Vidal G, Paepe R D, Dubois A, Boccara A C, (2007) "Early chloroplastic alterations analysed by optical coherence tomography during a harpin-induced hypersensitive response," Plant J. 50(2), 338-346.

27. Braga R A, Dupuy L, Pasqual M, Cardosos R R, (2009) "Live biospeckle laser imaging of root tissue," European Biophysics Journal (38), 679-686.

28. Maheswari R U, Takaoka H, Homma R, Kadono H, Tanifuji M, (2002) "Implementation of optical coherence tomography (OCT) in visualization of functional structures of cat visual cortex," Opt Commun 202(1-3), 47-54.

29. Maheswari R U, Takaoka H, Kadono H, Homma R, Tanifuji M, (2003) "Novel functional imaging technique from brain surface with optical coherence tomography enabling visualization of depth resolved functional structure in vivo," J. Neurosci. Methods 124(1), 83-92.

30. Chen Y, Aguirre A D, Ruvinskaya L, Devor A, Boas D A, Fujimoto J G, (2009) "Optical coherence tomography (OCT) reveals depth-resolved dynamics during functional brain activation," J. Neurosci. Methods 178(1), 162-173.

31. Watanabe H, Rajagopalan U M, Nakamichi Y, Igarashi K M, Madjarova V D, Kadono H, Tanifuji M, (2011) "In vivo layer visualization of rat olfactory bulb by a swept source optical coherence tomography and its confirmation through electrocoagulation and anatomy," Biomedical Optics Express, 2, 8, 2279.

32. Kurenda A, Adamiak A, Zdunek A, (2012) "Temperature effect on apple biospeckle activity evaluated with different indices," Postharvest Biology and Technology 67, 118-123.

33. Aizu Y, Asakura T, (1996) "Trends in Optics," Academic Press, San Diego, 27-49.

34. Ansari M D Z, Nirala A K, (2013) "Biospeckle activity measurement of Indian fruits using the methods of cross-correlation and inertia moments," Optik 124, 2180-2186.

35. Ashmore M R, (2005) "Assessing the future global impacts of ozone on vegetation," Plant, Cell and Environment 28, 949-964.

36. Richards B L, Middleton J T, Hewitt W B, (1958) "Air pollution with relation to agronomic crops. V. oxidant stipple of grape," Agronomy Journal 50, 599-561.

37. Crutzen P J, Lawrence M G, Poschl U, (1999) "On the background photochemistry of ozone," Tellus 51A-B, 123–146.

38. Reeves C E, Penkett S A, Bauguitte S, Law K S, Evans M J, Bandy B J, Monks P S, Edwards G D, Phillips G, Barjat H, Kent J, Dewey K, Schmitgen S, Kley D, (2002) "Potential for photochemical ozone formation in the troposphere over the North Atlantic as derived from aircraft observations during ACSOE," Journal of Geophysical Research107, D23, 4707.

39. Torsethaugen G, Pell T G, Assmann S M, (1999) "Ozone inhibits guard cell K+ channels implicated in stomatal opening," Proceedings of the National Academy of Sciences of the United States of America **96:** 13577-13582.

40. Pell E J, Schlagnhaufer C D, Arteca R N, (1997) "Ozone-induced oxidative stress: mechanisms of action and reaction," Physiologia Plantarum **100**: 264-273.

41. Grandjean G A, Fuhrer J, (1992) "The response of spring wheat (Triticum aestivum L.) to ozone at higher elevations III. Responses of leaf and canopy gas-exchange, and chlorophyll fluorescence to Ozone Flux," New Phytologist **122**: 321-328.

42. Frei M, Tanaka J P, Wissuwa M, (2008) "Genotypic variation in tolerance to elevated ozone in rice: dissection of distinct genetic factors linked to tolerance mechanisms," Journal of Experimental Botany 59, 3741-3752.

43. Fiscus E L, Booker F L, Burkey K O, (2005) "Crop responses to ozone : uptake, modes of action, carbon assimilation and partitioning," Plant, Cell and Environment 28, 997-1011.

44. Inada H, Yamaguchi M, Satoh R, Hoshino D, Nagasawa A, (2008) "Effects of ozone on photosynthetic components and radical scavenging system in leaves of rice (Oryza sativa L.) ," Journal of Agricultural Meteorology 64 (4), 243-255.

45. Sarvajeet S G, Narendra T, (2010) "Reactive oxygen species and antioxidant machinery in abiotic stress tolerance in crop plants," Plant Physiology and Biochemistry 48, 909-930.

46. Kumagai T, Hidema J, Kang H, Sato T, (2001) "Effects of supplemental UV-B radiation on the growth and yield of two cultivars of Japanese lowland rice (Oryza sativa L.) under the field in a cool rice-growing region of Japan," Agriculture, Ecosystems and Environment 83, 201-208.

47. Weele C M V, Jiang H S, Palaniappan K K, Ivanov V B, Palaniappan K, Baskin T I, (2003) "A New Algorithm for Computational Image Analysis of Deformable Motion at High Spatial and Temporal Resolution Applied to Root Growth. Roughly Uniform Elongation in the Meristem and Also, after an Abrupt Acceleration, in the Elongation Zone," Plant Physiology **132**, 1138-1148.

48. Taiz L, Zeiger E, (2002) "Plant Physiology. 3rd Edition," Sinauer Associates, Inc., Sunderland, Massachusetts.

49. Reich P B, (1987) "Quantifying plant response to ozone: a unifying theory," Tree Physiology **3**, 63-91.

50. Yonekura T, Shimada T, Miwa M, Arzate A, Ogawa K, (2005) "Impacts of Tropospheric Ozone on Growth and Yield of Rice (*Oryza sativa L.*)," Agricultural Meteorology **60**, 1045-1048.

51. Yamaguchi M, Inada H, Satoh R, Hoshino D, Nagasawa A, Negishi Y, Sasaki H, Nouchi I, Kobayashi K, Izuta T, (2008) "Effects of ozone on the Growth, Yield and Leaf Gas Exchange Rates of Two Japanese Cultivars of Rice (*Oryza sativa* L.) ," Agricultural Meteorology **64**, 131-141.

CHAPTER 2

2. Optical Coherence Tomography (OCT)

2.1. Introduction to interferometry

Since the optical coherence tomography based on law coherence interference, prior to introducing its fundamentals, the principle of interferometry will be introduced. Interference is commonly seen light phenomena in environment, such that the vivid colors in a soap bubble and vivid colors in an oil stick on a wet road. Further the colored fringes seen in a thin air film enclosed between two glass plates when they are brought into contact. Those fringes are commonly known as "Newtons rings", first described by Boyle and independently by Hooke in the latter half of the 17th century. This discovery can be called the starting point of optical interferometry [1].

Interferometers are basic optical measurement tools (Hariharan 1985) in which guarantee very high sensitivity with high reliability. Further Interferometers can be used real time and non distractive measurements [2]. Generally, in optical interferometry, shape, displacement, deformation, etc., of the object are obtained from the difference between the wavefronts of optical waves from the reference and object surfaces, which appear as interference fringes [3].

From the basic equations of Electromagnetic Theory, with a certain approximation, distributions of intensity of light beams can be described in terms of changes of intensity in the cross-sectional area of the light beam. When

two or more light beams coming from the same coherent light source are superposed, the distribution of the resulting intensity cannot be described as a simple addition of light beam intensities. The intensity in the region of superposition is found to vary from point to point between maxima that exceed the sum of the intensities of the beams, and minima that may be zero [4,5].

Let us consider the case of superposition of two waves that can be described with their complex amplitudes,

$$a_1 = A_1 e^{i\phi_1} \tag{2.1}$$

$$a_2 = A_2 e^{i\phi_2} \tag{2.2}$$

here A_1 and A_2 are the amplitudes of the waves, and ϕ_1 and ϕ_2 are the wave phases. In optical measurements, the observed quantity is the intensity, which in the case of the two superposing waves becomes

$$I = |a_1 + a_2|^2 \tag{2.3}$$

$$I = |a_1|^2 + |a_2|^2 + 2|a_1||a_2|cos(\phi_1 - \phi_2) \tag{2.4}$$

$$I = I_1 + I_2 + 2\sqrt{I_1 I_2} cos(\Delta\phi) \tag{2.5}$$

Therefore, the resultant intensity cannot merely be described as a sum of the two intensities. This phenomenon is called interference and $2\sqrt{I_1 I_2} cos(\Delta\phi)$ is called the interference term [4,5]. The maximum intensity is obtained when $cos(\Delta\phi) = 1$, i.e. when the phase difference is $(\Delta\phi) = 2n\pi$. The two waves are in-phase, which means that there is a constructive interference. The minimum intensity is obtained when $cos(\Delta\phi) = -1$, i.e. when the phase difference is $\Delta\phi = (2n + 1)\pi$. The two waves are out-of-phase which means that there is a destructive interference. The interference phenomenon produces alternate dark and bright bands known as interference fringes. If the two beams are to

interfere to produce stable patterns, there are some requirements, namely the two waves should be coherent in time and space. There are numerous optical set-ups that can be used for very precise interferometric measurements of different mechanical characteristics. Generally they can be classified into [4,5],

Wavefront dividing

Amplitude dividing.

2.1.1. Wavefront dividing Interferometers

There are a number of wavefront dividing interferometers. Most common among these are Fresnel double mirror, Fresnel double prism, Lloyd's mirror and Michelson's stellar interferometer. The basic concept behind those interferometers is Thomas Young`s in the earliest of interference experiments. Here portion of primary wave-front are used either directly as sources to emit secondary waves. These secondary waves are then brought together, thereupon to interfere. This is known as Young`s double slit experiment. Figures 2.1(a, b, and c) correspond to the classic arrangement of Young`s Experiment [5].
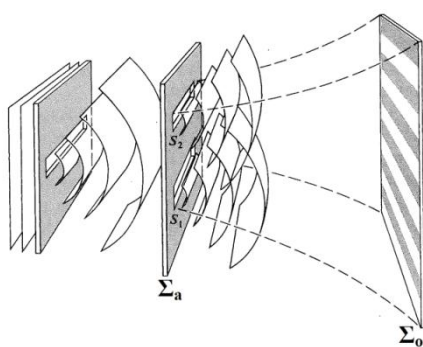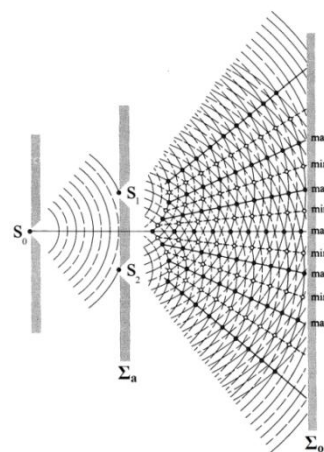
(a)   (b)
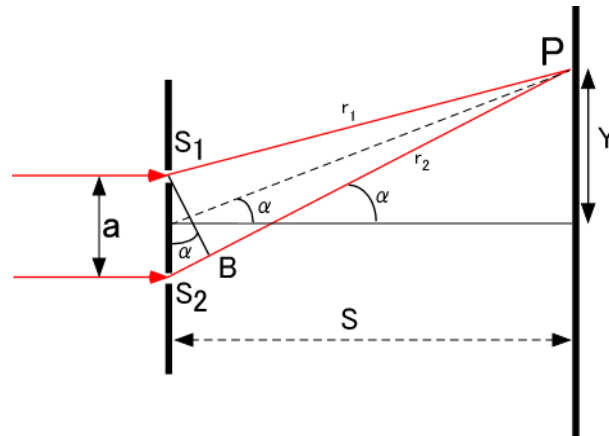
(c)

Figure 2.1. Young's Experiment (b) Overlapping waves showing peaks and troughs. (c) The eometry of Young`s Experiment.

Following calculation illustrate the mathematical condition to satisfy the wave-front interference. The wavefront incident on the screen Σ_a is divided by the two small holes S_1 and S_2. Spherical wavefronts emerge from the holes and will interfere, with the interference being observed on the second screen, Σ_o. The path length difference of the light reaching a point P in screen Σ_o can be calculated as shown in Figures 2.1(c).

$$S_2B = S_2P - S_1P$$

$$S_2B = r_2 - r_1$$

$$r_2 - r_1 = a \sin\alpha$$

If the distance **S** is much greater than distance **a**, the distance **S** can be approximated by

$$r_2 - r_1 = a\alpha$$

Further,

$$\alpha \approx \frac{Y}{S}$$

$$r_2 - r_1 = a\frac{Y}{S}$$

The phase difference then becomes,

$$\delta = k(r_2 - r_1)$$

$$\delta = \frac{2\pi}{\lambda}\left(\frac{a}{S}\right)Y$$

If this is inserted into the general expression for the resulting intensity distribution, where $I_1 = I_2 = I_0$, the intensity becomes,

$$I(y) = 2I_0\big(1 + cos(\delta)\big) \tag{2.6}$$

$$I(y) = 4I_0\left[cos^2\left(\frac{2\pi}{\lambda}\left(\frac{a}{S}\right)Y\right)\right] \tag{2.7}$$

2.1.2. Amplitude dividing Interferometers

Here, the amplitude splitting, the primary wave itself is divided into two fragments, which travel different paths before recombining and interfering. This is done with the help of a beam splitter. A commonly used amplitude division instrument is the Michelson interferometer, a schematic diagram is shown in Figure 2.2.

<div align="center">

(a)   (b)

</div>
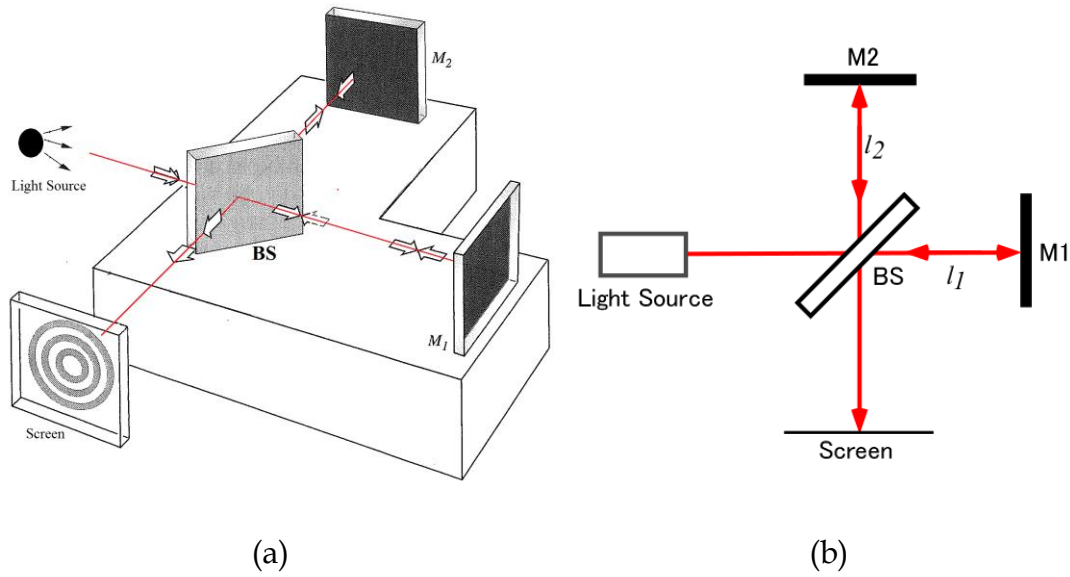
Figure 2.2. The Michelson Interferometer.

In the basic Michelson interferometer the light from a source, is divided by beam splitter (BS) oriented at 45° to the beam. The transmitted beam travels to mirror M1 where it is back $\Delta\emptyset = k\Delta x$ reflected to BS. Further the reflected beam travels to mirror M2 where it is reflected. The two beams that are directed towards the screen, E, interfere to produce fringes on the screen.

If it is perfectly aligned using perfect lenses, mirrors and ideal BS and laser, the interference of two smooth waveforms would create a constant intensity across the screen. The phase difference is equal to the optical path length difference multiplied by the wave number, which is expressed by

$$(\Delta\emptyset) = 2\pi\frac{l}{\lambda} \tag{2.8}$$

where λ is the laser wavelength, and l is the optical path length difference of two beams.

The path difference between the two partial waves can be varied by moving one of the mirrors. Movement of a mirror through a distance x gives a path difference of $2x$ and a phase difference of,

<div align="center">

22

</div>

$$\Delta\emptyset = \left(\frac{2\pi}{\lambda}\right)2x \qquad\qquad (2.9)$$

In here constructive interference occurs when,

$$\Delta\emptyset = 2m\pi$$

$$m = 0, \pm2, \pm4, \dots\dots$$

Destructive interference occurs when,

$$\Delta\emptyset = (2m + 1)\pi$$
$$m = \pm1, \pm3, \dots\dots$$

The resultant intensity distribution is given by,

$$I(x) = 2I\left[1 + cos\left(\frac{4\pi x}{\lambda}\right)\right] \qquad\qquad (2.10)$$

2.2. Optical coherence tomography (OCT)

2.2.1. Introduction

A simple OCT system schematic is illustrated in Figure 2.3(b). Since OCT is based on low-coherence interfernce, Michelson interferometer is built and a low-coherance light source is used. to Light from a low-coherence source is directed into a 50:50 beams splitter (BS). The BS is assumed to split the incident optical power evenly into sample and reference arms, although many practical OCT system designs take advantage of unbalanced beam splitting [6,7]. The backscattered light from the sample is mixed with the reflected light from the reference mirror, and the combined light is made to interfere on the surface of a detector. The electronic signals detected at the photoreceiver are processed into an A-scan, representing the depth resolved reflectivity profile of the sample at

23

the focal spot of the sample beam at a fixed lateral position of the scanning mechanism. A two-dimensional cross-sectional image of the sample, called B-scan is achieved by scanning the probing beam in the sample arm.

2.2.2. Time domain OCT

(a)   (b)

(c)
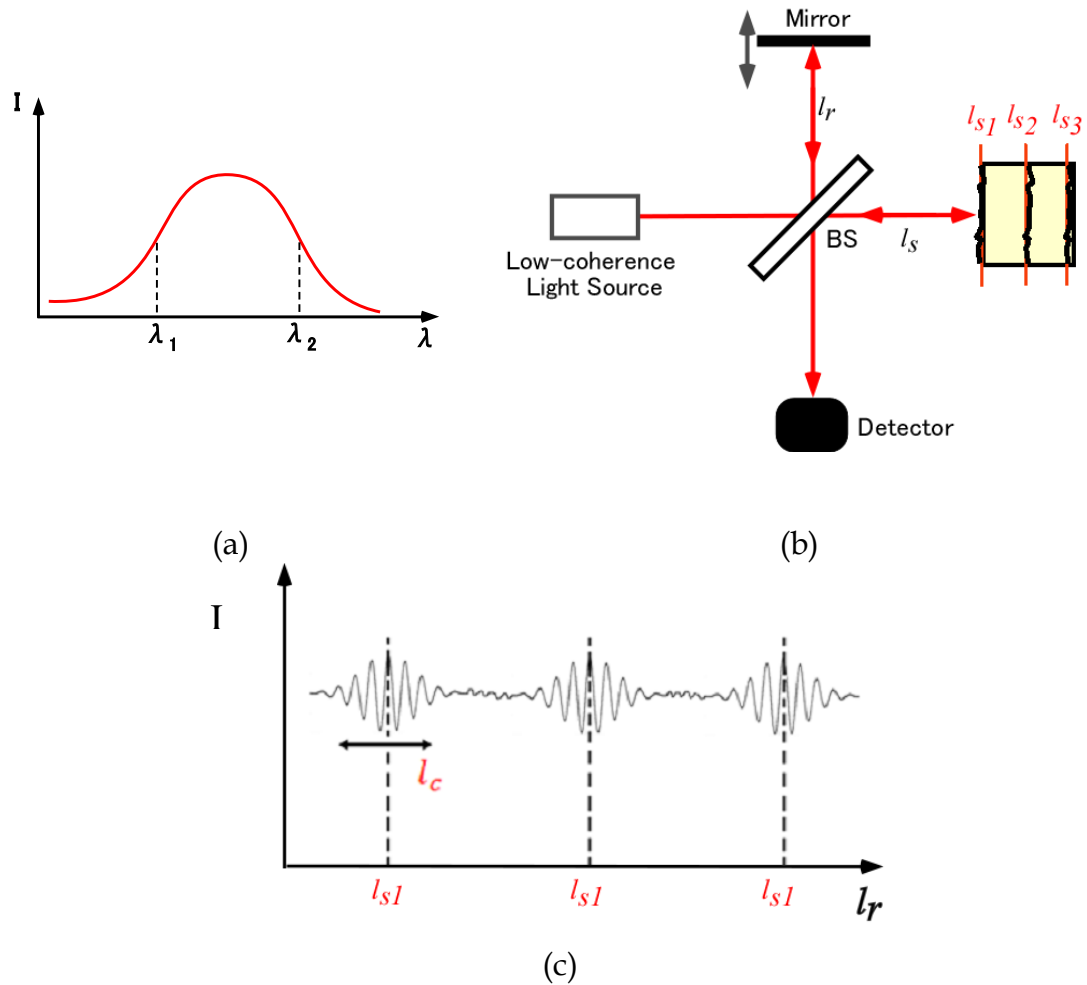
Figure 2.3. (a) Low coherence light source spectrum. (b) Time domain optical coherence tomography. (c) Detected interference signal

In the case of time domain OCT (TD-OCT), the low-coherence source in Figure 2.3(a) is broadband and continuous-wave, the reference arm delay is repetitively scanned in length, a single-channel detector is employed, and the required signal processing consists of detecting the envelope of the detected fringe pattern corresponding to interference between the reference arm light

24

and each successive scattering site in the sample. As an example, in Figure 2.3(b), sample consist of three depth layers and corresponding path lengths are ls_1, ls_2 , and ls_3. When we scan the reference mirror at ls_1, ls_2, and ls_3, interference signal is resolved in depth direction as shown in Figure 2.3(c). At the data processing stage, depth resolved reflectivity profile is obtained. To overcome this difficult mechanical scanning in TD-OCT, a spectral domain OCT (SD-OCT) was proposed and is commonly used nowadays.

2.2.3. Spectral domain OCT

In the case of spectral domain OCT (SD-OCT) which is used in our study, the source is broadband and, the reference arm length is fixed at a position approximately corresponding to the position of the sample, and the spectral interference pattern between the light returning from the reference arm and all depths in the sample is dispersed by grating in a spectrometer and collected simultaneously on a line scan camera. The spectral interference pattern encodes in its spectral frequency content the entire depth-resolved structure of the sample at the position of the focal spot. Finally, a depth profile of the sample is obtained by taking a Fourier transforming the spectral interference pattern.

(a)
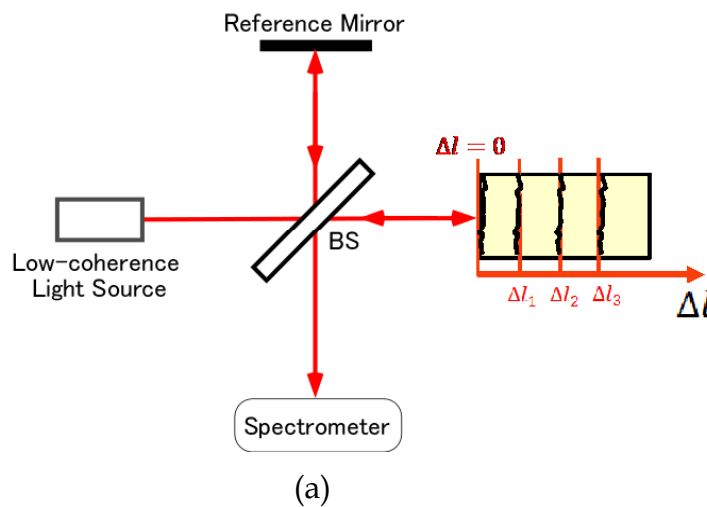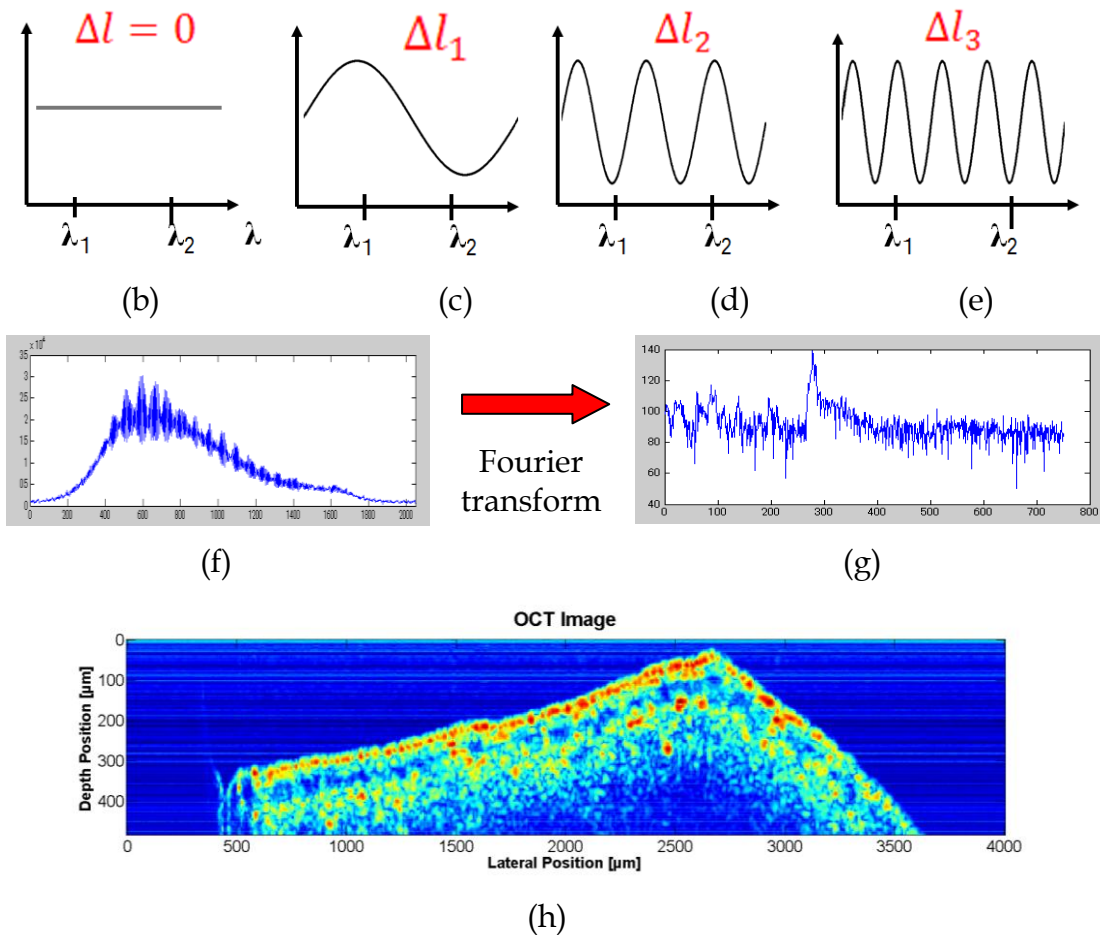
Figure 2.4. Basics of spectral domain OCT. (a) Michelson interferometer. (b~e) Signals received by the spectrometer from the surface, and other three layers of the sample corresponding to $\Delta l = 0$, Δl_1, Δl_2, Δl_3. (f) Spectrometer receives interference signal with combination of all the frequency components at the focal spot of the sample beam at a fixed lateral position of on the sample. (g) Signal is Fourier transformed to get depth resolved reflectivity profile at a fixed lateral position. (h) Two-demensional cross-sectional image of back surface Chinese chives leaf.

As an example, sample has four different depth layers as Figure 2.4(a). As the wave length is swept, the signals received by the spectrometer from the surface, and other three layers of the sample corresponding to $\Delta l = 0$, Δl_1, Δl_2, Δl_3 are shown in Figures 2.4(b, c, d, and e) respectively. Frequency of the signal is increased as the depth of the layer becomes higher. More and more higher frequency signal is obtained from more deeper layers. However, spectrometer receives interference signal with combination of all the frequency components at the focal spot of the sample beam at a fixed lateral position of on the sample

as shown in Figure 2.4(f). However signal received by the spectrometer is in wave length space (λ). Then interference signal is rescaled to get it into wave number (k), and finally it is Fourier transformed to get depth resolved reflectivity profile at a fixed lateral position (A-scan). Figure 2.4(h) shows two dimensional cross-sectional image of back surface of Chinese chives leaf achieved by scanning the probing beam in the sample arm (assembling multiple A-scans). We use a software program (LabVIEW 2011, National Instruments, USA) to rescale the interference signal.

(a)

(b)

$$k = \frac{2\pi}{\lambda}$$

(c)
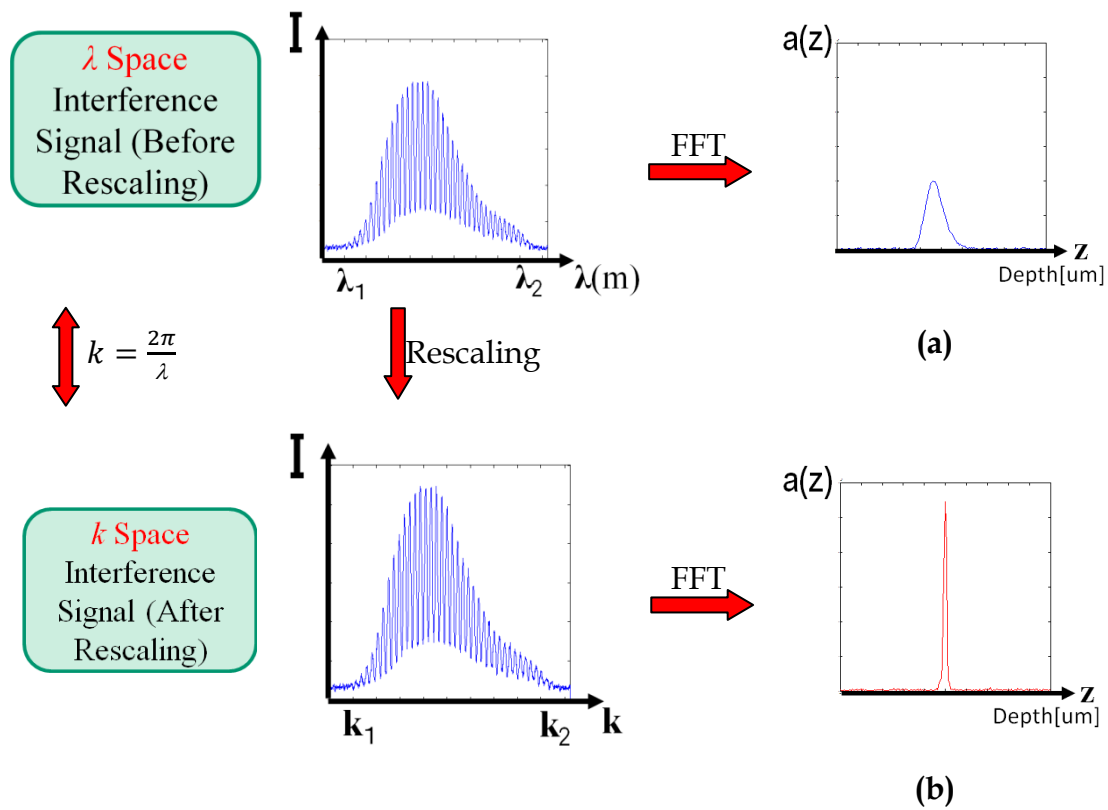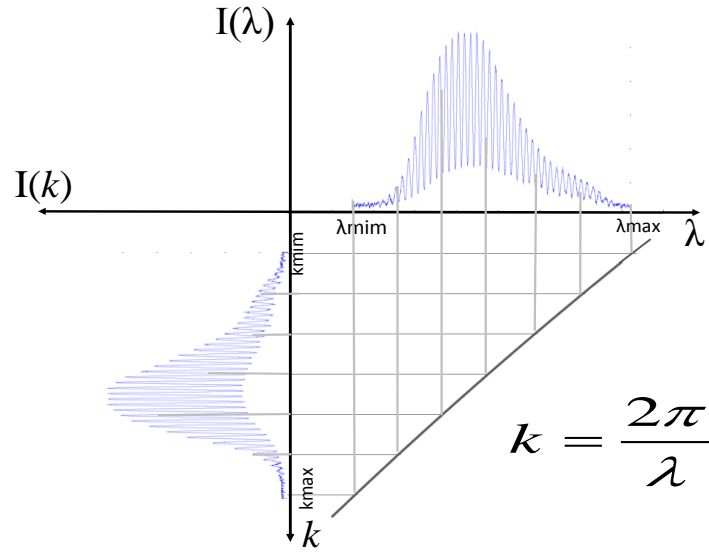
Figure 2.5. Rescaling process. (a) Reflectivity profile obtained without rescalling the interference signal (b) Same obtained after rescalling.

Rescaling interference signal from λ to k space, narrow profile is obtained. The intensity of the peak is also increased hence, higher resolution and contrast can be achieved.

2.2.3. Point spread function (PSF)

To get point spread function of our SD-OCT system, a mirror was kept in the sample arm instead of a biological sample. Interference signals were acquired as the mirror was being moved by a micrometer screw of its bed. Signal was Fourier transformed to get depth profile. Since the mirror has one surface layer, reflectivity profile has only one notable peak. However by moving the mirror, such many profiles (Figure 2.6) can be taken corresponding to the path length difference of the mirror. Full width of half maximum of profile gives us the coherence length of the source and it is equivalent to the axial (depth) resolution of the system. In here, we got the depth resolution as 6μm.
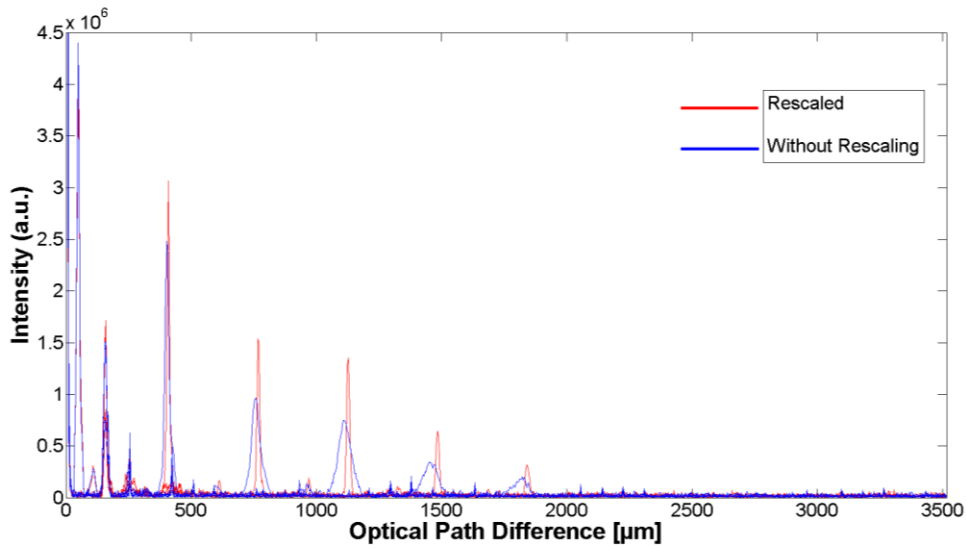
Figure 2.6. Point spread function obtained with our SD-OCT system.

2.2. Mathematical treatments in OCT

2.2.1. General treatment
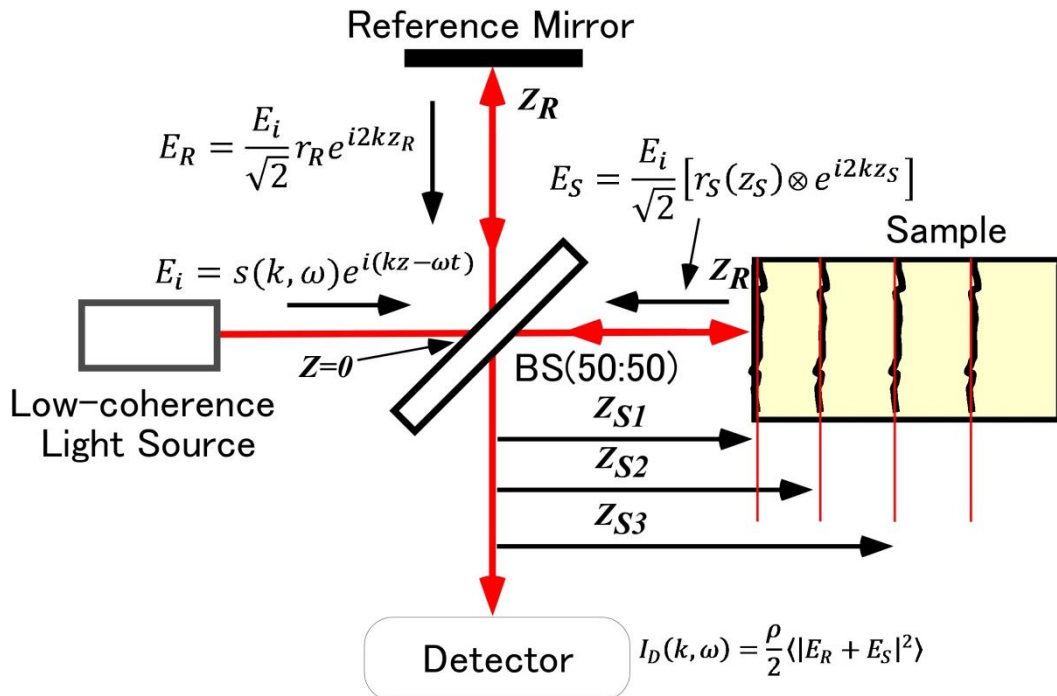
Figure 2.7. Michelson low coherence interferometry used in OCT.

Consider the Michelson interferometer illustrated in Figure 2.7. The interferometer is illuminated by a polychromatic plane wave whose electric field expressed in complex form is,

$$E_i = s(k, \omega)e^{i(kz-\omega t)} \tag{2.11}$$

here, $s(k, \omega)$ is the electric field amplitude as a function of the wave number $k = 2\pi/\lambda$ and angular frequency $\omega = 2\pi\nu$, which are respectively the spatial and temporal frequencies of each spectral component of the field having wavelength λ. The wavelength λ and frequency ν are coupled by the index of refraction $n(\lambda)$ (which is wavelength-dependent in dispersive media) and vacuum speed of light c according to $c/n(\lambda) = \lambda\nu$. The BS is assumed to have an achromatic (wavelength-independent) power splitting ratio of 50:50. The reference reflector is assumed to have electric field reflectivity r_R and power reflectivity $R_R = |r_R|^2$. The distance from the BS to the reference reflector is z_R.

The sample under interrogation is characterized by its depth-dependent electric field reflectivity profile along the sample beam axis $r_S(z_S)$, where z_S is the path length variable in the sample arm measured from the BS. In general $r_S(z_S)$ is continuous, resulting from the continuously varying refractive index of biological tissues and other samples. It may also be complex, encoding the phase as well as the amplitude of each reflection. However, for an illustrative example, we assume a series of N discrete, real delta function reflections of the form,

$$r_S(z_S) = \sum_{n=1}^{N} r_{S_n}\delta(z_S - z_{S_n}) \tag{2.12}$$

each reflection characterized by its electric field reflectivity $r_{S1}, r_{S2}\dots$, and path length from the BS of $z_{S1}, z_{S2}\dots$ (Figure 2.8).

$$r_S(z_S) = \sum_{n=1}^{N} r_{S_n} \delta(z_S - z_{S_n})$$

$$E_S = \frac{E_i}{\sqrt{2}}\left[r_S(z_S) \otimes e^{i2kz_S}\right]$$

$$\frac{E_i}{\sqrt{2}}$$

Reflections from sample

z_{S1}
z_{S2}
z_{S3}
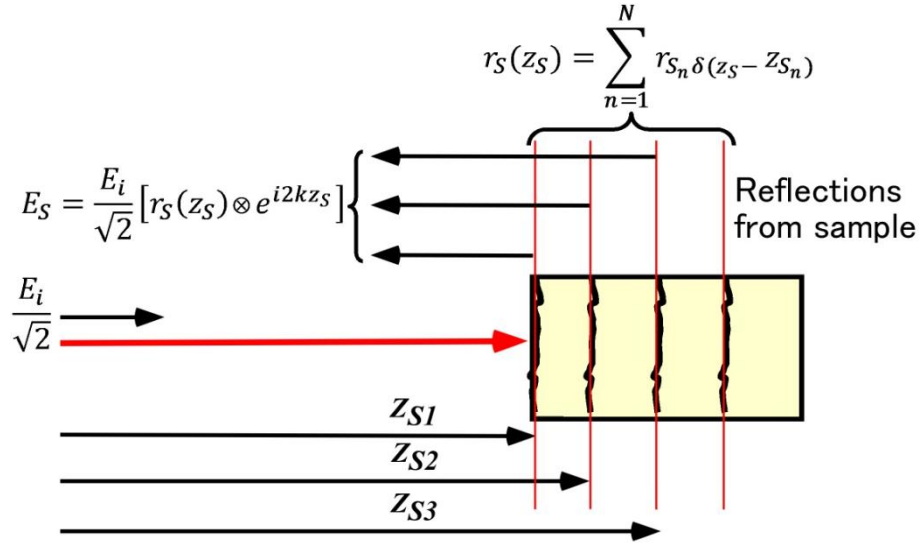
Figure 2.8. Light reflections from different depth layers of the sample.

The power reflectivity of each reflector is given by the magnitude squared of the electric field reflectivity, for example $R_{S1} = |r_{S1}|^2$. The reconstruction of the function $\sqrt{R_S(z_S)}$ from noninvasive interferometric measurements is the goal of low-coherence interferometry in OCT. The electric field passing through the BS after returning from the sample arm is,

$$E_S = \frac{E_i}{\sqrt{2}}\left[r_S(z_S) \otimes e^{i2kz_S}\right] \tag{2.13}$$

where $\otimes$ represents convolution, and the factor of 2 in the exponential kernel accounts for the round-trip path length to each sample reflection. Note that for most samples such as biological tissues imaged with OCT, sample reflectivities R_{S1}, R_{S2} . . .are typically very small (on the order of ~10^{-4} to 10^{-5}); thus the returned reference field typically dominates the reflected sample field. Indeed, published studies have shown that selection of the appropriate reference reflectivity is an important design criterion in OCT system design [8, 9]. For the example of discrete reflectors, the fields incident on the BS after returning from the reference and sample arms are given by,

$$E_R = \frac{E_i}{\sqrt{2}}r_R e^{i2kz_R} \tag{2.14}$$

$$E_S = \frac{E_i}{\sqrt{2}} \sum_{n=1}^{N} r_{S_n} e^{i2kz_{S_n}} \tag{2.15}$$

respectively. The returning fields are halved in power upon passing through the BS again and interfere at the square-law detector, which generates a photocurrent proportional to the square of the sum of the fields incident upon it, given by,

$$I_D(k,\omega) = \frac{\rho}{2} \langle |E_R + E_S|^2 \rangle = \frac{\rho}{2} \langle (E_R + E_S)(E_R + E_S)^* \rangle \tag{2.16}$$

Here, ρ is the responsivity of the detector (units Amperes/Watt), the factor of 2 reflects the second pass of each field through the BS, and the angular brackets denote integration over the response time of the detector. Arbitrarily setting $z = 0$ at the surface of the BS, and expanding for the detector current gives

$$I_D(k,\omega) = \frac{\rho}{2} \langle \left| \frac{s(k,\omega)}{\sqrt{2}} r_R e^{i(2kz_R - \omega l)} + \frac{s(k,\omega)}{\sqrt{2}} \sum_{n=1}^{N} r_{S_n} e^{i(2kz_{Sn} - \omega l)} \right|^2 \rangle \tag{2.17}$$

Expanding the magnitude squared functions in (equation 2.17) eliminates the terms dependent upon the temporal angular frequency $\omega = 2\pi\nu$, which is reasonable since ν oscillates much faster than the response time of any practical detector. This leaves the temporally invariant terms

$$I_D(k) = \frac{\rho}{4} [S(k)(R_R + R_{S1} + R_{S2} + \cdots)]$$

$$+ \frac{\rho}{4} \left[S(k) \sum_{n=1}^{N} \sqrt{R_R R_{S_n}} \left(e^{i2k(z_R - z_{Sn})} + e^{-i2k(z_R - z_{Sn})} \right) \right]$$

$$+ \frac{\rho}{4} \left[S(k) \sum_{n \neq m=1}^{N} \sqrt{R_{S_n} R_{S_m}} \left(e^{i2k(z_{Sn} - z_{Sm})} + e^{-i2k(z_{Sn} - z_{Sm})} \right) \right] \tag{2.18}$$

Here, $S(k) = \langle |s(k,\omega|^2 \rangle$ is substituted, which encodes the power spectral dependence of the light source. As an illustrative example, a Gaussian-shaped

light source spectrum is convenient to use in modeling OCT because it approximates the shape of actual light sources and also has useful Fourier transform properties. The normalized Gaussian function $S(k)$ and its inverse Fourier transform $\gamma(z)$ are given by

$$\gamma(z) = e^{-z^2 \Delta k^2} \quad \overset{\leftrightarrow}{F} \quad S(k) = \frac{1}{\Delta k \sqrt{\pi}} e^{-\left[\frac{(k-k_0)}{\Delta k}\right]^2} \tag{2.19}$$

and are illustrated in Figure 2.9.
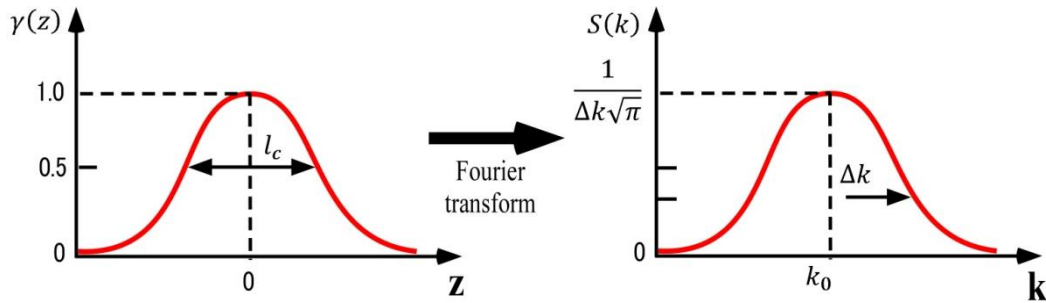
Figure 2.9. Illustration of Fourier transform relationship between the Gaussian-shaped coherence function $\gamma(z)$ (characterized by the coherence length l_c), and the light source spectrum $S(k)$ (characterized by the central wavenumber k_0 and wavenumber bandwidth Δk)

Here, k_0 represents the central wave number of the light source spectrum and Δk represents its spectral bandwidth, corresponding to the half-width of the spectrum at $1/e$ of its maximum. As will be seen below, the inverse Fourier transform of the source spectrum $\gamma(z)$, otherwise called the "coherence function," dominates the axial point-spread function (PSF) in OCT imaging systems (at least those employing a low numerical aperture focusing objective). The PSF is commonly characterized by its full width at half the maximum (FWHM) value, and is the definition of the round-trip "coherence length" of the light source l_c.

The coherence length is an explicit function of the light source bandwidth, stated both in wave number and wavelength terms as

$$l_c = \frac{2\sqrt{\ln(2)}}{\Delta k} = \frac{2\ln(2)}{\pi} \frac{\lambda_0^2}{\Delta \lambda} \tag{2.20}$$

Here, $\lambda_0 = 2\pi/k_0$ is the center wavelength of the light source and $\Delta\lambda$ is its wavelength bandwidth, defined as the FWHM of its wavelength spectrum (so that $\Delta k = \frac{\pi}{\sqrt{\ln(2)}}\frac{\Delta\lambda}{\lambda_0^2}$). Note the inverse relationship between the coherence length and the light source bandwidth.

Using Euler's rule to simplify (equation...) generates a real result for the detector current as a function of wave number, commonly known as the "spectral interferogram"

$$I_D(k) = \frac{\rho}{4}[S(k)(R_R + R_{S1} + R_{S2} + \cdots)] \quad \text{"DC Terms"}$$

$$+ \frac{\rho}{2}\left[S(k)\sum_{n=1}^{N}\sqrt{R_R R_{S_n}}\cos[2k(z_{R-z_{S_n}})]\right] \quad \text{"Cross-correlation Terms"}$$

$$+ \frac{\rho}{4}\left[S(k)\sum_{n\neq m=1}^{N}\sqrt{R_{S_n} R_{S_m}}\cos[2k(z_{S_n-z_{S_m}})]\right] \quad \text{"Auto-correlation Terms"}$$

$$(2.21)$$

The result in (equation 2.17) includes three distinct components:

A pathlength-independent offset to the detector current, scaled by the light source wavenumber spectrum and with amplitude proportional to the power reflectivity of the reference mirror plus the sum of the sample reflectivities. This term is often referred to as "constant" or "DC" component. This is the largest component of the detector current if the reference reflectivity dominates the sample reflectivity.

A "cross-correlation" component for each sample reflector, which depends upon both light source wave number and the path length difference between the reference arm and sample reflectors. This is the desired component for OCT imaging. Since these components are proportional to the square root of the sample reflectivities, they are typically smaller than the DC component.

However, the square root dependence represents an important logarithmic gain factor over direct detection of sample reflections.

"Autocorrelation" terms representing interference occurring between the different sample reflectors appear as artifacts in typical OCT system designs (exceptions occur in common-path system designs, in which the autocorrelation component represents the desired signal). Since the autocorrelation terms depend linearly upon the power reflectivity of the sample reflections, a primary tool for decreasing autocorrelation artifacts is selection of the proper reference reflectivity so that the autocorrelation terms are small compared to the DC and interferometric terms.
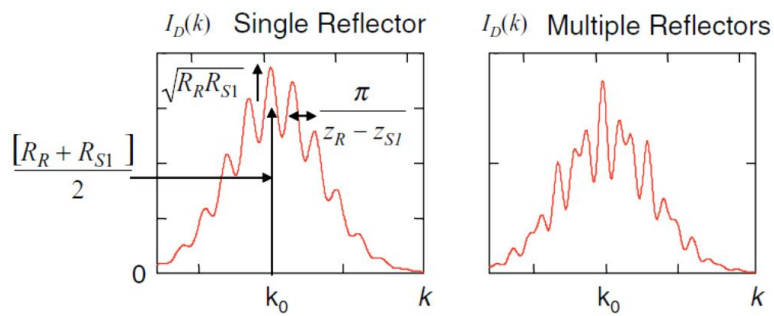
Figure 2.10. Important features of the spectral interferogram. For a single sample reflector of field reflectivity r_{S1} = 0.1 (*left*) the cross-correlation component with amplitude $\sqrt{R_R R_{S1}}$ and wavenumber period $\pi/(z_R - z_{S1})$ rides on top of the DC term of amplitude $[R_R + R_{S1}]/2$ (factors of $\rho S(k)$ are left out for clarity). For multiple reflectors, the cross-correlation component is a superposition of cosinusoids

It is useful to gain an intuitive understanding of the form of (equation 2.21), as well as the effect that different source spectra and different numbers of sample reflectors and their distributions have upon it. For a single reflector, only DC and a single interferometric term are present, and the source spectrum is modulated by a simple cosinusoid whose period is proportional to the distance between the sample and reference reflectors, as illustrated in Figure 2.10. In addition, the amplitude of spectral modulation or "visibility" of the spectral fringes is proportional to the amplitude reflectivity of the sample

reflector $\sqrt{R_{S1}}$. For the case of multiple reflectors, the spectrum is modulated by multiple cosinusoids, each having a frequency and amplitude characteristic of the sample reflection which gives rise to it. In addition, if more than one reflector is present in the sample, autocorrelation components modulated according to the path length difference between the sample reflectors and proportional to the product of their amplitude reflectivities also appear. Since the sample amplitude reflectivities are typically small, these terms are typically small, and also since reflections in the sample tend to be clumped closely together compared to the distance between the sample and the reference reflector, their modulation frequencies tend to be small.

2.2.2. Treatment for time domain low coherence interferometry

In traditional or time-domain OCT (TDOCT), the wavenumber-dependent detector current $I_D(k)$ in (2.21) is captured on a single receiver while the reference delay z_r is scanned to reconstruct an approximation of the internal sample reflectivity profile $\sqrt{R_S(z_S)}$. The result is obtained by the integration of (2.21) over all k:

$$I_D(z) = \frac{\rho}{4}[S_0(R_R + R_{S1} + R_{S2} + \cdots)]$$

"DC Offset"

$$+ \frac{\rho}{2}\left[S_0 \sum_{n=1}^{N} \sqrt{R_R R_{S_n}} e^{-(z_R - z_{S_n})^2 \Delta k^2} cos\left[2k_0(z_R - z_{S_n})\right]\right] \qquad (\mathbf{2.22})$$

"Fringe Bursts"

Here, $S_0 = \int_0^\infty S(k)dk$ is the spectrally integrated power emitted by the light source. The resulting time-domain "A-scan" resulting from such a

measurement is illustrated in Figure 2.11. Note that the sample reflectivity profile convolved with the source coherence function is again recapitulated in the result, resident on a DC offset proportional to the sum of the reference and sample power reflectivities. In addition, the convolved sample reflectivity profile is modulated by a cosinusoidal carrier wave modulation at a frequency proportional to the source center wavenumber k_0 and the difference between reference and sample arm lengths $z_R - z_{S_n}$. Since the reference arm length z_R is typically scanned as a function of time in TD-OCT systems, this carrier provides a convenient modulation frequency for lock-in detection, which provides for high sensitivity detection of the reflectivity envelope and rejection of the DC offset.
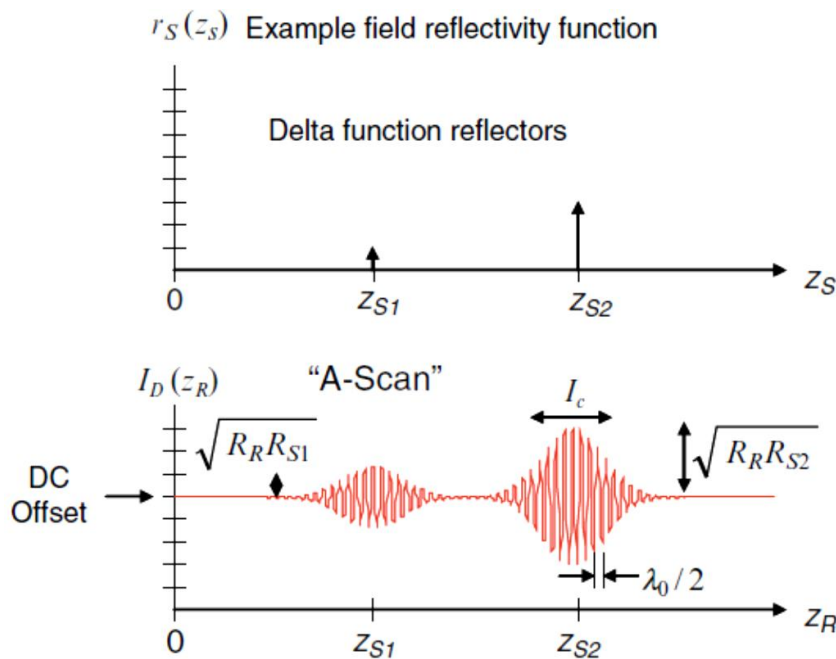
Figure 2.11. Illustration of the example discrete-reflector sample field reflectivity function $r_S(z_S) = \sum_{n=1}^{N} r_{S_n} \delta(z_S - z_{S_n})$ (top), and the A-scan resulting from time-domain low-coherence interferometry.

2.2.3. Treatment for Fourier domain low coherence interferometry

In Fourier domain OCT (FD-OCT), the wave number-dependent detector current $I_D(k)$ in (equation 2.25) is captured and processed using Fourier analysis to reconstruct an approximation of the internal sample reflectivity profile $\sqrt{R_S(z_S)}$. The process for capturing $I_D(k)$ depends upon the experimental details of the detection apparatus. In SD-OCT, a broadband light source is used, and all spectral components of $I_D(k)$ are captured simultaneously on a detector array placed at the output of a spectrometer [8-10]. In SS-OCT, the spectral components of $I_D(k)$ are captured sequentially by recording the signal in a single detector while synchronously sweeping the wave number of a narrowband swept-laser source [25–28].

The sample reflectivity profile $r_S(z_S)$ is estimated from the inverse Fourier transform of $I_D(k)$. Making use of the Fourier transform pair

$$\frac{1}{2}[\delta(z + z_0) + (z - z_0) \overset{\leftrightarrow}{F} \cos kz_0$$

and the convolution property of Fourier transforms

$$x(z) \otimes y(z) \overset{\leftrightarrow}{F} X(k)Y(k),$$

the inverse Fourier transform of (2.9) may be calculated as

$$i_D(z) = \frac{\rho}{8}[\gamma(z)(R_R + R_{S1} + R_{S2} + \cdots)]$$

"DC Terms"

$$+ \frac{\rho}{4}\left[\gamma(z) \otimes \sum_{n=1}^{N} \sqrt{R_R R_{S_n}}[\delta(z \pm 2(z_{R-z_{S_n}}))]\right]$$

38

"Cross-correlation Terms"

$$+\frac{\rho}{8}\left[\gamma(z)\otimes\sum_{n\neq m=1}^{N}\sqrt{R_{S_n}R_{S_m}}\left[\delta(z\right.\right.$$

$$\left.\left.\pm 2(z_{S_n}-z_{S_m}))\right]\right] \qquad (2.23)$$

"Auto-correlation Terms"

Note that the desired sample field reflectivity profile

$$\sqrt{R_S(z_S)}=\sum_{n=1}^{N}\sqrt{R_{S_n}}\,\delta\left(z_S-z_{S_n}\right) \qquad (2.24)$$

is indeed embedded within the cross-correlation terms of (equation 2.23), although it is surrounded by several confounding factors. Carrying out the convolutions by taking advantage of the sifting property of the delta function, we obtain the result of the interferometric measurement, referred to as the "A-scan":

$$i_D(z)=\frac{\rho}{8}\left[\gamma(z)(R_R+R_{S1}+R_{S2}+\cdots)\right]$$

$$+\frac{\rho}{4}\sum_{n=1}^{N}\sqrt{R_R R_{S_n}}\left[\gamma\left[2(z_{R-}z_{S_n})\right]+\gamma\left[-2(z_{R-}z_{S_n})\right]\right]$$

$$+\frac{\rho}{8}(z)\sum_{n\neq m=1}^{N}\sqrt{R_{S_n}R_{S_m}}\left[\gamma\left[2(z_{S_n}-z_{S_m})\right]+\gamma\left[-2(z_{S_n}-z_{S_m})\right]\right] \quad (2.25)$$

The results in (equation 2.23) and (equation 2.25) for the example of discrete sample reflectors and a Gaussian-shaped source spectrum are plotted in Figure 2.12. As can be seen in the figure, the sample field reflectivity profile,

$$\sqrt{R_S(z_S)}=\sum_{n=1}^{N}\sqrt{R_{S_n}}\,\delta\left(z_S-z_{S_n}\right) \qquad (2.26)$$

is reproduced in the cross-correlation terms with the following modifications.
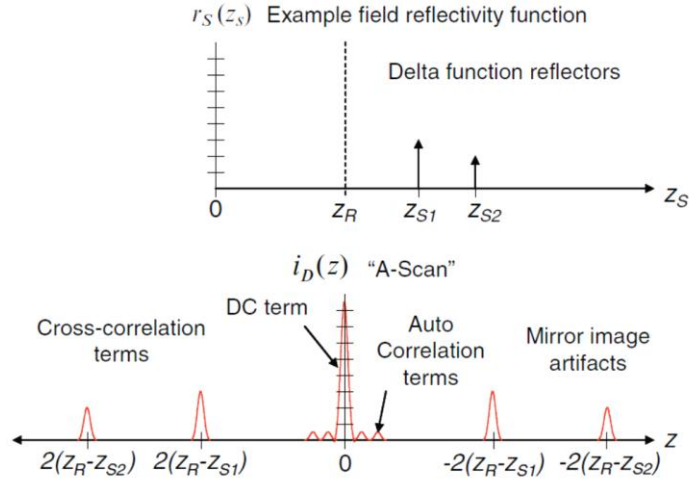
Figure 2.12. Illustration of the example discrete-reflector sample field reflectivity function $R_S(z_S) = \sum_{n=1}^{N} R_{S_n} \delta(z_S - z_{S_n})$ (*top*), and the A-scan resulting from Fourier domain low-coherence interferometry.

First, the zero position of the reflectivity profile appears at the position of the reference reflector z_R, rather than the position of the BS. Second, the apparent displacement of each sample reflector from the reference position is doubled (which can be understood from the fact that the interferometer measures the round-trip distance to each reflector). We accommodate this by defining a new single-pass depth variable $\bar{z} = 2z$. Third, each reflector appears broadened or blurred out to a width of about a coherence length by convolution with the function $\gamma(z)$. This is precisely the definition of an imaging system PSF. Given the inverse relationship of the coherence length to the light source bandwidth, the clearest path to increase the fidelity of the estimate of $\sqrt{R_S(z_S)}$ is to use as broad bandwidth sources as possible. Fourth, the magnitude of the detected sample reflectivity, which can be very small, is amplified by the large homodyne gain factor represented by the strong reference reflectivity $\sqrt{R_R}$. All the modifications listed so far can be dealt with through proper interpretation of the data, i.e., realization that the zero position corresponds to the position of the reference reflector, relabeling axial distances to account for the factor of 2, and accounting for the homodyne gain factor.

A number of additional modifications to the field reflectivity profile are termed artifacts and are more serious. First, as seen in the cross-correlation terms in (equation 2.23) and (equation 2.25), a mirror image of the blurred version of $\sqrt{R_S(z_S)}$ appears on the opposite side of zero pathlength, i.e., the reference reflector position. This is termed the complex conjugate artifact in FD-OCT, and is simply understood from the fact that since the detected interferometric spectrum is necessarily real, its inverse Fourier transform must be Hermitian symmetric, i.e., its positive and negative distances are complex conjugates of each other and therefore if they are real, they must be identical. This artifact is not serious so long as the sample can be kept entirely to one side of zero path length, in which case it can be dealt with by simply displaying only the positive or negative distances. However, if the sample strays over the zero path length border, it begins to overlap its mirror image, an effect that cannot be removed by image processing alone. A number of approaches are under development for removing this complex conjugate artifact [15-22].

Additional image artifacts also arise from the DC and auto-correlation terms in (equation 2.23) and (equation 2.25). The DC terms give rise to a large artifactual signal centered at zero pathlength difference. The FWHM value of the DC artifact is only one coherence length wide; however, the signal amplitude is so much larger than the desired cross-correlation terms that the wings of the Gaussian-shaped PSF from (equation 2.19) can overwhelm desired signal components much farther away. Since the largest component of the DC artifact comes from the reference reflector (with reflectivity near 1), a simple method to eliminate that component is to record the amplitude of the spectral interferometric signal (equation 2.21) with the reference reflector but no sample present, then to subtract this signal component from each subsequent spectral interferometric signal acquired. The autocorrelation terms in (equation 2.23) and (equation 2.25) also give rise to artificial signals at and near the zero

41

pathlength position, since the distance between reflectors in a sample is typically much smaller than the distance between the sample reflectors and the reference arm path length. The best method to eliminate the autocorrelation signals is to ensure that the reference reflectivity is sufficient so that the amplitude of the autocorrelation terms is very small compared to the cross-correlation terms.

2.2.4. Lateral resolution
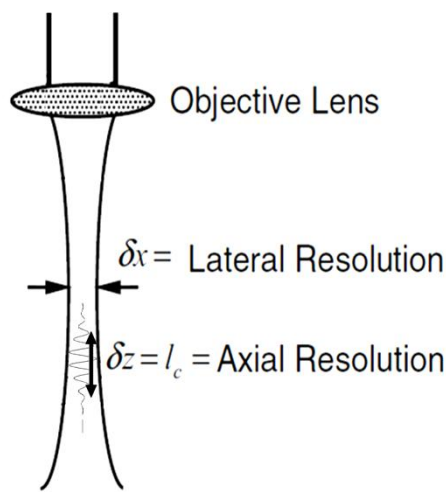
Figure 2.13. Sample arm beam.

Lateral resolution of OCT system is given by

$$\Delta x = \frac{4\lambda_0}{\pi} \left[\frac{f}{d}\right] \tag{2.27}$$

where, f is the focal length of sample arm adjective lens and d is the beam diameter. λ_0 is the central wave length of low coherence light source.

2.3. Speckle phenomena

2.3.1. Light interaction with biological tissue

Light interacts with matter in various ways, Figure 2.14. The different processes that occur depend on the wavelength of the light as well as the structure of the medium. Light can be reflected, scattered or absorbed when it interacts with the matter. Photons with very high energy, like gamma and x-rays, may even ionize atoms or break bonds in the molecules, but this will not be the case in this work since low energy light source is being used through all the experiments.
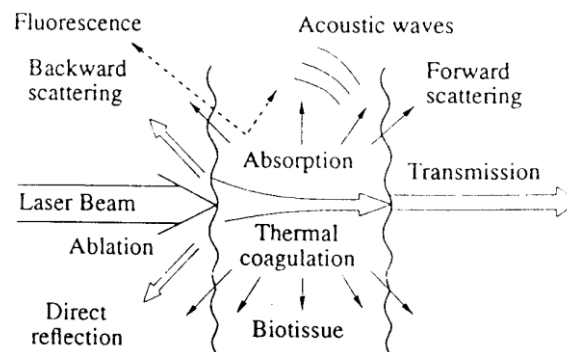
Figure 2.14. Various interactions between light and matter [26].

The reflection of the light, when it enters a border between different refractive indexes, obeys the laws of Snell and Fresnel. It depends therefore on the refractive indexes as well as the angle of the incoming and the reflected rays:

$$n_1 \times \sin \varphi_1 = n_2 \times \sin \varphi_2 \text{ (Snell)} \tag{2.28}$$

$$R = \frac{1}{2} \left[\frac{\sin^2(\varphi_1 - \varphi_2)}{\sin^2(\varphi_1 + \varphi_2)} + \frac{\tan^2(\varphi_1 - \varphi_2)}{\tan^2(\varphi_1 + \varphi_2)} \right] \text{ (Fresnel)} \tag{2.29}$$

n_1, n_2 are the refractive indexes in the two materials and φ_1, φ_2 the angles of the light perpendicular to the boundary.

The scattering can be either elastic or inelastic. Elastic means that the scattered photons neither loose nor gain energy in the process. The types of elastic scattering are Rayleigh and Mie. In Rayleigh scattering, the electromagnetic field of the incoming light induces a polarization of the molecule, which "re-radiates" the light with retained wavelength and without delay. This appears when the particles in the substance are about the same size as or smaller than the wavelength of the light, Figure 2.15. The cross section for this process is about 10^{-26} cm^{-2} and proportional to λ^{-4} [27], which means that it increases as the wavelength decreases. This involves, for instance, that the blue light from the sun is scattered on the molecules in the air more than the red light, and therefore makes the sky look blue.
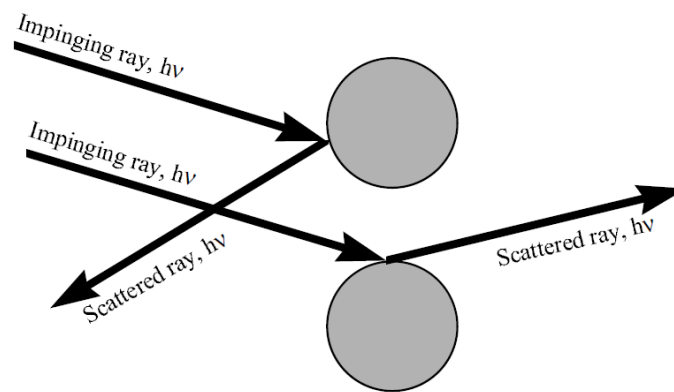
Figure 2.15. Rayleigh scattering on particles.

If the particles on the other hand are bigger than the wavelength, there will be Mie scattering. In this case a ray simply penetrates the wall of the particle and reflects one or several times against the inside of the wall before it leaves the particle, Figure 2.16. Examples of this are the bad visibility in fog and the rainbow in the clouds. In the latter example, the sunlight scatters in the water drops in the clouds. As the sunlight consists of a wide spectra, the drops

in the clouds will operate as small prisms which scatter the different wavelengths in different angles to the sun, and there will be a rainbow. The cross section for Mie scattering depends very much on the sizes and refractive indexes of the particles and the surrounding media. It varies therefore between about 10^{-26} and 10^{-8} cm^{-2} [27]. The probability of the effect is proportional to λ^{-2} and is hence not as wavelength dependent as Rayleigh scattering.
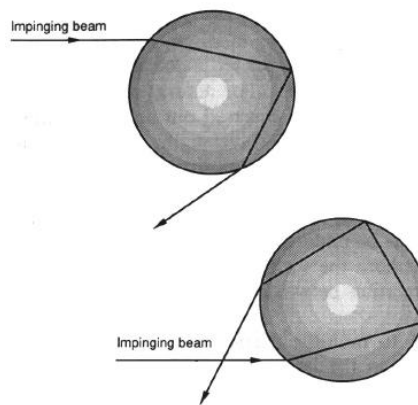
Figure 2.16. Mie scattering in particle.

The strongest inelastic effects in scattered light are Raman and Brillouin. Raman is a special case of Rayleigh scattering. The difference appears when the molecule reradiates the light. The excited electrons fall back to another energy level than where they were before the polarisation, Figure 2.17. This gives wavelengths shifted certain energies, up or down, from the wavelength of the incoming light, specific for each bond in the medium. Hydrogen has the largest shift and changes the energy 4155 cm^{-1}, but the most common shifts are 100-1000 cm^{-1} [28]. The cross section for Raman scattering is about 10^{-29} cm^{-2}.
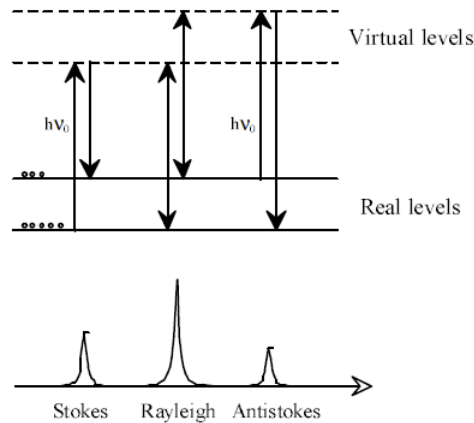
Figure 2.17. Raman shifts of the scattered light [27].

Brillouin scattering appears when a crystal is deformed by a long acoustic phonon. The refractive index of the crystal changes due to the tension that is induced by the vibration. Consequently, if a phonon is present it will affect the shifts and directions of all the photons it encounters. The size of the changes, depends on the resonance frequencies of the setup and hence the characteristics and size of the object, the laboratory, the equipment and the phonon. The absorption process is a very complex part of the interaction. The different atoms and molecules in the matter have a wide range of possible energy levels which can be excited. After a certain time delay, also depending on the type of atoms or molecules, they lose energy by either producing heat, contributing to some photochemical reaction or re-radiate photons in any direction, called fluorescence. These photons may have the same wavelengths as the incoming rays but also other, depending on the probability for the occupation of the different energy levels. All this information is specific for each medium and is therefore a good source when working with spectroscopy to extract information concerning the characteristics of the substance. On the other hand, since this study is depending on the correlation of the scattering in different media, the re-radiation may instead be a source of noise. The probabilities for absorption and fluorescence are both normally about $10^{-16}\,cm^{-2}$.

46

However, in liquids and solids at atmospheric pressure the molecules will be close enough to bounce in to each other and stimulate the segregation of heat. This is called quenching and reduces the probability of fluorescence to about $10^{-20}\,cm^{-2}$ [27].

2.3.2. Composition and structure of biological tissue

All biological tissue consist of cells. Figure 2.18 shows a typical vegetable cell, its basic elements and their sizes. The diameter of the cell is about 0.1 mm. The cell wall is a 30 nm thick layer of polysaccharides and proteins that will stretch as the cell grows and eventually deteriorate and break as the cell dies. In the cell there are several nuclei with the size of about 0.5 µm which includes the DNA. The mitochondria have about the same size as the nuclei and control the respiration of the cell, as it provokes the oxidation of nutrients. There are also larger parts, chloroplasts, which are the engines of the cells. They are a few µm in diameter, contain chlorophyll and are responsible for the production of energy. The ligament that glues the particles together consists of endoplasmic reticulum which produces and transports proteins to the membranes. The biggest part of the cell is the vacuole, which is a reservoir of water, sugars, pigments, oxygen and carbon dioxide. It is the part that expands the most and makes the cell grow.
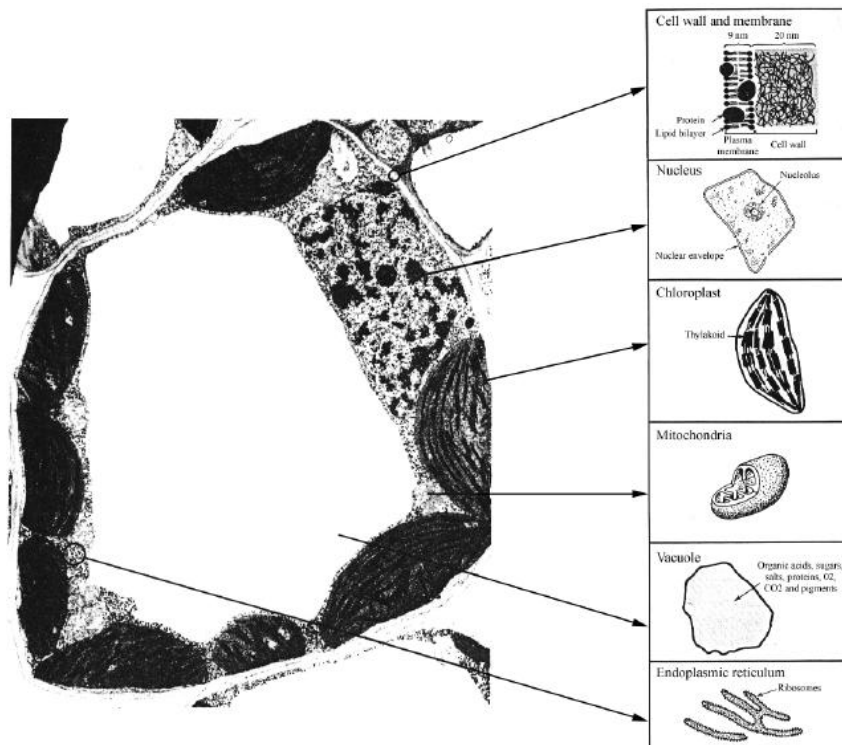
Figure 2.18. Vegetable cell [29].

The cells stick to each other like bricks in a wall, even though there is inter-space between some of them. This space may be filled with air or loose subparts of cells. The tissue has a 50 μm thick layer of surface cells that are called epidermal cells. The surface is normally covered with wax, small fluff called trichomes and pigments to moderate the wavelengths that penetrate it. Leaves which have been extensively studied have more layers. Their next layer is called palisade and is about 1 mm thick. Underneath is the spongy layer which has about the same thickness [30]. The distribution of chloroplasts is not homogenous right the way through the tissue. It highly depends on the type of vegetable and where it grows. When it grows in the shade and is reached by diffuse light, it needs another distribution than if it receives direct collimated light. It also has a movement of the chloroplasts, called cyclosis, to adjust the absorption of light. There is even a movement of whole cells to use the light as effectively as possible. As the light penetrates the tissue, the intensity decreases

with the depth and the cells turn towards the highest gradient of the light. In other words, the biological tissue is not a "vegetable", it is actively working to influence light propagation and absorption to its own advantage.

2.3.3. Optical properties of biological tissue
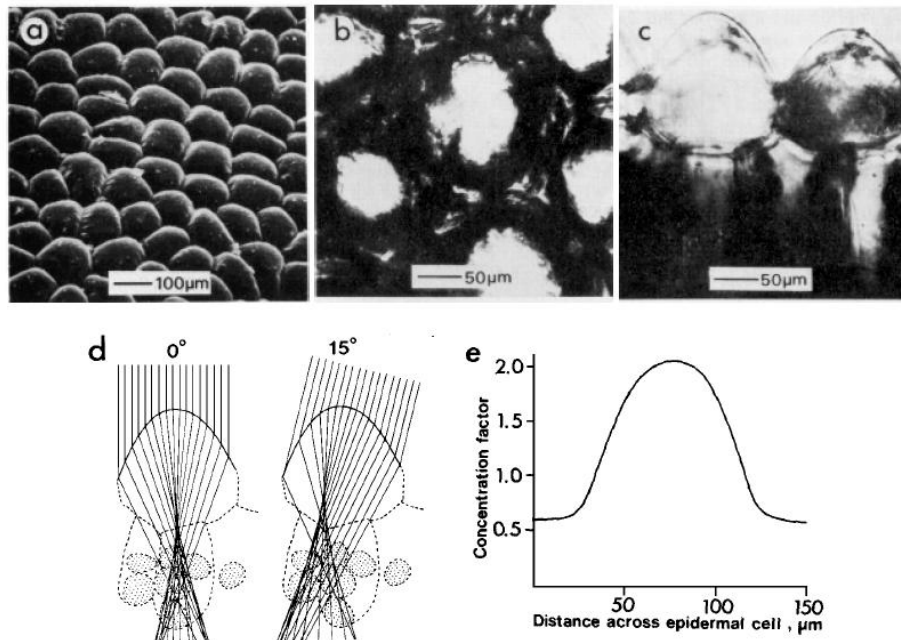
Figure 2.19. (a) Surface of vegetable showing cells. (b,d) Cells (seen from above) focusing light towards their centers. (c) Cells (seen from the side) focusing light. (e) Intensity concentration in cells. [31].

Any transparent matter with a curved surface and a refractive index higher than air, can focus light. Tissue has absorption centers, consisting of so called chromophores. It is in these centers that the tissue can optimize its use of light, consequently cells concentrate the incoming light to these areas. This is particularly important for leaves because they are thin and need to create a lot of energy to support the plant. Figure 2.19 shows epidermal cells of a tropical plant, living in the shade, with very strong focusing. Even though it is hard to imagine a lens effect in a matter with multiple scattered light, calculations of radiation within maize mesocotyls, the first leaves of the sprout, indicate that focusing further into the tissue could exist [24]. Obviously the electromagnetic

field in biological tissue is very heterogeneous and the concentrations of light vary a lot. Let us now reason microscopically about the scattering with the above mentioned types of interactions with matter; reflection, scattering and absorption. As the tissue has a higher refractive index than air, there will be a reflection on the surface. The light that penetrates however, may therefore also be trapped inside. If polarized light is used, it will lose its polarization at a high exponential rate as it penetrates the tissue. Therefore approximately all the light that is reflected back with kept polarization comes from the reflection in the surface [23,24]. During a study, when illuminating biological tissue with polarized light, researchers found that the polarization in the specular direction of observation was 0.98 due to the reflection in the surface but only 0.17 in a 0°/30° setup (similar to the one that is used in this study). The refractive indexes are different inside and outside the cells as well as in all the cell parts and in the cell wall. The indexes of different vegetable cell walls have been investigated with results between 1.333-1.472 and with an average of 1.425 [25]. This means that the back scattered light from biological tissue not only is multiple scattered, but is also multiple reflected on different surfaces.
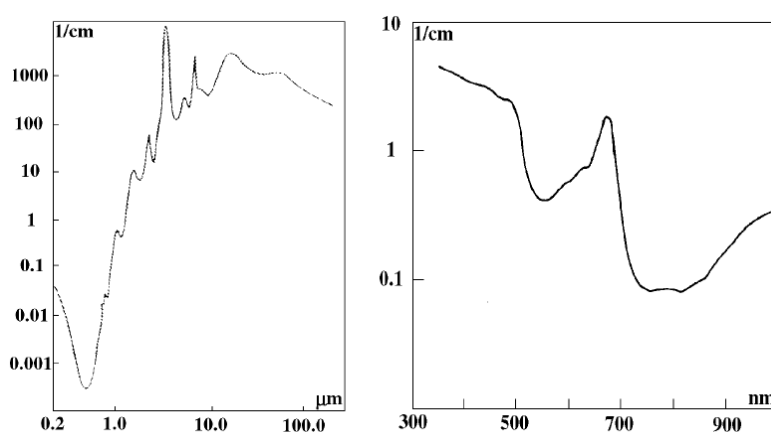
Figure 2.20. Light absorption in water (left) and chlorophyll (right).

Biological tissue is a highly scattering media. The sizes of the cells, the vacuoles and spaces between cells are a bit larger than the wavelength of a

HeNe-laser. Thus they are probably participating in Mie scattering, which consequently is very strong with a cross section comparable with the absorption, 10^{-16} cm^{-2}. All the other parts as well as all the molecules are participating in the Rayleigh scattering. The cross section for Rayleigh scattering, 10^{-26} cm^{-2}, is however small compared to that for Mie scattering. This also leads to that the Raman effect is very small as the cross section is about 10^{-29} cm^{-2}. There is also Brillouin-scattering in biological tissue even though it is not as strong as in a crystal. These effects will cause direct or indirect shifts and broadenings in the scattered light.

The absorption is wavelength dependent and varies a lot. Due to that the main absorbers are water and chlorophyll, the absorption spectrum mainly depends on them. In Figure 2.20, the absorption spectra for water and chlorophyll are illustrated. Note that they have different scales of wavelength. We can see that water absorbs a lot in the infrared region, yet it has a window at around 0.6 μm. A HeNe-laser is therefore a good source to use if you do not want to get your signal absorbed by water. The chlorophyll naturally absorbs of course a lot in the visible range, since that is its main purpose. One of the chlorophyll's absorption peaks coincides with the wavelength of the laser, 633 nm. This greatly facilitates measurements of the amount of chlorophyll in an object. When measuring speckles, a strong absorption does not cause important problems. However, when measuring an object where the quantity of chlorophyll changes a lot, changes in the speckle size may occur with time as less absorption involves deeper penetration of the light. By using a diaphragm, it is possible to get rid of this problem since this method keeps the speckle size constant. Most of the absorbed energy will turn into heat but the change of temperature will probably not be important even though there is a strong absorption.
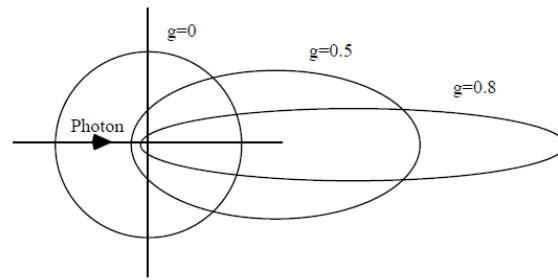
Figure 2.21. The probability for a photon to be scattered in certain directions for different values of g.

The most common way of describing the properties of a medium is with the absorption coefficient, μ_a, and scattering coefficient, μ_s. To get the total coefficient, the two are coupled to define the linear transport coefficient $\mu_{tr} = \mu'_s + \mu_a \times \mu'_s$ is the reduced scattering coefficient $\mu'_s = (1 - g)\mu_s$ which depends on the anisotropy factor g. g is the mean cosine of the scattering angle and can obtain values between -1 and 1. g=1 is pure forward scattering and g=0 is uniform scattering, Figure 2.21. Human tissue, for example, has a typical value of the factor g=0.7-0.95 [32].

2.3.4. Laser Speckles

In the early 1960's, when continuous wave lasers first became commercially available, researchers working with the instruments noticed what at the time was regarded as a strange phenomenon. When laser light was reflected from a surface such as paper or the wall of the laboratory, a high contrast, time scale granular pattern would be seen by an observer looking at the scattering spot.

In addition the random intensity distributions that now call a speckle pattern Figure 2.22 (a), is formed when fairly coherent light is reflected from a rough surface. For example rough surface is illuminated by a laser light as shown in Figure 2.22 (b), the place under illumination will be a spot with a

granular appearance. Further speckle can arise light is propagates through a medium with random refractive index fluctuations [33]. Further, measurement of the intensity reflected from such a spot showed that fine scale fluctuations of the intensity exists in space, even though the illumination of the spot was relatively uniform.

The surface of the most materials are extremely rough on the scale of an optical wavelength ($\lambda \approx 5 \times 10^{-7}$ m). When nearly monochromatic light is reflected from such a surface, the optically wave resulting at any moderately distant point consists of many coherent components or wavelets, each arising from a different microscopic element of the surface. With reference to Figure 2.22 (b), the distances travelled by these various wavelets may differ by several or many wavelengths if the surface is truly rough. Interference of the de-phased, but coherent wavelets results in the granular pattern of intensity that is call speckle [34].
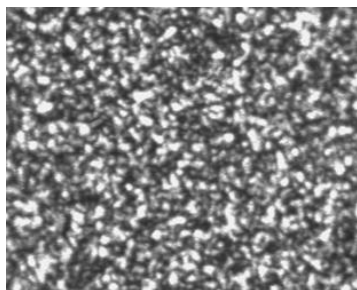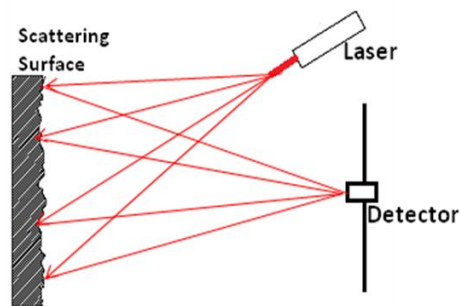
(a)   (b)

Figure 2.22. (a) Speckle pattern (b) Laser illumination of a rough surface.
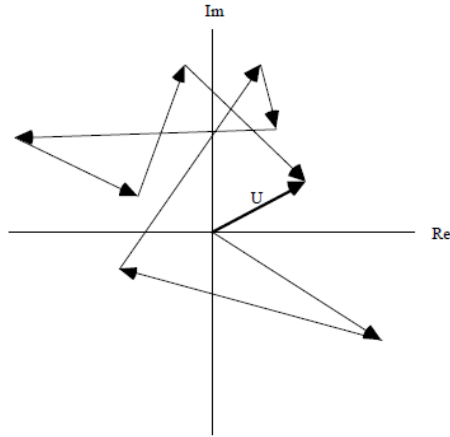
Figure 2.23. The complex sum of rays that create a spot in a speckle pattern.

In each point in the speckle image, the light from many scatterers are superposed and therefore complexly added. The resulting intensity is

$$A(P,t) = \sum_{j=1}^{N} |A_j(P,t)| \exp[i\phi_j(P,t)]$$

(2.32)

where A is the phase amplitude, P the observation point and N the number of scatterers that contribute to A in P. Compare with the complex addition in Figure 2.23. This is identical with the random walk problem in two dimensions [35].

For example, if you look at the spot, your retina will be one of these planes, as in the example above. As many waves from different parts of the spot interact, they all have different phases, creating an intensity consisting of their complex sum, Figure 2.23 and equation 2.32. The intensity function, which is a result from a ray-tracing function, is an exponential function [33];

$$P_I(I) = \frac{I}{<I>} e^{\left(\frac{I}{<I>}\right)}$$

(2.30)

where $P_i(I)$ is the probability of a certain intensity I. The intensity with highest probability is 0, the mean intensity $<I>$, and for higher values it falls off rather quickly. This means that the variations of the intensities are not very big and therefore sensitive to noise. The size of each speckle follow the law of Airy:

$$d = 2 \cdot 1.22 \left(\frac{\lambda \cdot z}{D} \right)$$

(2.31)

where d = diameter of speckles, z = distance of observation and D = diameter of circular area observed.

2.3.5. Biospeckles

When speckles are created from light scattered by moving particles, the speckles are modulated by the state of motion of the scatterers. This makes the speckle pattern time varying and thus the speckles are called temporal. It actually gives the speckles a boiling appearance and they are therefore sometimes referred to as boiling speckles. When the speckles originate from biological specimen the speckles are called biospeckles [34]. Biospeckles stern from a very complex phenomenon. When the light penetrates the object it is multiple scattered in all possible directions before leaving the object. Consequently it is not possible to recognize and study each particle that scatters the light.

The frequency of the speckle fluctuations are hence directly related to the rate of change in the random walk and therefore the velocity of each scatterer. The effect can be compared with the Doppler method where a very narrow laser beam illuminates a vessel and the velocity (v) of the fluid in the vessel is given from the frequency of the fluctuating scattered light:

$$f_D = \frac{1}{2\pi}(\overline{K}_s - \overline{K}_i) \cdot \overline{v}$$

<div align="right">

(2.33)

</div>

where K_s and K_i are the wave vectors for the incident and the scattered light. In our case every scatterer has this Doppler phenomenon, but the directions of the movements do not matter. Because of the complexity of the scattered light there has not yet been established accurate mathematical methods to describe this. However, the different wave vectors, velocity vectors and the multiple scattering all together may statistically be interpreted as a Doppler broadening of the scattered light [36]. A problem is that a part of the broadening is a pure random signal superposed with the Doppler broadening. A method to get rid of this noise is to measure the evolution of many speckles and use the mean value of them all.

2.3.6. Properties of biospeckles

The two most interesting dimensions of the speckles are size and intensity. The size of the stationary speckles are, as mentioned above, equal to the Airy disc resulting from the size of the illuminated area. But what happens with the size of the speckles as the light penetrates the object and is multiple scattered? Studies have been conducted to investigate the properties of time varying speckles. It has been shown that the speckles resulting from scattering inside an object have a smaller average size than the ones produced from scattering on the surface [23]. This can easily be explained with the expansion of the laser beam as it penetrates the object. As the light is scattered back, it leaves the object through a larger area than where it entered. In other words, the Airy law is still valid but with the actual size of the illuminated area rather than the width of the laser beam. The speckle pattern is actually superposed of two different patterns. Large speckles, resulting from scattering on the surface and with a large angular dependence, are modulated by small speckles, from the

light from the interior with very weak angular dependence [37]. In article [23], experiments with apples were made and the ratio of the sizes of the speckles was found to be 1:10. The same researcher showed with apertures that the speckle size increases with the decreasing diameter of the aperture and also that the rate of temporal changes of the speckles decreases with decreasing aperture size. The time varying effect of the speckles is also stronger far away from the direction of the specular reflection [23].

Another property is the size of the region reached by light in the object when illuminating with a very thin laser beam. It has the following dependence on the depth:

$$D = D_0 \left[1 - \exp\left(-\frac{T}{T_0} \right) \right]$$

(2.34)

D is the diameter of the region and T is the depth. In the experiments with apples [23], $D_0 = 20$ mm and $T_0 = 1.6$ mm were empirically found, which give an illuminated area that can be illustrated like in Figure 2.24. A depth of about 7 mm was found to be the maximum depth from where the scattered light contributes to the speckle pattern. It was discovered that the temporal speckle variations come mainly from scatterers within a few mm depth [23].
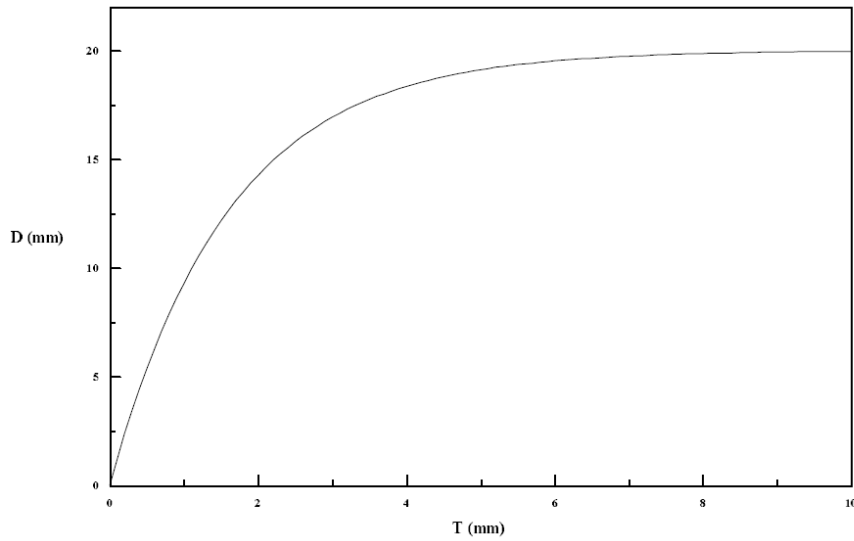
Figure 2.24. Diameter of region reached by light, D, as a function of depth in the matter, T.

The speckle is a stochastic effect and can therefore be described only statistically. There are many statistical approaches and several of them are evaluations from the concepts of first and second order statistics. The first order is the statistical description of the contrast of speckles in a pattern in one single image. This approach shows that the standard deviation, σ, of the spatial intensity is the mean intensity, $< I >$, of the speckle pattern. The contrast may be expressed as $\sigma_2 < I >_2$ and when this ratio is 1, the pattern has a maximum contrast and is therefore fully developed [38]. This of course depends on the time the image is exposed. With a very long exposure, the image will become unclear, resulting in a very low contrast. However, with the knowledge of the time, the contrast and the ratio of moving scatterers to stationary ones, it is possible to determine the mean velocity of the scatterers. This technique can be used for example to visualize blood flow in the retina and to study vibrations [39]. The second order statistics is a description of the size and intensity distributions of the speckles in an image. The method involves taking the autocorrelation of the image to determine the sizes. This technique is also used

58

to determine the changes of intensity in one single pixel by taking the autocorrelation of its time history.

In recent years speckle pattern has been used variety of applications. The most obvious application is to the measurement of surface roughness. Another related application of speckle pattern is the study of displacements and distortion that arise in non-destructive testing of mechanical components (Speckle interferometry and speckle photography). Further they are utilized for in astronomy, examine the reflection state of reflection of the eye, test patterns for optical and other recording systems, etc. Like that there are many useful applications in the speckle pattern.

As in earlier explanation speckles appear as a result of random interference of the scattered light by a rough surface object under the illumination of a coherent light such as a laser beam. The speckles were considered as a noise in the early advent of lasers. However, its use in investigating biological phenomenon such as blood flow measurements, biological activates of living substances, noninvasively has made them to be realized as an important making them no longer a random noise.

Reference

1. Hariharan P, (1985) "Optical Interferometry," Academic Press, Sydney.

2. Jiang Z, Staude W, (1989) "An Interferometric Method for Plant Growth Measurements," Journal of Experimental Botany 40, 1169-1173.

3. Kobayashi K, Kadono H, (2010) "Expansion of the dynamic range of statistical interferometry and its application to extremely short to long-term plant growth monitoring," Applied Optics 49: 6333-6339.

4. Born M, Wolf E, (1999) "Principle of Optics: Electromagnetic theory of propagation, Interference and Diffraction of light," Oxford University Press, Cambridge.

5. Hecht E, "Optics," Addison-Wesley, 4th edition.

6. Rollins A M, Izatt J A, (1999) Opt. Lett. 24(21), 1484.

7. Podoleanu A G, (2000) Appl. Opt. 39(1), 173.

8. Fercher A F et al., (1995) Opt. Commun. 117(1-2), 43.

9. Hausler G, Lindner M W, (1998) J. Biomed. Opt. 3(1), 21.

10. Wojtkowski, M. et al., (2002) J. Biomed. Opt. 7(3), 457.

11. Chinn S R, Swanson E A, Fujimoto J G, (1997) Opt. Lett. 22(5), 340.

12. Golubovic B et al., (1997) Opt. Lett. 22(22), 1704.

13. Lexer F et al., (1997) Appl. Opt. OT 36(25), 6548.

14. Haberland U H P, Blazek V, Schmitt H J, (1998) J. Biomed. Opt. 3(3), 259.

15. Wojtkowski M et al., (2002) Opt. Lett. 27(16), 1415.

16. Leitgeb R A et al., (2003) Opt. Lett. 28(22), 2201.

17. Choma M A, Yang C, Izatt J A, (2003) Opt. Lett. 28(22), 2162.

18. Yun S H et al., (2004) Opt. Exp. 12, 4822.

19. Gotzinger E et al., (2005) Opt. Exp. 13(2), 583.

20. Sarunic M V et al., (2005) Opt. Exp. 13, 957.

21. Davis A M, Choma M A ,Izatt J A, (2005) J. Biomed. Opt. 10(6), 064005.

22. Zhang J, Nelson J S, Chen Z P, (2005) Opt. Lett. 30(2), 147.

23. Xu Z, Joenathan C, Khorana B M, (1995) "Temporal and spatial properties of the time varying speckles of botanical specimens," Optical engineering vol. 34, no. 5, pp. 1487-1502.

24. Vogelmann T C, (1993) "Plant tissue optics," Annu. rev. plant physiol. plant mol. biol. vol. 44, pp. 231-251.

25. Gausman H W, Allen W A, Escobar D E, (1974) "Refractive index of plant cell walls, "Applied optics vol. 13, no.1, pp. 109-111.

26. Tuchin V V, (1993) "Lasers and Fiber Optics in Biomedicine," Laser Physics vol. 3, no. 4, pp. 767-820.

27. Svanberg S, (1992) "Atomic and molecular spectroscopy," Springer-Verlag.

28. Bass M, (1995) "Handbook of optics I,", 2nd ed., McGraw-Hill Inc.

29. Lehninger A L, (1981) "Bioquímica, Las bases moleculares de la estructura y función celular," 2nd ed. Worth publishers, inc.

30. Seyfried M, Fukshansky L, (1983) "Light gradients in plant ti ssue," Applied optics vol. 22, no. 9, pp. 1402-1408.

31. Bone R A, Lee D W, Norman J M, (1985) "Epidermal cells functioning as lenses in leaves of tropical rain-forest shade plants," Applied optics vol. 24, no. 10, pp. 1408-1412. 54.

32. Berg R, (1995) "Laser-based cancer diagnostics - Tissue optics considerations," Lund reports on atomic physics, LRAP-184.

33. Dainty J C, (1975) "Laser Speckle and Related Phenomena," Springer-Verlag, Berlin.

34. Aizu Y, Asakura T, (1996) "Trends in Optics," (San Diego: Academic Press) pp27–49.

35. Goodman J W, (1984) "Statistical properties of laser speckle patterns," Laser speckle and related phenomena, Dainty J C, ed., vol 9 of Topics in Applied physics, Springer-Verlag, Berlin, pp. 9-75.

36. Drain L E, (1980) "The laser doppler technique," chap. 4, p. 70, Wiley, New York.

37. Briers J D, (1975) "Wavelength dependence of intensity fluctuations in laser speckle patterns from biological specimens," Opt. commun. vol. 13, pp. 324-326.

38. Goodman J W, (1984) "Statistical optics," Wiley, New York.

39. Briers J D, (1993) "Speckle fluctuations and biomedical optics: implications and applications," Optical engineering vol. 32, no. 2, pp. 277-283.

CHAPTER 3

3. Application of developed fOCT biospeckle signal analysis to monitor O_3 stress on plants

In this study, we proposed, developed, and applied fOCT, based on biospeckle signal, to monitor the biological response of plants for O_3 stress. In the experiments, *Allium tuberosum,* commonly known as Chinese chives was exposed to 0, 80, 120, and 240ppb O_3 concentrations, and the effects to both back and front side of the leaf were observed to validate the developed fOCT biospeckle imaging and signal analysis for functional changes inside the leaf. Experimental data were analyzed by our first approach. In addition, separate experiments were conducted with Chinese chives under 240ppb of O_3 exposure

and biospeckle signals of different depth positions were analyzed with our second approach. Since the fluctuation of the biospeckle signal reflects biological activities inside the tissue, the signals coming from different layers were analyzed for magnitude of fluctuation and temporal characteristics. Significant increment in magnitude was found in the epidermal layer while changes in mesophyll cell layer was identified by it temporal characteristics.

3.1. Optical System and Method

3.1.1. Optical System

Figure 3.1. Experimental setup of the spectral domain optical coherence tomography system used in this study. SLD-super luminescent diode, L1~L6-lenses, M1-mirror, PC-polarization controller, DAQ-data acquisition device, IMAQ-image acquisition device.

Figure 3.2. Photograph of spectral domain optical coherence tomography system used in this study. (1)-SLD, (2)-grating, (3)-line scan camera, (4)-sample arm, (5)-reference arm, (6)-polarization controller, (7)-circulator, (8)-fiber coupler, (9)-sample arm objective lens,

SD-OCT system was set up in this work to achieve high resolution OCT imaging. The schematic diagram of our SD-OCT system is shown in Figure 3.1 (Figure 3.2). The light source used in the system is a super luminescent diode (SLD) with a central wavelength 836.1nm and a band width of 55.2nm. Identical lenses were placed in the sample and reference arms to cancel dispersion mismatch in the two arms. The coupler splits, 99% of the incident power from the SLD to the sample and 1% to the reference mirror. The backscattered light from the sample and the light reflected from the reference mirror are recombined by the coupler. By means of a circulator, those lights are guided to the spectrometer consisting of a collimator and grating. The collimated light by lens L5 enters grating and the spectral interference signal is obtained by the line-scan camera through lens L6 (focal length is 200mm).
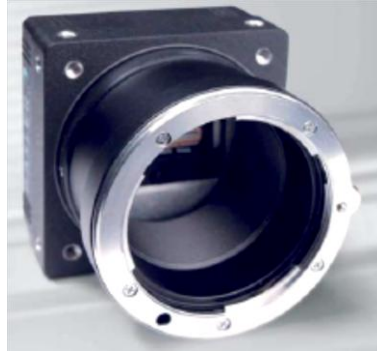
Figure 3.3. Line scan CCD camera used in this study (L104k-2k, BASLER, Germany).

Table 3.1. Specifications of line scan camera used in the study.

Specifications	L101k
Sensor	2048 pixel linear CCD Thomson TA7813
Pixel Size	10 µm x 10 µm (10 µm pitch)
Spectral Response	300 - 1000 nm, peak at 700 nm (See Figure 1-1)
Pixel Depth	Programmable 8 bit or 10 bit
Video Output Formats Single	8 Bit, Single 10 Bit, Dual 8 Bit, or Dual 10 Bit
Synchronization	Via external ExSync signal or free-run
Exposure Time Control	Edge-controlled, level-controlled, or programmable
Power Requirements	12 VDC ± 10%, max. 6.5 W

We used a line scan CCD camera (L104k-2k, BASLER, Germany) with 2048 pixels and acquisition rate of 25,000 lines per second (Figure 3.3, and Table 3.1). The axial resolution (depth resolution) was estimated to be 6µm and the lateral resolution was estimated to be 22µm. A galvanomirror-scanner in the sample arm permits a lateral scanning in x and y directions. One image of the size 1024×2500 pixels was acquired with an acquisition rate of 10 frames per second. The incident power delivered to the leaf sample was approximately

5mW, that gave an irradiance lower than the damage threshold for plant leaves [1].
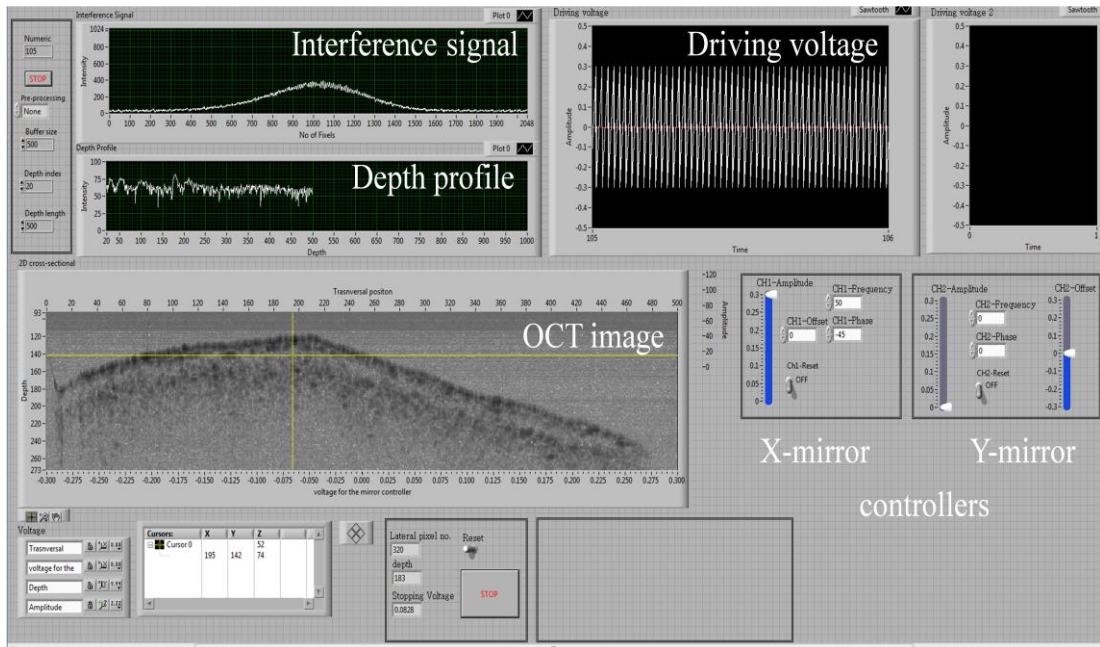
Figure 3.4. Screenshot of front panel window of the developed software.

A Software program (LabVIEW 2011, National Instruments, USA) was developed (Figure 3.4) to combine OCT system and to acquire OCT imaging data and biospeckle signals data from interested spatial positions. Driving voltages for galvanomirror-scanners were given through a data acquisition device (DAQ, PCIe-1429, National Instruments, USA) and imaging data from line scan camera was taken by a image acquisition device (IMAQ, PCIe-6351, National Instruments, USA).

3.1.2. Plant and ozone exposure system
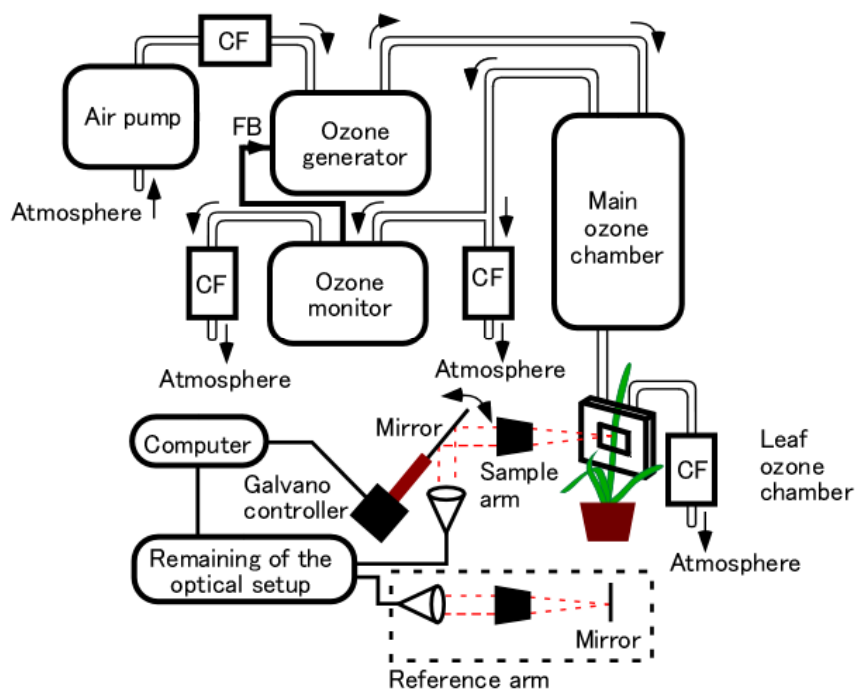
Figure 3.5. Schematic of O_3 exposure system and simplified sketch of SD-OCT system used in this study. CF-charcoal filter, FB-Feedback signal.
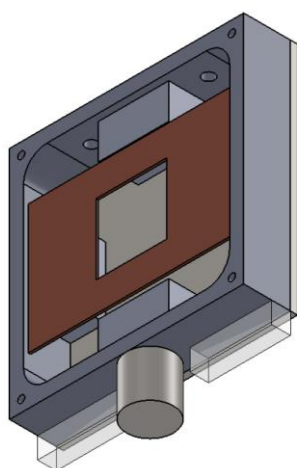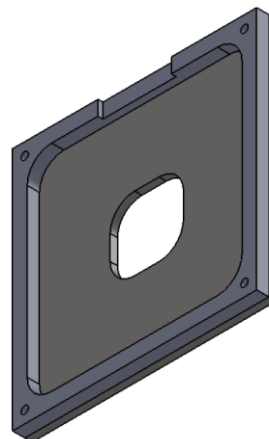
(a)   (b)
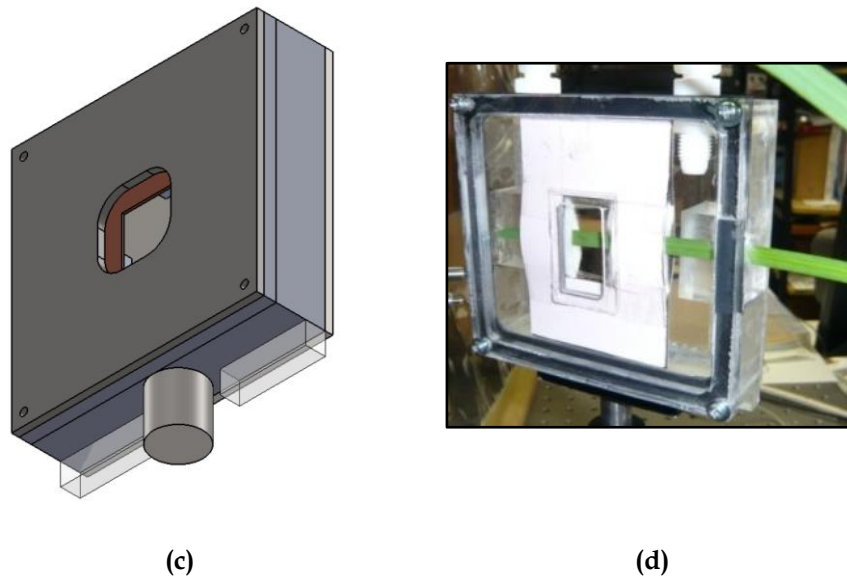
Figure 3.6. Leaf ozone chamber. (a) Design of back part of the chamber, (b) Design of the front part of the chamber, (c) Design of the whole chamber, (d) Actual leaf chamber in operation.

The O_3 exposure system (Figure 3.5) consists of air pump, charcoal filters (CF), an O_3 generator (OES 10A, Dylec Inc., Japan), an O_3 monitor (Model 1150, Dylec Inc., Japan), main O_3 chamber ($33.5 \times 33.5 \times 58$ cm^3). A specially designed (Figure 3.6) leaf O_3 chamber ($10 \times 10 \times 2$ cm^3), made up of plastics, was connected to the main O_3 chamber to facilitate scanning of the leaf. Generated O_3 was fed into the main O_3 chamber, and its concentration was precisely controlled by measuring the O_3 concentrations with the O_3 monitor and feeding the signal back to the generator. In O_3 exposure measurements, the O_3 generation system approximately took 9 minutes, 10 minutes, and 14 minutes to reach the set O_3 concentrations, 80ppb, 120ppb, and 240ppb, respectively. Such a way, the control system took approximately 9 minutes, 10 minutes, and 14 minutes to bring O_3 concentration to 0ppb from 80ppb, 120ppb, and 240ppb, respectively. The O_3 feedback control system practically could stabilize the concentration of O_3 within the leaf and main O_3 chambers at an accuracy of around 0.5% during the experiments.

69

Figure 3.7. Chinese chives plant which were grown in the growing chamber for expermental purposes.

Chinese chives plants were grown (Figure 3.7) in a growth chamber (Conviron, Controlled Environmental Ltd, Canada). We maintained the relative humidity at 55%-65%, and respective day/night cycle of 12/12 hours at a light intensity of 260-350μmolm^{-2}s^{-1}/ 0μmolm^{-2}s^{-1} and an air temperature of 25°C/18°C. The plants were regularly watered kept to acclimate to the environmental conditions. In the experiment, healthy young leaves of the plants, one to two weeks old, were employed and mounted in the leaf O$_3$ chamber. Three halogen lamps with the fiber optic light guides were used to illuminate the plant leaf with a light intensity of 500μmolm^{-2}s^{-1} during experiments.

3.1.3. Timing protocol and data acquisition
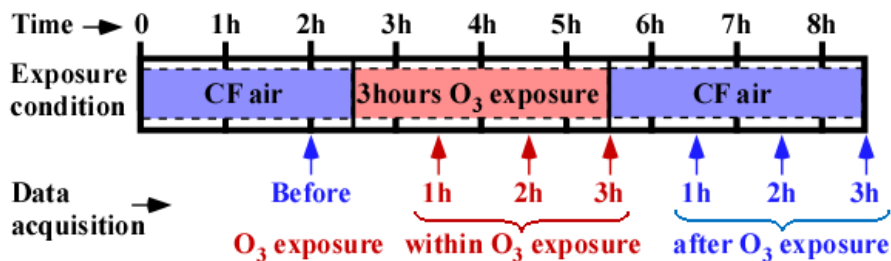
Figure 3.8. Timing protocol of O$_3$ exposure and data acquisition.

The experiments were carried out with the O_3 concentrations of 0, 80, 120, and 240ppb separately to investigate the influence of O_3 on Chinese chives. The entire experimental duration was 8.5 hours (Figure 3.8). As an initial condition, a continuous air flow (10 liter/min.) after passing the CF was fed into the leaf O_3 chamber, where the leaf is mounted, for two hours to achieve physical stability of the plant during the experimental period. For each O_3 exposure condition, next half an hour was allocated to reach desired (0, 80, 120, and 240ppb) O_3 concentration in the main O_3 chamber after starting the O_3 generator. However, leaf in the leaf O_3 chamber still received CF air. At the end of this half an hour period, tubes of the leaf O_3 chamber were arranged in such a way that, air containing O_3 with desired concentration will reach leaf without passing through the charcoal filter (CF). Then, the O_3 exposure was carried out for three hours. Same as above, end of 3hours of exposure, tubes of the leaf O_3 chamber were arranged to the early state, such that the leaf in the leaf chamber again received CF air for another 3hours. Same time O_3 generator was switched off. Final CF air treatment was done to monitor the response of leaf after the O_3 exposure. The O_3 concentrations of 120ppb and 240ppb were chosen based on the criterion used in Japan, where 120ppb for warning and 240ppb for serious warning for O_3 are issued in Japan. Meantime, 0ppb was chosen for control experiments. Both the temperature and the humidity were kept constant during a single session of experiment with respective variations, ±2% and ±1%. Measurements were performed at the position 5cm away from the apex of the leaf.

For the first approach of biospeckle signal analysis, OCT imaging data were acquired (Figure 3.8) sequentially, before, and at 1hour, 2hours, and 3hours after starting O_3 exposure (*within*), and at 1hour, 2hours, and 3hours after stopping of O_3 exposure (*after*). Same procedure was applied for the measurements on front and back surfaces of leaves separately with O_3

concentrations of 0, 80, 120, and 240ppb. Six experiments were performed for each condition.

For the second approach of fOCT biospeckle signal analysis, fOCT biospeckle signal data for diferent depth positions of the leaf were acquired sequentially, before, and at 1hour, 2hours, and 3hours after starting O_3 exposure (*within*), and at 1hour, 2hours, and 3hours after stopping of O_3 exposure (*after*). In here, to get time signals (biospeckles) from depth positions of a interested fixed lateral position, scanning mirrors were stopped at the corresponding angles with the help of developed software program. In these experiments too, line scan camera acquisition rate was set to be 25000 lines per seconds. Six experiments were performed under 240ppb O_3 exposure for six different Chinese chives leaves and data acquired at sixteen different lateral positions on those leaves.

3.1.4. Data analysis
3.1.4.1. Data analysis for first approach

Acquired spectral interference signal from line scan camera, was first transformed in to wave number (k) space from wavelength (λ) space (rescaling), and then, Fourier transformed in order to obtain the depth resolved reflectivity profile of the sample at the focal spot of the sample beam at a fixed lateral position of the scanning mechanism (A-scanning). While the scanning mechanism was swept or stepped the focused beam position across the sample, multiple A-scans were acquired and assembled in the computer into a two-dimensional cross-sectional image of the sample (B-scanning).

A certain interested potion of leaf image of the size 65×2500 pixels (223×4000 μm²) were chosen from the originally acquired cross-sectional image $I_{OCT}(x,y;t_i)$. Then, a fOCT biospeckle image $I_b(x,y;t_i)$ was obtained by

calculating the SD of the fOCT biospeckle signal at each and every point in the selected portion of the OCT cross-sectional image along the time axis (from the successively acquired OCT cross-sectional images) as given by,

$$I_{b(x,y;t_i)} = \left[\frac{1}{n} \sum_{j=1}^{n} \left\{ I_{OCT(x,y;t_{i+j})} - \langle I_{OCT(x,y;t_i)} \rangle \right\}^2 \right]^{\frac{1}{2}} \qquad (3.1)$$

where,

$$\langle I_{OCT(x,y;t_i)} \rangle = \frac{1}{n} \sum_{j=1}^{n} I_{OCT(x,y;t_{i+j})}$$
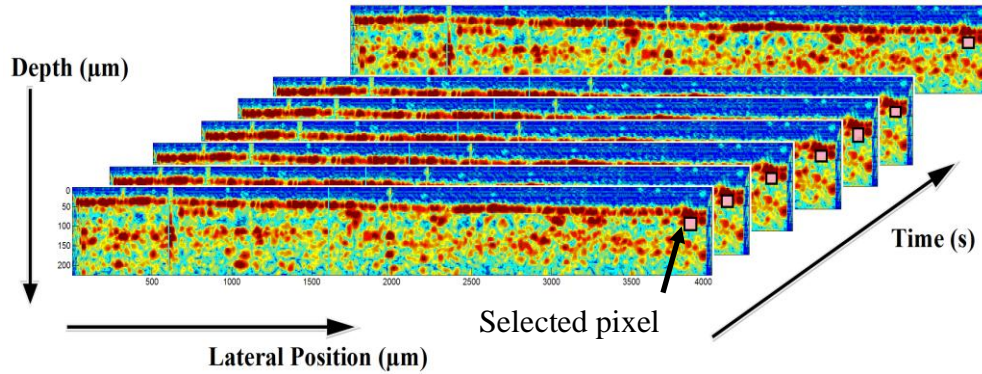
Figure 3.9. Successively acquired OCT cross-sectional images while a experiment for O₃ stress.
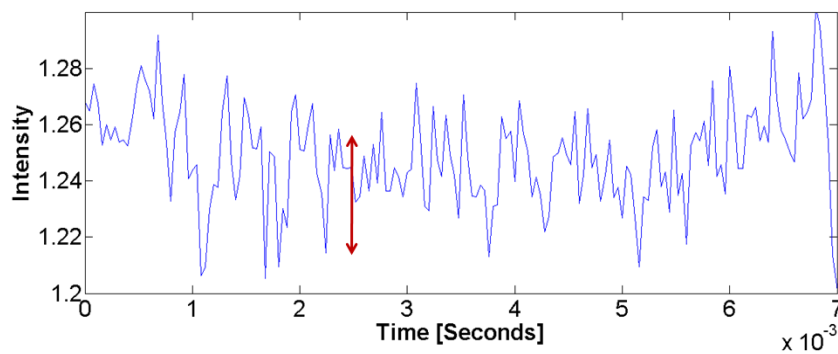
Figure 3.10. Intensity variation of selected pixel along time (same pixel of successivly aquired OCT images)

As an example, one pixel of OCT cross-sectional image, and same pixel of successively acquired images were selected shown in Figure 3.9. Intensity variation of that pixel with time was plotted (Figure 3.10). Then, SD of this time

signal calculated. This calculation was done for each and every pixel of the OCT cross-sectional image (Equation 3.1).

3.1.4.2. Data analysis for second approach

While the scanning mechanism was being stopped, Spectral interference signals were acquired for 1.2 seconds, giving us 25000×1.2 depth resolved reflectivity profiles at the same fixed lateral position. They were assembled in the computer into a two-dimensional image. This is a Time History OCT image that represents the variation, along the time, of a region from the OCT image of the leaf sample. Its rows represent different depth positions and the columns their intensities in a sequence of regularly spaced time steps (1/25,000 seconds). The activity of the sample appears as intensity changes in the horizontal direction, that is, along the rows.

By continuing data acquisition for 1.2 × 5 seconds, such a five number of time history OCT images were acquired. Power spectral densities of time signals were calculated for each and every depth position (along time axis) of five time history OCT images separately. To get higher signal to noise ratio (SNR), five power spectral densities corresponding to each depth position were averaged. Averaged of power spectral densities were used to calculate the autocorrelation functions at a certain depth position.

Here, the autocorrelation function is the correlation function calculated between two of the same signals with one delayed from the other by an increment τ of the independent variable time *(t)*. Autocorrelation obtained as a function of τ is a measure of the similarity of the signal with itself [2]. Let *I(t)* be time signal (intensity variation in time) of length *M*. The autocorrelation function can be defined as,

$$y(\tau) = \sum_{j=0}^{j=M-1} \left(I(t_j)I(t_j - \tau) \right) \tag{3.2}$$

When the correlation is normalized, its magnitude will range from 0 to 1. Autocorrelation function can be easily computed using a fast algorithm based on the convolution theorem, which can be expressed as follows,

$$y(\tau) = \sum_{j=0}^{j=M-1} \left(I(t_j)I(t_j - \tau) \right) = iFFT \left(I \times I^* \right) \tag{3.3}$$

Where *I* is the Fourier transform of *I(t)*, * means complex conjugation and *iFFT* stands for the inverse fast Fourier transform (FFT). Therefore, following three steps were done to calculate the autocorrelation function. We used Matlab (MATLAB R2009a, Mathworks, USA) computer software for calculations.

The *I(t)* was discrete Fourier transformed (*fft* function in Matlab),

Fourier transform of *I(t)* was multiplied *with* the its conjugated transform (power spectral density calculation),

The product was inverse discrete Fourier transformed (*ifft* function in Matlab).

The temporal variations of biospeckles were quantified by calculating CL (full width half maximum of the autocorrelation function) and it was employed to investigate the biological activities of different depth layers of the Chinese chives plant leaf against O3 stress. We expect, with the change in movements of scatters, CL of autocorrelation function would get altered due to temporal changes of the biospeckle signal.

3.2. Results and discussion

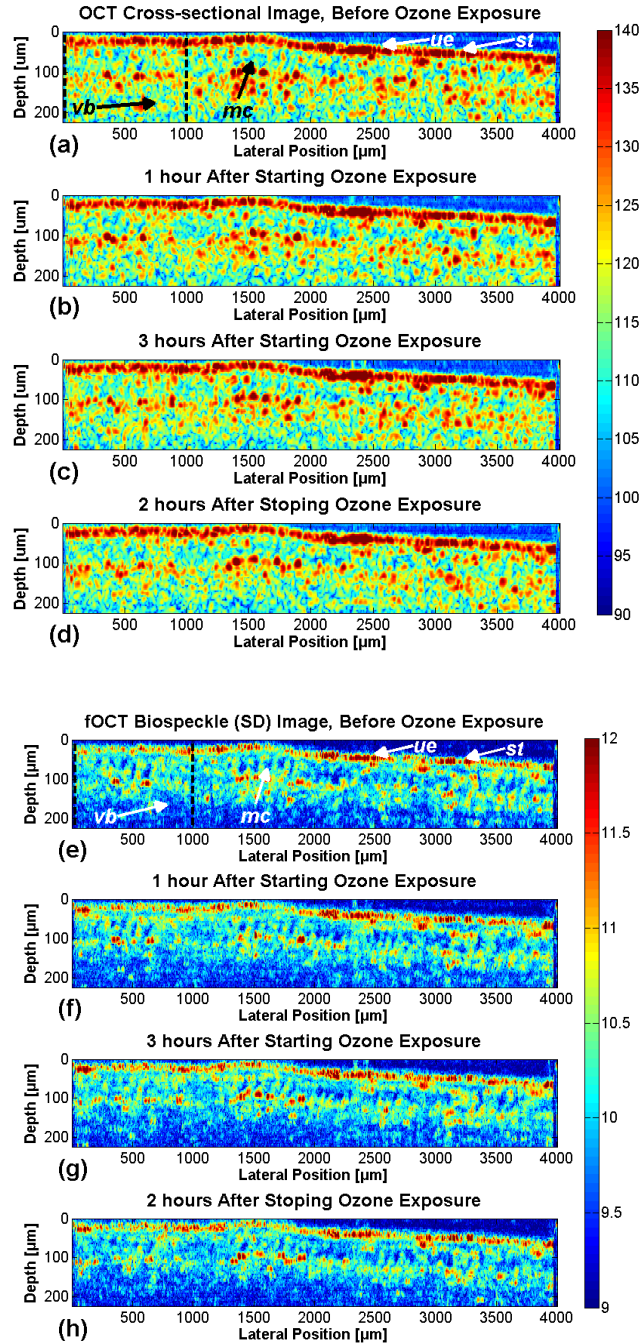## 3.2.1. Results and discussion of first approach

Figure 3.11. (a~d) Obtained conventional structural OCT cross-sectional images. (e~h) Corresponding fOCT biospeckle images. (a,e) Before exposure of O_3. (b,f) 1hour after starting exposure. (c,g) 3hours after starting exposure. (d,h) 2hours after stopping exposure. *ue*-upper epidemis, *mc*-mesophyll cell, *ve*-vesicular

76

bundle, *st***-stomata.**

Figures 3.11(a-d) show conventional structural OCT images of Chinese chives leaf (back surface) acquired before O_3 exposure, after starting exposure at 1, and 3 hours as well as after stopping exposure at 2 hours, while Figures. 3.11(e-h) represents corresponding fOCT biospeckle (SD) images. For our analysis, a certain lateral region (1000µm) was selected and laterally averaged in order to improve the SNR. Laterally averaged depth profile of selected region of conventional structural OCT images obtained under conditions of before, 1, and 3 hours after starting as well as 2 hours after stopping O_3 exposure are shown in Figure 3.12(a). Meanwhile Figure 3.12(b) shows corresponding depth profiles of the fOCT biospeckle images. Comparing the microscopic image in Figure 3.14(b), upper epidermal layer and the distinctive more oval shape mesophyll cells are clearly evident in the fOCT biospeckle image (Figure 3.11(e)). However, these features are not clear in conventional structural OCT image (Figure 3.11(a)). Vain area cannot be identified clearly both in fOCT and conventional OCT images. It may due to higher absorption and scattering in the leaf sample. However, around 100µm depth region can be seen clearly with the fOCT biospeckle images.
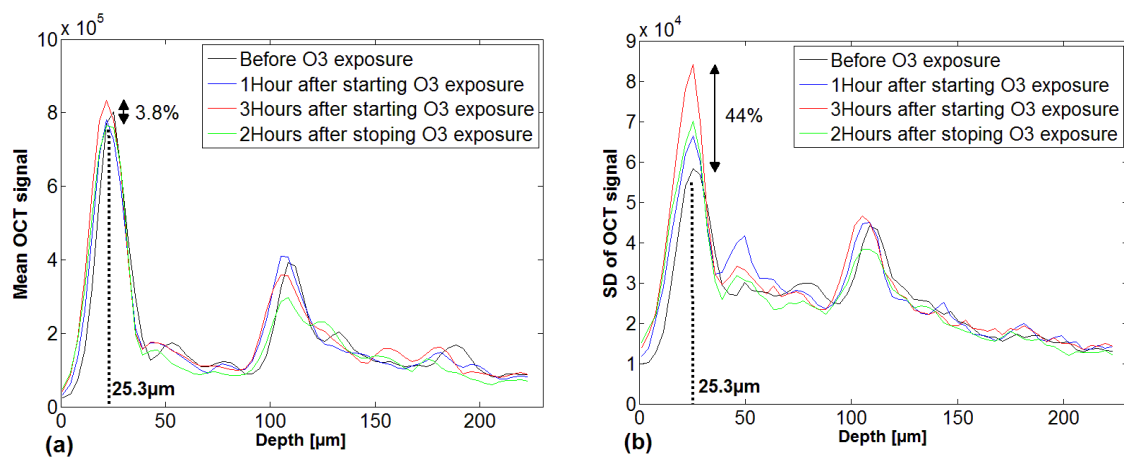

Figure 3.12. (a) Depth profiles of selected area of conventional structural OCT cross-sectional images. (b) Corresponding depth profiles of fOCT biospeckle images.

The difference in depth profiles of conventional structural OCT images at 25.3μm depth position that corresponds to the upper epidermal layer of the leaf, between before and after 3 hours of O_3 exposure is 3.8%. On the other hand, the corresponding values at the maximum of averaged depth profiles of fOCT biospeckle images were significantly increased to 44%. This variation in depth profiles of fOCT biospeckle images with O_3 exposure were clear for epidermal layer, since strong reflection could be seen from this layer. Therefore, the maximums of averaged depth profiles corresponding to the epidermal layer of fOCT biospeckle images at each time interval such as before, after starting and after stopping of O_3 exposure were used for further analysis in following discussion, since epidermal layer shows a large variation in averaged SD compared to other layers. However, earlier studies confirmed that of palisade mesophyll cells as main target of O_3 injury [3,4]. Due to strong reflection from epidermal layer and higher absorption in the leaf, changes in magnitudes (SD) of fOCT biospeckle signals from deeper layers were not significantly identified with such a short-term of O_3 exposure.

Focusing on the relative change in biospeckle signal coming from the plant leaf in response to O_3 exposure, the SDs of biospeckle signals at the epidermal layer (25.3μm depth position) were normalized by the SD_o of same layer of fOCT biospeckle image obtained before O_3. The normalized maximum SDs across six samples at 1, 2, and 3 hours after starting O_3 exposure (18 measurements) were averaged as *within* and at 1, 2, and 3 hours after stopping O_3 exposure (18 measurements) were averaged as *after* to obtain the averaged normalized standard deviation (ANSD) as given by,

$$ANSD = \langle SD/SD_o \rangle \tag{3.4}$$

where, $\langle\rangle$ denotes average over 18 measurements. The measurements were performed separately for back and front sides of the leaf, as shown in Figures

78

3.13(a, and b). The following discussion, the ANSD of biospeckle signal was used. Before and after O_3 exposure, plant leaves were treated with CF air for 2.5hours and 3hours respectively (Figure 3.8).
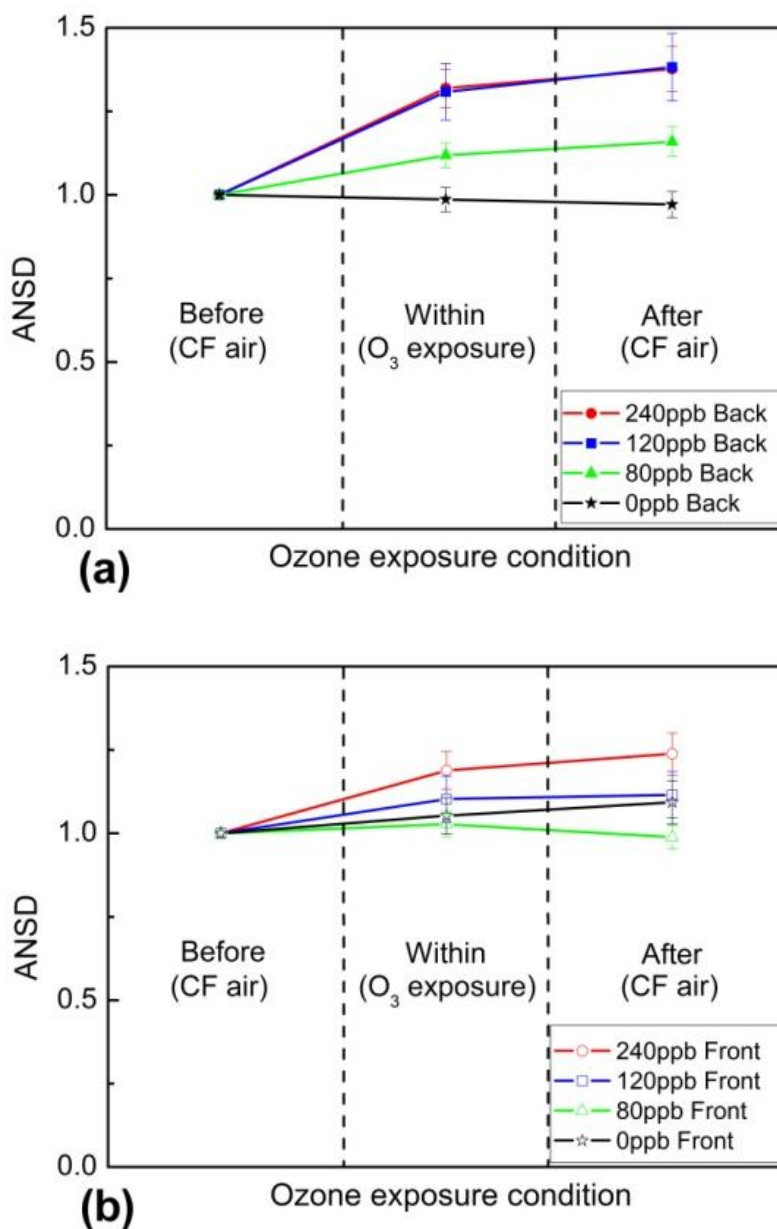

Figure 3.13. ANSDs of biospeckle signals of Chinese chives leaves under O_3 exposures of 0, 80, 120, and 240ppb. Each average value is plotted with standard error for 18 measurements. (a) from back surface. (b) from front surface.

Table 3.2. ANSDs of leaf back and front surfaces under O_3 exposures. Each value is mean±SD for eighteen measurements. The ANSD within O_3

exposure and after exposure were compared with that before exposure using statistical two samples t-test. (ns, not significant; ** $P < 0.01$).

O_3 concentration	Within exposure		After exposure (CF air)	
	Back surface	Front surface	Back surface	Front surface
240ppb	1.32 ± 0.24 **	1.19 ± 0.24 **	1.38 ± 0.29 **	1.24 ± 0.27 **
120ppb	1.31 ± 0.36 **	1.10 ± 0.29 ns	1.38 ± 0.43 **	1.12 ± 0.29 ns
80ppb	1.12 ± 0.16 **	1.03 ± 0.16 ns	1.16 ± 0.19 **	0.99 ± 0.15 ns
0ppb (CF air)	0.99 ± 0.15 ns	1.05 ± 0.23 ns	0.97 ± 0.17 ns	1.09 ± 0.28 ns

The temporal variations of ANSD of the biospeckle signal were examined for back surface as well as the front surface for O_3 exposure of concentrations 0, 80, 120, and 240ppb. It can be seen from the Figures 3.13(a, and b), the fluctuation becomes larger for both back and front surfaces as the concentration of O_3 becomes larger. Further, the ANSDs on back surface are larger than those on front surface. The ANSDs calculated for leaf back and front surfaces are shown in Table 1 and 2 respectively. In the case of leaf back surface, the differences in ANSDs between before (CF air treatment) and within O_3 exposure to 240, 120, 80ppb were significant (t-test, P < 0.01, Table 3.2). In addition, the differences in ANSDs between before and after O_3 exposure (CF air treatment after the exposure) for the same above concentrations were also significant (t-test, P < 0.01, Table 3.2).

For leaf front surface, the differences in ANSDs between before and within and also before and after O_3 exposure to 240ppb concentration were significant (t-test, P < 0.01, Table 3.2). However, the differences in ANSDs between before and within and also before and after O_3 exposure to 120, and 80ppb concentrations were not significant.

The differences in ANSD between the front and back surfaces (within and after O_3 exposure) for concentrations of 120ppb and 80ppb O_3 exposure are 26.7% and 13%, respectively. On other hand, the corresponding values for 240ppb O_3 exposure was reduced to13%. This may due to a saturation of the reaction for O_3 stress on plant back surface.

For the different response on the front and back sides of the leaf for O_3 exposure, the stomata may play a significant role since O_3 is taken up through the stomata and reacts with water and intercellular components to generate highly reactive oxygen species (ROS), that include peroxides and free radicals which are probably the real cause of the negative effect of O_3. Plants have a number of mechanisms that chemically and enzymatically remove these toxic compounds avoiding cellular damage [5-9]. O_3 stress affects the photosynthetic activity while altering leaf and root respiration rates [10] Therefore due to the higher fluctuation of the signal in the epidermal layer, stomata densities on both sides of the leaves were examined. Figure 3.14(a) shows a microstructural observation, number of stomata was counted within the circle having radius of 940µm, and the stomata densities were calculated. The stomata densities on the front and back sides of the leaf were 11.1±1.7 and 12.3±1.5, respectively. Therefore, a significant difference could not be found.

(a)   (b)
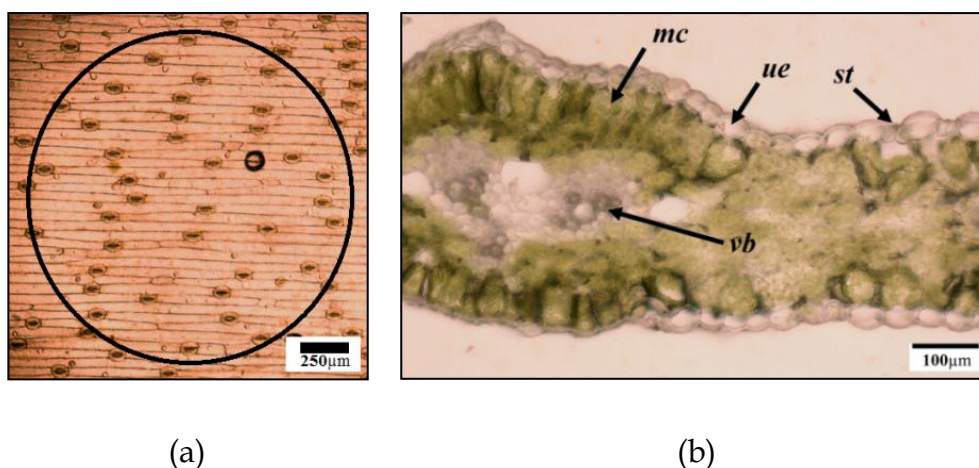
Figure 3.14. (a) Optical microscopy analysis for stomata on leaf back surface. (b) Optical microscopy analysis of cross-section of a leaf of Chinese chives. *ue*-upper epidemis, *mc*-mesophyll cell, *st*-stomata, *vb*-vascular bundle.

Meanwhile, leaf sections (across the leaf) were examined under a bright-field microscope. It was difficult to find a clear structural difference between front and back surfaces (Figure 3.14(b)). Moreover, the back surface of the leaf is

rougher and has a higher surface area than front surface. This may results in the difference in the total number of stomata on the front and back surfaces. In addition, stomatal conductances may be different on front and back surfaces. However, they are remained for our future research to be performed.

3.2.2. Results and discussion of second approach
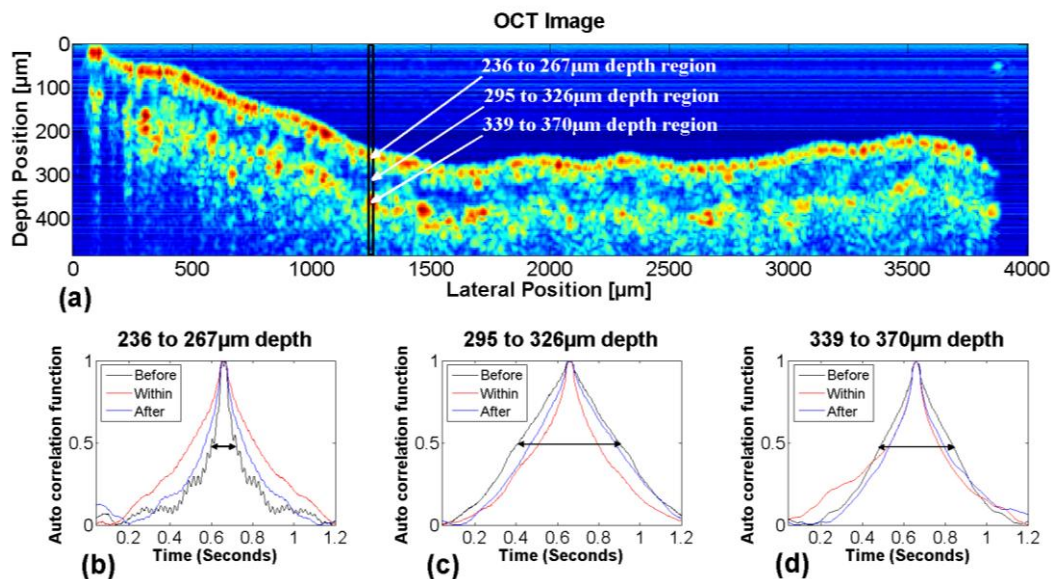
Figure 3.15. (a) OCT Image of leaf back surface. (b) Averaged autocorrelation functions, 236 to 267μm depth layer (epidermal layer). (c) Averaged autocorrelation functions, 295 to 326μm depth layer (mesophyll cell layer). (d) Averaged autocorrelation functions, 339 to 370μm depth layer (layer below the mesophyll cells).

Table 3.3. NCLs at different depth layers of the leaf.

Exposure condition	236 to 267μm depth layer	295 to 326μm depth layer	339 to 370μm depth layer
Before	1.00	1.00	1.00
Within O_3 exposure	2.58	0.70	0.57

After O₃ exposure	1.58	0.76	0.84

While OCT images of the leaf being captured (Figure 3.15(a)), galvano scanning mirrors were stopped at the corresponding angle to focus light beam at 1264µm lateral position. Interference signals were acquired and autocorrelation functions corresponding to each and every depth position were calculated. Out of different depth positions, 236 to 267µm depth region (epidermal layer), 295 to 326µm depth region (mesophyll cell layer) as well as 339 to 370µm depth regions (layer bellow mesophyll cells) were selected. Autocorrelation functions of different depth positions corresponding to each depth layer were averaged (along depth direction) separately. The autocorrelation function obtained for each depth layer at 1, 2, and 3hours within O₃ exposure were averaged as *within* and at 1, 2, and 3hours after exposure were averaged as *after* and drawn as shown in Figures 3.15(b,c, and d). Finally, to quantify temporal characteristics of bispecklel signals coming from different depth layers, CLs of biospeckle signals, corresponding to three different layers were calculated for before, within, and after O₃ exposure time intervals. Focusing on relative change in biospeckle signal coming from three different layers of the plant leaf in response to O₃ exposure, CLs of biospeckle signals, those of within and after O₃ exposure were normalized by the same obtained before exposure (CL₀).

Normalized correlation lengths (NCLs), corresponding to each time intervals of O₃ exposure were tabulated as shown in the Table 2. For 236 to 267µm depth region (epidermal layer), NCL was increased by 158% with the O₃ exposure. 63% recovery of CL to before level was seen after the O₃ exposure. For 295 to 326µm (mesophyll cell layer), NCL was decreased by 30% with O₃ exposure. 20% recovery of NCL to before level was seen after the O₃ exposure.

Meanwhile, as same as above mentioned region, 43% decreased of NCL was found after the O_3 exposure for the region of 339 to 370μm depth. However, it was a 63% recovery of CL after the O_3 exposure. Temporal characteristics of biospeckle signals were different layer to layer within O_3 exposure and after exposure.

Further, NCLs across 16 measurements from back surface of six different leaves of Chinese chives, before, within, and after exposure to O_3 were averaged separately to obtain averaged normalized correlation length (ANCLs) as given by,

$$ANCL = \langle CL/CL_o \rangle \qquad\qquad (3.5)$$

where, $\langle \rangle$ denotes average over 16 measurements. The following discussion, the NCLs of biospeckle signals, which were coming from different layers, were used (Figure 3.16). Three different layers, those on OCT image were compared with the leaf section in Figure 3.14(b).
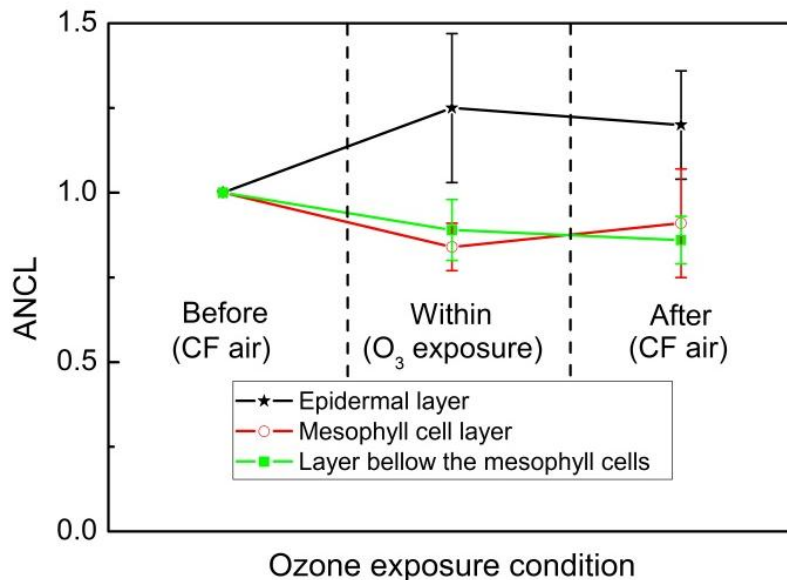

Figure 3.16. ANCLs of biospeckle signals coming from different layers (from back surface) of Chinese chives leaves under O_3 exposures of 240ppb. Each average value was plotted with standard error for 16

measurements.

Table 3.4. ANCLs of different layers of leaf (from back surface) under 240ppb O_3 exposure. Each value is mean±SD for 16 measurements. The ANCL within O_3 exposure and after exposure were compared with that before exposure using statistical two samples t-test. (ns, not significant; ** $P < 0.05$; * $P < 0.07$).

Layer	Within exposure	After exposure (CF air)
Epidermal layer	1.25 ± 0.89 ns	1.20 ± 0.64 ns
Mesophyll cell layer	0.84 ± 0.26 **	0.91 ± 0.63 *
Layer bellow the mesophyll cells	0.89 ± 0.35 ns	0.86 ± 0.27 *

For leaf mesophyll cell layer, the difference between ANCLs of before and within O_3 exposure of 240ppb concentration was significant (t-test, $P < 0.05$, Table 3.4). However, for epidermal layer and the layer bellow the meshophyll cells, the differences between ANCLs of before and within O_3 exposure were not significant even with significant level of $P < 0.07$ (t-test, $P < 0.07$, Table 3.4).

The difference between ANCLs of epidermal layer before and after the exposure was not significant (t-test, $P < 0.07$, Table 3.4). However, for mesophyll cell layer and the layer bellow the meshophyll cells, the differences between ANCLs of before and after O_3 exposure were significant with significant level of $P < 0.07$ (t-test, $P < 0.07$, Table 3.4).

Increase of CL, in other words slow temporal characteristic biospeckle activity in the epidermal layer could be seen within and after the O_3 exposure. Biospeckle characters were increased within and even after O_3 exposure in the mesophyll cell layer and the layer below mesophyll cells. The effect of O_3 stress appears more significantly in the mesophyll cell layer of the leaf for such a short term of O_3 exposure. For the different response on different layers, for O_3 exposure, the structural differences may play a significant role.

O₃ injury mainly occurs in the mesophyll cells whereas epidermal and stomatal cells and vascular cells resist until the last stage before total leaf necrosis. Inner cell wall thickening with cellulosic material frequently occurs, specially in palisade mesophyll cells in plant leaves. Earlier studies show that the inner and outer cell wall layer was generally thickened locally in outermost palisade mesophyll cells and irregular starch accumulation in bundle sheath, epidermal and guard cells could be seen in response to ozone stress [11].

3.3. Summary

We proposed, developed, and applied well the fOCT biospeckle imaging technique for monitoring O₃ stress on plants. The internal cell structure, specially mesophyll cell layer, within the Chinese chives leaf can clearly been seen in the fOCT biospeckle image, which is not clearly visible in conventional OCT cross-sectional image.

Due to strong reflection from epidermal layer, analysis for changes in magnitude of fOCT biospeckle signal was effective. In this study, we found that, epidermal layers of both surfaces of the leaf showed an increased fluctuation in biospeckle signal for the O₃ stress. Meanwhile, it showed a larger fluctuation against O₃ exposure on back side than those on front surface. These results indicate that the epidermal layer of back side of Chinese chives leaf is more sensitive to O₃ stress than the front surface.

However, analysis for magnitude of variation of biospeckle signal coming from more deeper layers, such as mesophyll cell layer, could not identify the changes with O₃ exposure. Our second approach, analysis for temporal characteristics of biospeckle signals coming from more deeper layers other than epidermal layer showed significant results with O₃ exposure. Temporal characteristics of fOCT biospeckle signal coming from mesophyll cell

layer were changed significantly with the O_3 exposure. Since the temporal characteristic of a signal is governed by its rate of change, changes in more deeper layers could be identified.

The presented study suggests possible applications of developed fOCT biospeckle imaging and signal analysis technique, for investigating the immediate impact of environmental factors, specially O_3 exposure, in very short span of time such as a number of seconds or a few minutes quantitatively and qualitatively, which is not possible with conventional experimental methods and even with conventional OCT imaging. Since the OCT images were successively acquired nondestructively in a non-contact manner, fluctuation monitoring will not affect the physiological activities of the plant. Therefore, the possible reason for the change in fluctuation is the O_3 exposure, since O_3 stress affects the photosynthetic activity of plants.

We presented an optical method that can be used for *in-vivo* studies of plants under environmental stresses. As a preliminary experiment we presented results from Chinese chives under O_3 stress. We could observe the different responses in different layers of the plant leaf which differs before, within, and after O_3 exposure for both leaf back and front surfaces under 0, 80, 120, and 240ppb O_3 concentrations.

References

1. Chow T H, Tan K M, Beng K N, Razul S G, Tay C M, (2009) "Diagnosis of virus infection in orchid plants with high resolution optical coherence tomography," Journal of Biomedical Optics 14(1), 014006.

2. Apicellaa B, Brunob A, Wangc X, Spinelli N, (2013) "Fast Fourier Transform and autocorrelation function for the analysis of complex mass spectra," International Journal of Mass Spectrometry 338, 30-38.

3. Vollenweider P, Ottiger M, Goerg M S G, (2003) "Validation of leaf ozone symptoms in natural vegetation using microscopical methods." Environmental Pollution 124, 101-118.

4. Faoro F, Iriti M, (2009) "Plant cell death and cellular alterations induced by ozone: Key studies in Mediterranean conditions," Environmental Pollution 157, 1470-1477.

5. Kangasjärvi J, Talvinen J, Utriainen M, Karjalainen R, (1994) "Plant defense systems induced by ozone," Plant Cell Environ. 17, 83–794.

6. Sharma Y K, Davis K R, (1997) "The effects of ozone on antioxidant responses in plants," Free Rad. Biol. Med. 23, 480–488.

7. Sandermann H, Ernst D, Heller W, Langebartels C, (1998) "Ozone: an abiotic elicitor of plant defence reactions," Trends Plant Sci. 3, 47-50.

8. Dizengremel P, (2001) "Effects of ozone on the carbon metabolism of forest trees," Plant Physiol. Biochem. 39, 729-742.

9. Angels C, Domingo J I, Manuel T, Eva B, (2003) "Effects of 2-month ozone exposure in spinach leaves on photosynthesis, antioxidant systems and lipid peroxidation," Plant Physiology and Biochemistry 41, 839-845.

10. Walter A, Schurr U, (2005) "Dynamics of Leaf and Root Growth: Endogenous Control versus Environmental Impact," Annals of Botany 95, 891-900.

11. Goerg M S G, Vollenweider P, (2007) "Linking stress with macroscopic and microscopic leaf response in trees: New diagnostic perspectives," Environmental Pollution 147, 467-488.

CHAPTER 4

4. Application of developed fOCT biospeckle signal analysis to monitor water stress on plants

In this study, we applied developed fOCT, based on biospeckle signal, to monitor the biological response of plants under water stress. In the experiments, two kind of series were conducted. In first series, one Japanese rice cultivar, namely Koshihikari plants were kept without watering for 6 days. OCT imaging data were acquired with, without 1, 2, 3, 4, 5, 6 days water at same area of same leaf of a plant. Six experiments were conducted for data analyzing purposes. In second series, another set of Koshihikari plants were kept without watering for 6 days. After 6 days, plants were watered while OCT imaging data were acquired at before, after 1, 30, 60, 90, 120, 150, 180 minutes of adding water (5 experiments under same condition). Effects to back side of the leaf were observed to validate the developed fOCT biospeckle imaging and signal analysis for functional changes inside the leaf against water stress. Functional OCT biospeckle signals were analyzed for their magnitude of fluctuation as well as for temporal characteristics.

4.1. Optical System and Method

4.1.1. Optical System

Optical system is same as described in the section 3.1.1.

4.1.1. Gas exchange meter

For measuring the net photosynthetic rate (A), stomatal conductance (g_s), sub-stomatal CO_2 (C_i), and transpiration rate (T) under light-saturated conditions, three plants were selected randomly of Koshihikari cultivar. Measurements were conducted with second leaf. During measurements of A, g_s and C_i, and T atmospheric CO_2 concentration, the air temperature and the photosynthetic photon flux density in leaf chamber were maintained at ambient, 25^0C and 500 µmol $m^{-2}s^{-1}$ respectively. The measurements of A, g_s and C_i were obtained before and after adding water.

4.1.2. Plant materials

Figure 4.1. Cultivating of rice plants in a growth chamber

91

This research was carried out from May 2010 to September 2011 in Saitama university. Thirty to forty days old Koshihikari rice cultivar was used (Figure 4.1). Cultivar was cultured under identical conditions. The culturing conditions were as follow:

The seeds of Koshihikari cultivar were pre-germinated in dark environment for four days.

1. Seedlings were transferred to separate plastic containers (600 ml volume cup) with two plants per container. Same soil containing the clay and humus and 0.02 g of N-P-K fertilizer in the respective ratio of 14:14:14 was used to fill the plastic containers up to half of the container. N-P-K fertilizer was used to obtain robust root and stable development.

2. The seedlings were placed in a growth chamber (Conviron, Controlled Environmental Ltd, Canada) for around three weeks. The conditions of the chamber were maintained to follow a 24 hour cycle with 12 hours for day time at light intensities of 260-350 μmol m^{-2} s^{-1} and 12 hours for night time with 0 μmol m^{-2} s^{-1}.

During the total experimental period of six months, air temperature was within 18°C – 25°C and the relative humidity was kept at 55%-65%. Both the temperature and the humidity were kept constant during a single session with respective variations, ±1% and ±2%.

4.1.1. Timing protocol and data acquisition

For the first experimental series, grown rice plants were taken from growth chamber and OCT imaging data were acquired. Scanned areas were marked and then, plants were again kept in the growth chamber. These plants were not watered anymore for 6 days. On the second day (one day without water), same OCT data acquisition procedure was carried out. Scan area was

same as the first day. Data acquisition was proceed for 1, 2, 3, 4, 5, and 6 days without watering.

For the second experimental series, grown plants were kept in the growth chamber without watering for 6 days. After 6 days, plants were taken from growth chamber and OCT imaging data were acquired named as before adding water. Then plants were watered and OCT imaging data were acquired at 1, 30, 60, 90, 120, 150, 180 minutes after adding water. Five experiments were performed in this series. Functional OCT biospeckle data aquisition was same as described in section 3.1.3.

4.1.1. Data analysis

Data analysis is same as described in section 3.1.4. Due to irregular cross-section of rice leaf, area within main vain was selected. Averages of marked squire areas of OCT and SD biospeckle images (Figure 4.2) were calculated and those were used for further analysis purposes.
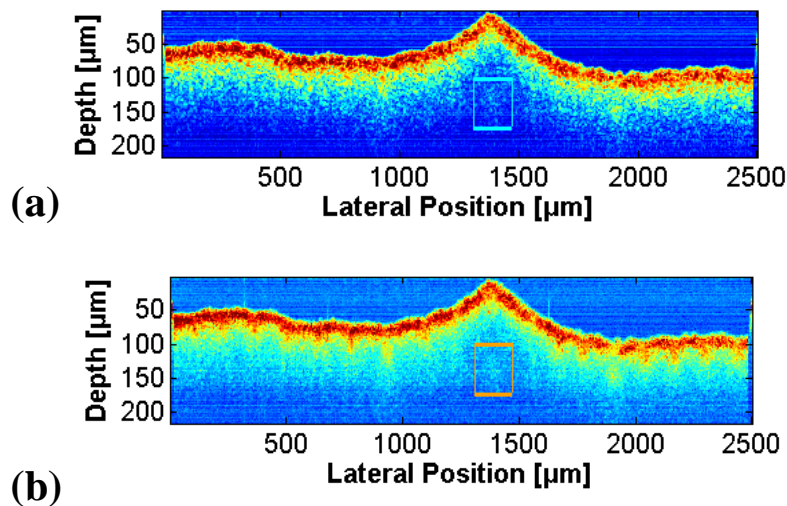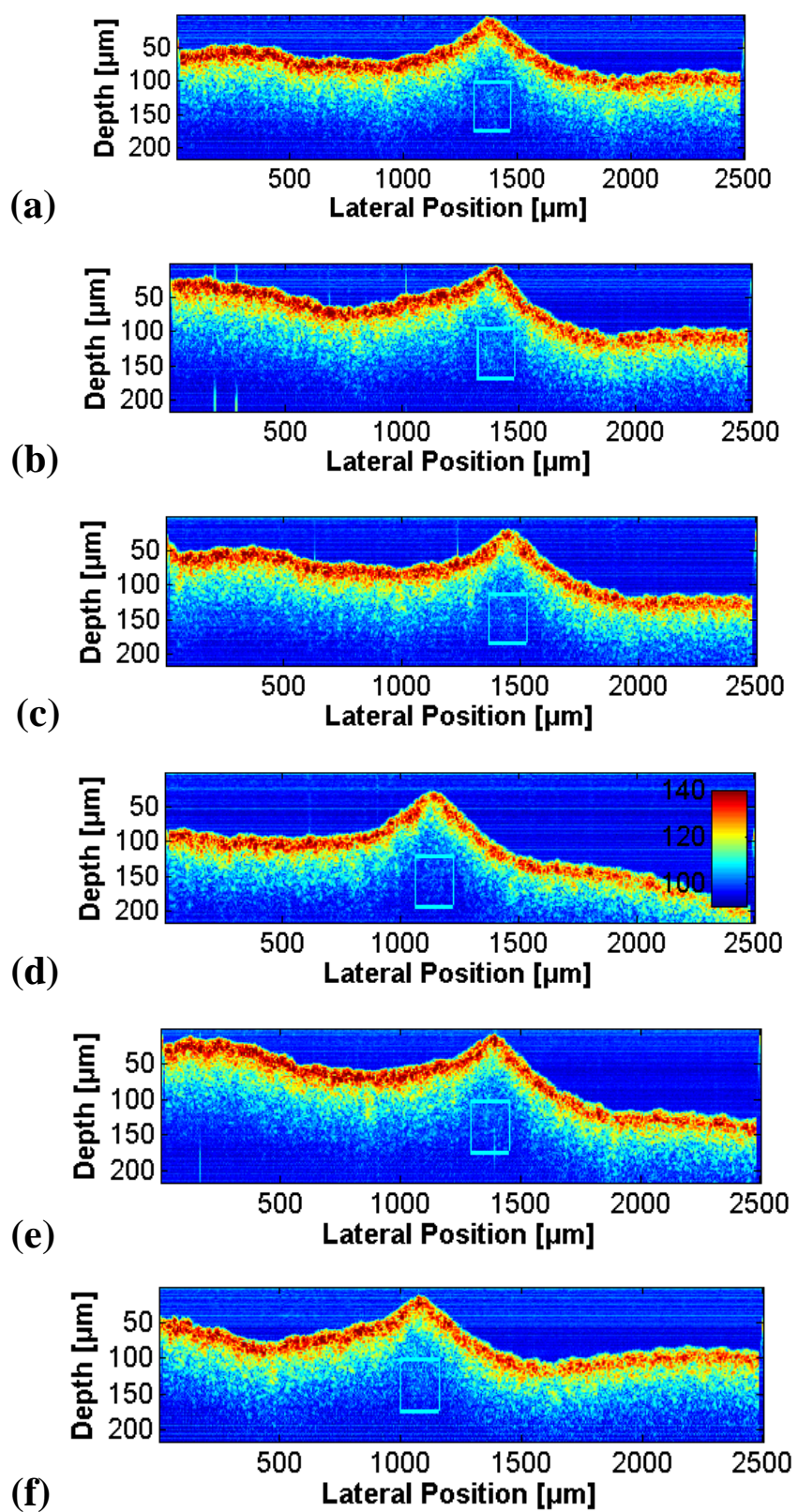

Figure 4.2. (a) OCT image, (b) Corresponding biospeckle image of rice leaf (from back side).

4.2. Results and discussion

(a)

(b)

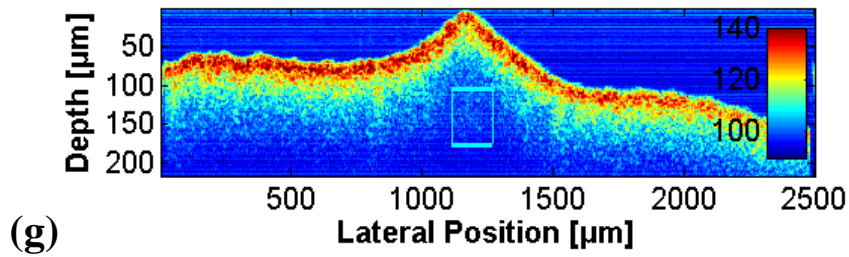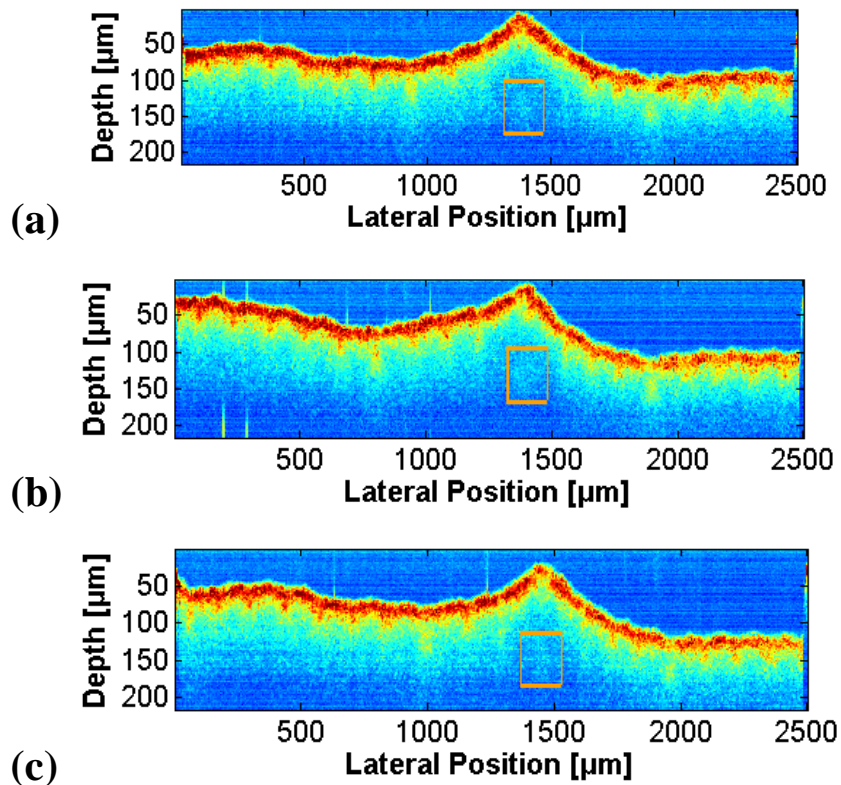**(c)**

(d)

(e)

(f)

(g)

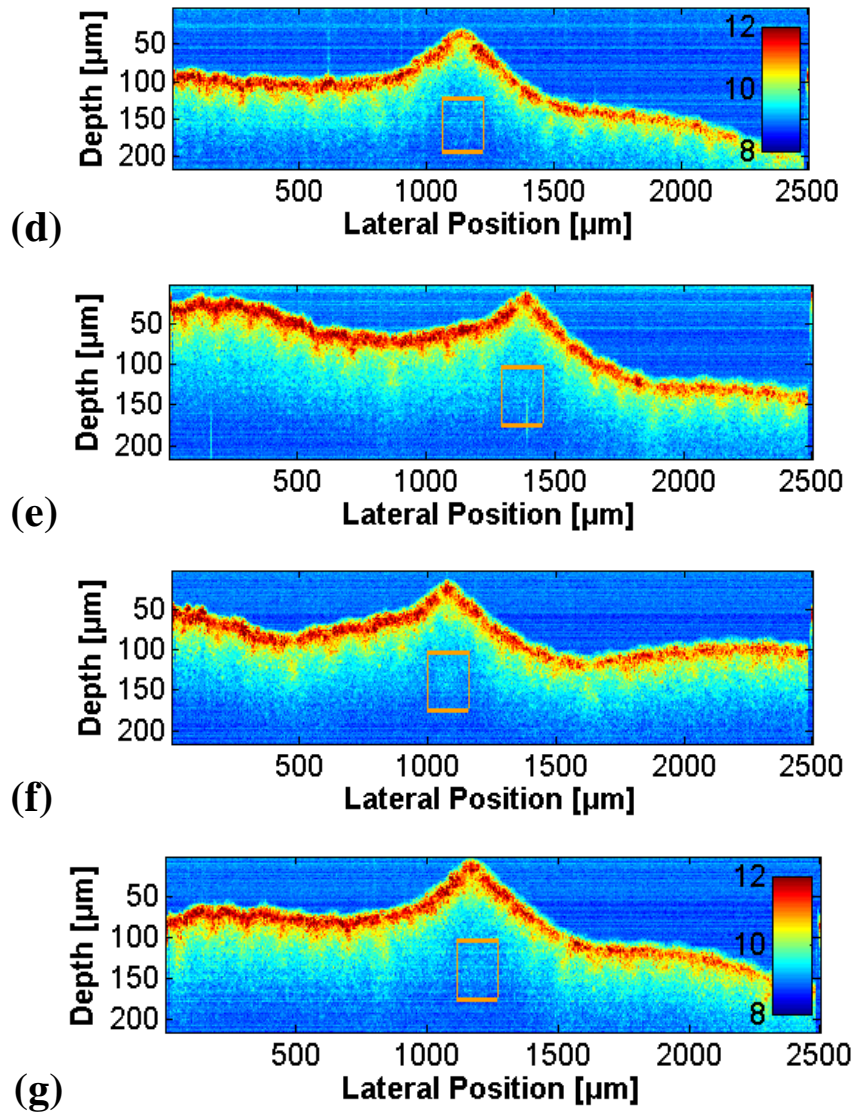**Figure 4.3. OCT images (a) With water, (b) 1 day without water, (c) 2 days without water, (d) 3 days without water, (e) 4 days without water, (f) 5 days without water, (g) 6 days without water.**

Figure 4.3 shows OCT images captured during one experiment. Special attention was given for the main vein are since it passes water in the leaf. Meanwhile Figure 4.4 shows corresponding biospeckle images. In here, a clear change could not be seen under water stress. However, small vein structure could be seen with biospeckle images.

(a)

(b)

(c)

(d)

(e)

(f)

(g)

Figure 4.4. Corresponding biospeckle images (a) With water, (b) 1 day without water, (c) 2 days without water, (d) 3 days without water, (e) 4 days without water, (f) 5 days without water, (g) 6 days without water.

For analysis purposes, averages (OCT image area)of marked areas of OCT images (with, without 1, 2, 3, 4, 5, 6 days) were normalizes by corresponding average of OCT image which was captured with water (1st day). Same way, averages (SD image area) of biospeckle images were normalized by corresponding average of biospeckle image which was captured with water. Further SD image area was divided by OCT image area (SD/Mean) for each instant.
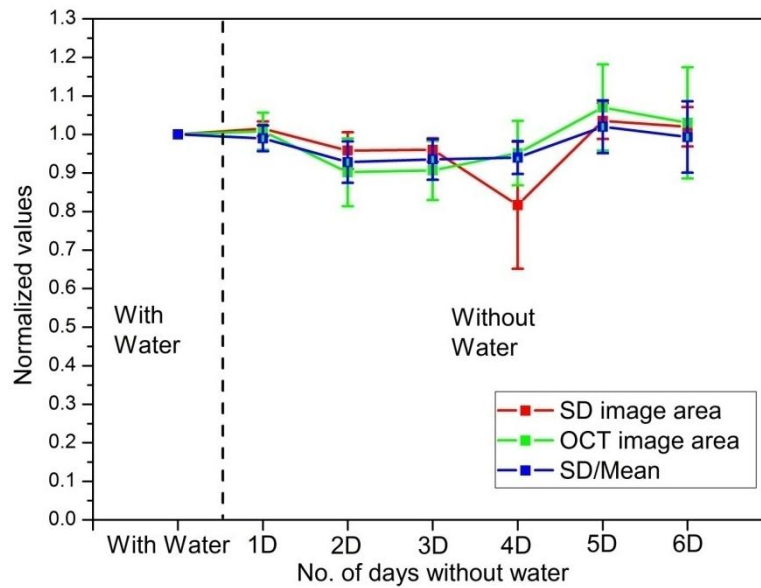
Figure 4.5. Variation of normalized average of marked area of OCT image, and biosprckle images.

Figure 4.5 shows normalized SD image area, OCT image area, and SD/Mean. However results do not show significant changes with water stress. Then, biospeckle signals were analyzes for their temporal charectoristics.

While OCT images of the leaf being captured (Figure 4.3), galvano scanning mirrors were stopped at the corresponding angle to focus light beam at main vein area (within marked area). Interference signals were acquired and autocorrelation functions corresponding to each and every depth position were calculated. Out of different depth positions, a 5µm depth region, and a 72µm depth region were selected. Autocorrelation functions of different depth positions corresponding to each depth region were averaged (along depth direction) separately. The autocorrelation function obtained for each depth region, with water, and without 1, 2, 3, 4, 5, 6 days of water were drawn. Finally, to quantify temporal characteristics of bispecklel signals coming from different depth layers, CLs of biospeckle signals, corresponding to three different layers were calculated. Focusing on relative change in biospeckle signal coming from three different layers of the plant leaf in response to water stress, CLs of

97

biospeckle signals, those of with and without 1..6 days of water were normalized by the same obtained with water (CL_o). Figure 4.6 shows a time history image of vein area.
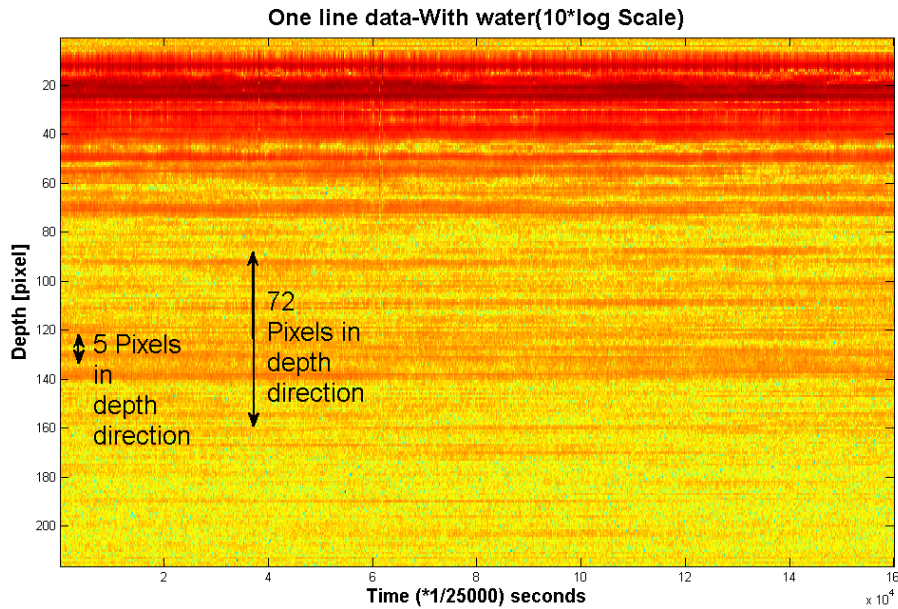

Figure 4.6. Time history image of vein area.

For analysis purposes, corresponding CLs with, and without 1, 2, 3, 4, 5, 6 days of water were normalizes by CL of with water (1st day). Same way, this procedure was applied separately for 5 pixels, and 72 pixels depth regions. We could not see a significant change in CL water stress for both 5µm, and 72 pixels depth regions. In this case too, we could not find a significant change in CL with water stress (Figure 4.7). However, when we used 72 pixels depth region for CL calculations, error was reduced (Figure 4.7).
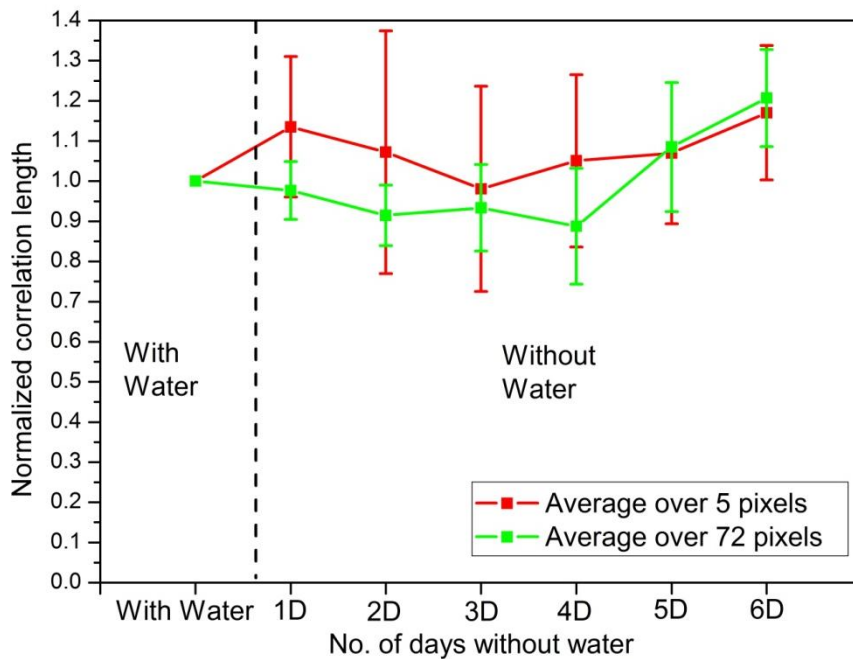
Figure 4.7. Variation of normalized CLs over 5 pixels, and 72 pixels (depth direction).

We could not see significant results against water stress. We kept plants in the chamber and brought them every day for OCT imaging. During this transportation, scanning area was slightly changed. So, it may be a one reason not to see significant changes.

We moved in to the second experimental series. Figure 4.8 shows OCT images captured during one experiment. In here too, special attention was given for the main vein area. Figure 4.9 shows corresponding biospeckle images. A clear change could not be seen with adding water to the plant. Small vein structure was seen clearly in biospeckle images.

(a)

(b)

(c)

(d)

(e)

(f)

(g)
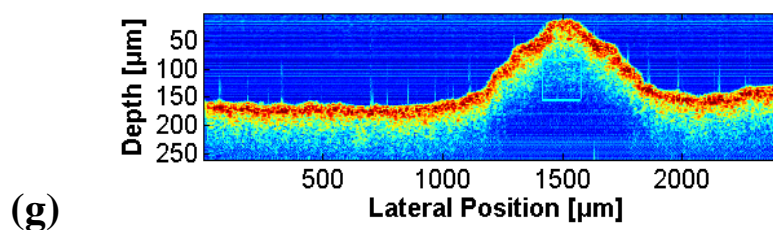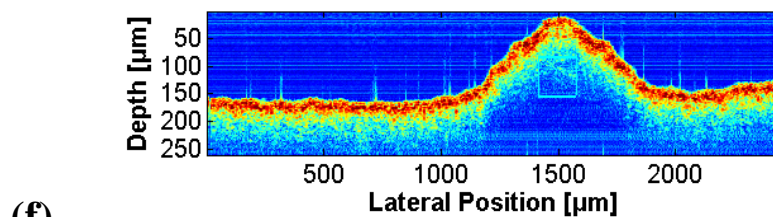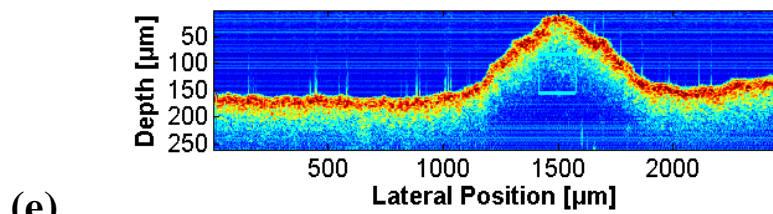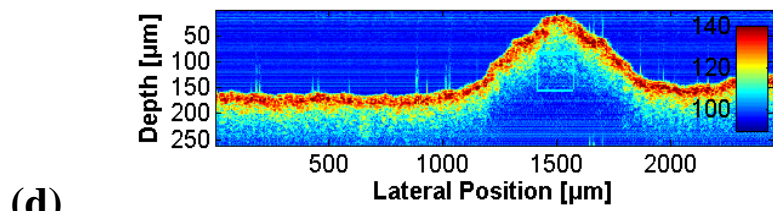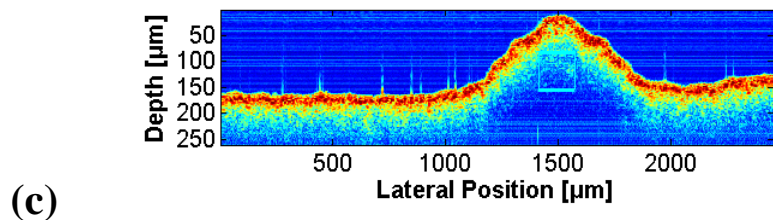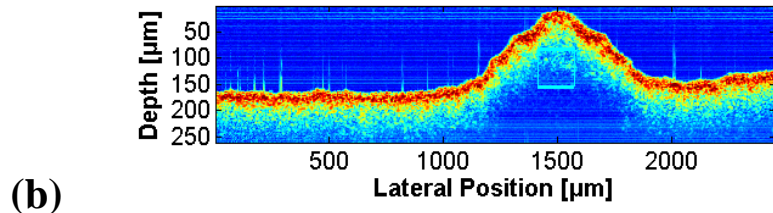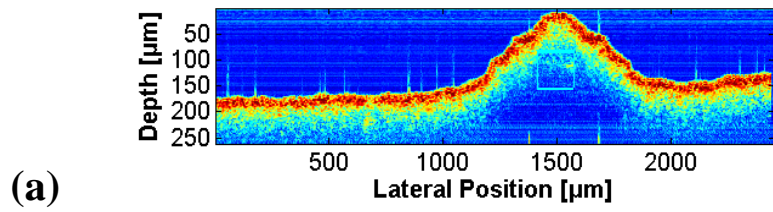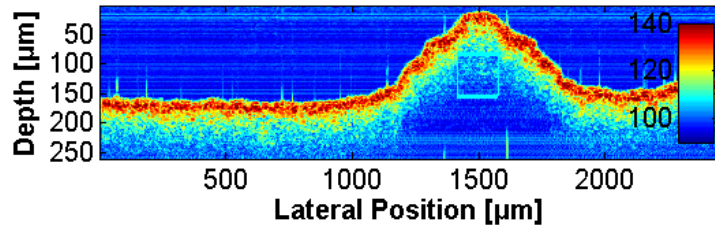
(h)

Figure 4.8. OCT images (a) Before adding water, (b) 1 Min after adding water, (c) 30 Min after adding water, (d) 60 Min after adding water, (e) 90 Min after adding water, (f) 120 Min after adding water, (g) 150 Min after adding water, (h) 180 Min after adding water.

(a)

(b)

(c)

(d)

101
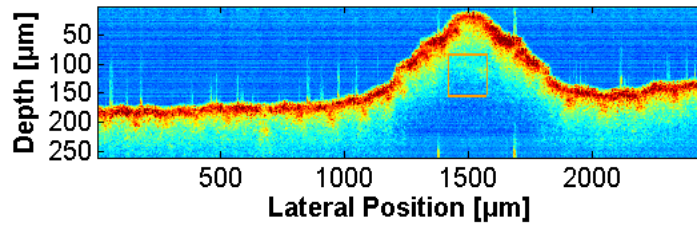
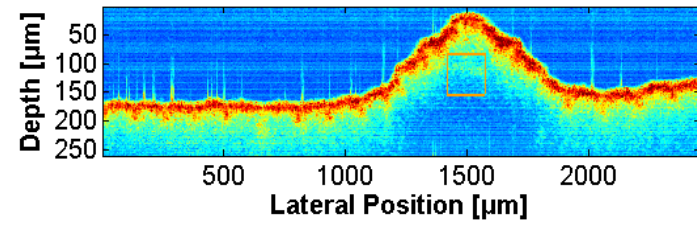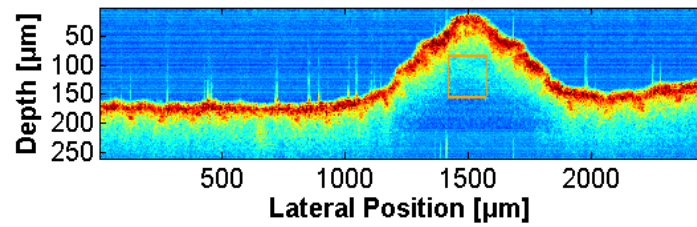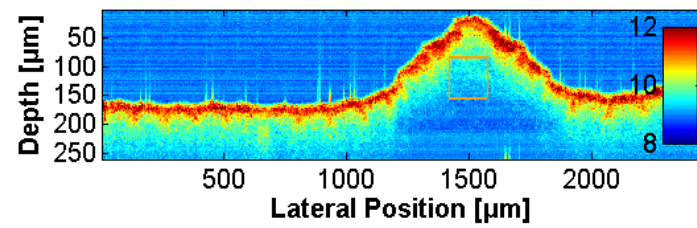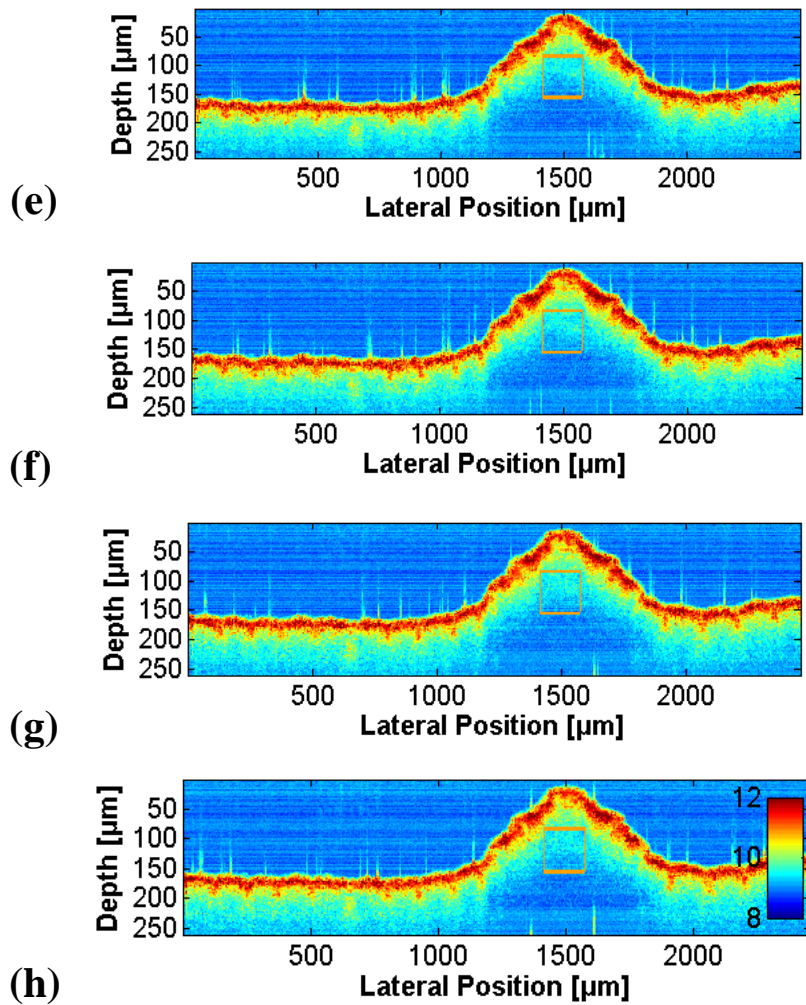**Figure 4.9. Corresponding biospeckle images (a) Before adding water, (b) 1 Min after adding water, (c) 30 Min after adding water, (d) 60 Min after adding water, (e) 90 Min after adding water, (f) 120 Min after adding water, (g) 150 Min after adding water, (h) 180 Min after adding water.**

In this series, we could capture OCT image of same area of the leaf, since plant was kept without water for 6 days initially and OCT imaging data were acquired while watering at 1, 30, 60, 90, 120, 150, 180 minutes. Figure 4.10 show experimental results over five replicas. Experimental results do not show significant changes while water coming to the plant.
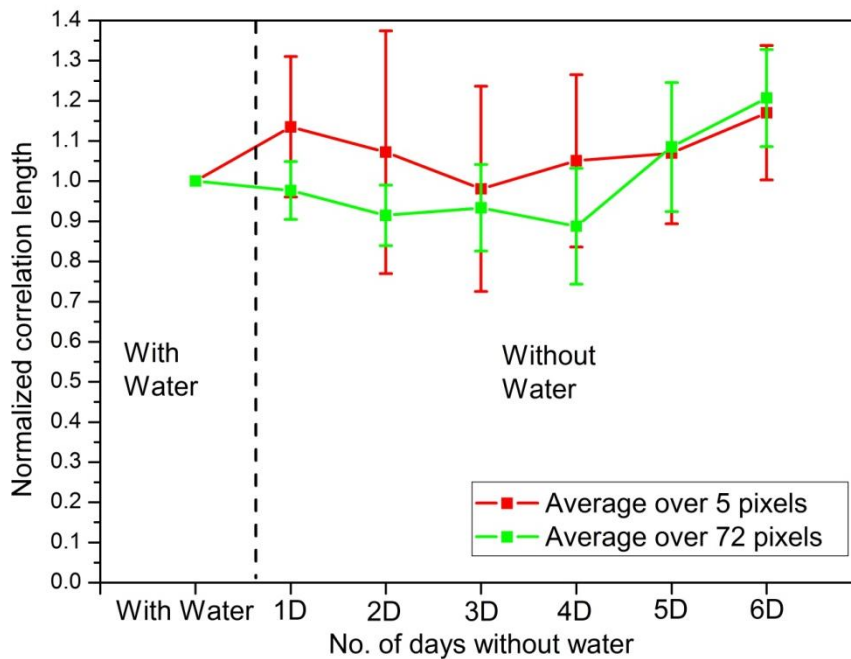
Figure 4.10. Variation of normalized average of marked area of OCT image, and biosprckle images.

Figures 4.11, 4.12, 4.13, and 4.14 show photosynthetic rate, stomatal conductance, sub-stomatal CO_2, and transpiration rate graphs received during one experiment with gas exchange meter. These results show that some change in those parameters can be seen after 325 minutes of adding water to the plant. Previous experimental series was conducted until 180 minutes of adding water. So, our next plant to continue experiments for long hours such as 6 to 8 hours after adding water.

103
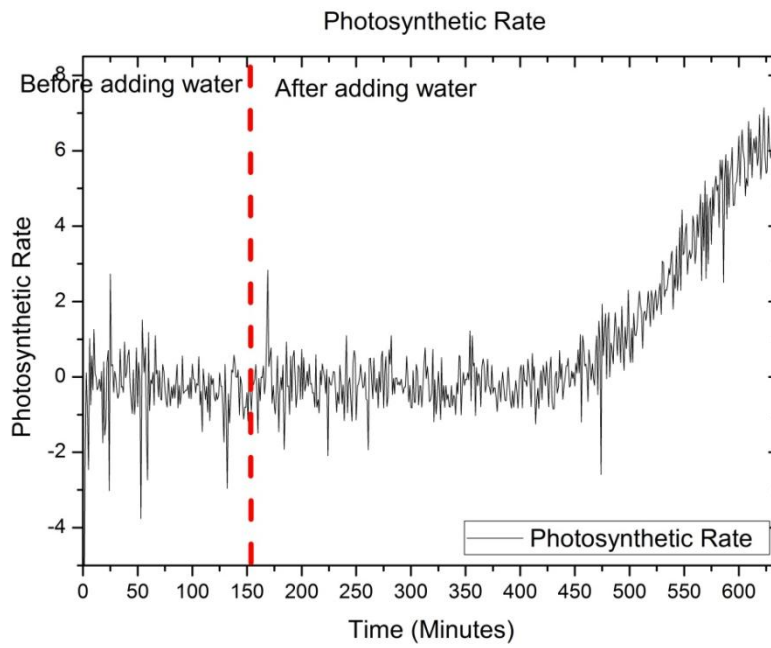
Figure 4.11. Photosynthetic rate before, and after adding water.
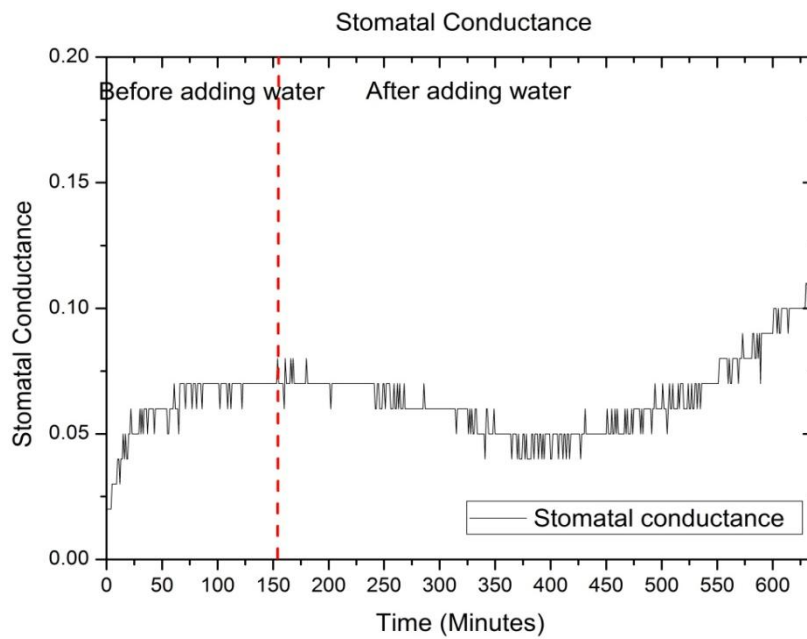
Figure 4.12. Stomatal conductance before, and after adding water.

104
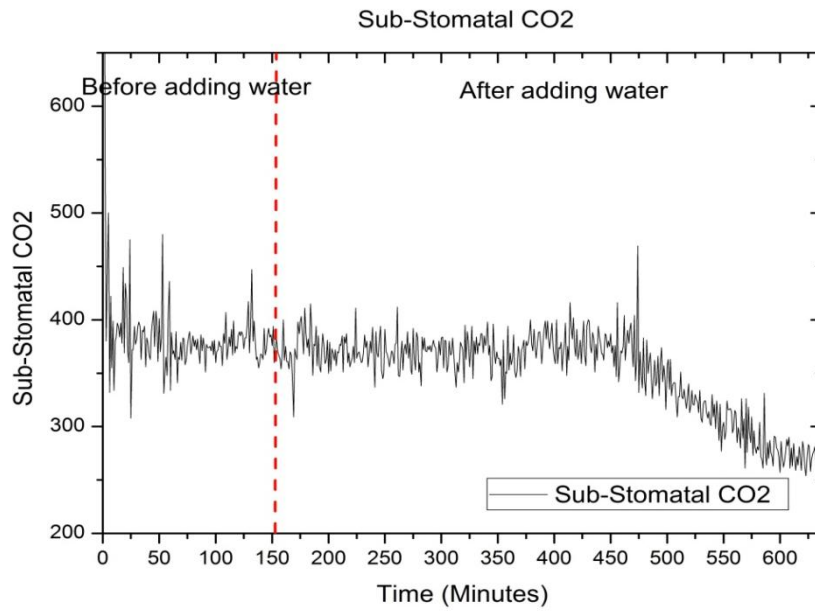
Figure 4.13. Sub-stomatal CO_2 before, and after adding water.
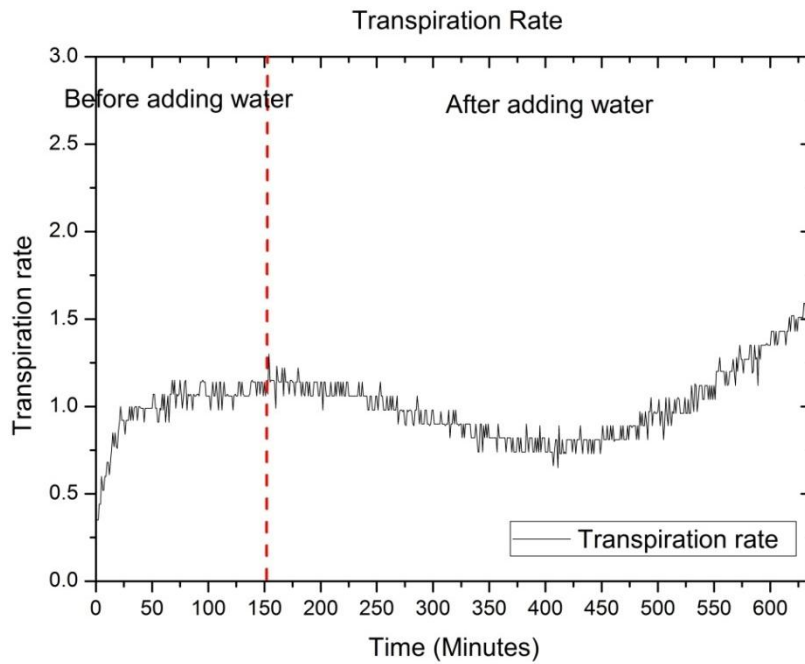
Figure 4.14. Transpiration rate before, and after adding water.

4.3. Summary

We proposed to use developed fOCT biospeckle imaging technique for monitoring water stress on plants. The vein structure, specially within the rice leaf could clearly been seen in the fOCT biospeckle image, which was not clearly visible in conventional OCT cross-sectional image.

However, analysis for magnitude of variation of biospeckle signal coming from main vein area, could not identify the changes with water stress even 180 minutes after adding water in the case of second experimental series. Our second approach, analysis for temporal characteristics of biospeckle signals coming from main vein area too did not show significant changes. However gas exchanges meter readings show changes after many hours (325 minutes) after adding water to the plant. Our future experiments will be conducted for many hours (over 5 hours) even after adding water.

CHAPTER 5

5. Conclusion and Future works

Biomass, height change, and counting are commonly employed techniques to monitor the effect of O_3 stress on plants [1]. Those require long waiting periods, and the changes in the internal structure of the plant cannot be recognized in real time. So, there is a need of fast and reliable method to assess the structural (i.e. functional) changes in plants against O_3 stress. The majority of methods for investigating internal structure of plants are invasive. They cause damage to the tissue under study, thereby limiting their application for *in-vivo* monitoring. An example of such a destructive approach is conventional optical microscopy which requires a destruction of the sample and a subsequent analysis, thus plants responses to external stress are inferred indirectly. In addition, the analysis cannot be performed in real time.

To overcome these limitations, we proposed to use optical coherence tomography (OCT). OCT [2,3] is an interferometric technique that detects internal reflected light and can provide non-contact two or three dimensional *in-vivo* tomographic images of the internal tissue structure with very high resolution of a few micrometers. It has generated numerous biological applications, most commonly in the fields of ophthalmology [4,5] and dermatology [6]. More recently, OCT has also been used in the field of botany to visualize the inner structure of tissue [7,8] and to study plants suffering from pathogen attack with conventional structural OCT imaging [9]. However, its potential in monitoring functional changes, in other words, biological activities inside tissue has not been well developed. In this study, we proposed to use

biospeckle signal to realize a functional OCT (fOCT) [10-12] to monitor the effect of O_3 on plants.

Processes such as cytoplasmic streaming, organelle movement, cell growth and division, and biochemical reactions are the biological activities occurring inside of plant leaf [13]. Behavior of these activities are changed under the influence of environmental stresses. We developed, and applied, proposed fOCT based on biospeckle to monitor the changes in biological activities of plants. Biospeckle is optical information that has been getting attention during last fifteen years for evaluation of properties of biological materials to monitor biological activities of plants [14].

The speckle pattern is generated by interference created by the backscattering of a random distribution of scatters at some distance from a scattering object under the illumination of a coherent light such as a laser. If there is no movement in scatters and no change in the structure of the object, the speckle pattern is stable in time. However, in the case of biological samples, the speckle pattern shows a dynamic property in time due to the moving organelles and particles within the sample. This dynamic speckle pattern is characteristic for biological tissues and has been called a biospeckle [15]. Therefore, the dynamic characteristics of the biospeckle can reflect the biological activities of a living substance [16].

To examine the fOCT biospeckles, OCT cross-sectional images were acquired successively over a certain period. Two different methods were used to analyze biospeckle signals coming from different spatial positions of the OCT cross-sectional image. In the first method, magnitude of the fluctuation of the biospeckle signal, in other words, standard deviation (SD) of the signal was calculated along the time axis for each spatial position from the data array of OCT cross-sectional images. Then, a fOCT biospeckle image was constructed

from the SDs of biospeckle signals. Magnitude (SD) of the time varying biospeckle signal reveal different biological information and it was proposed as a measure to evaluate the changes in biological activities against O_3 stress on plants.

In the second method, temporal characteristics of the biospeckle signals originating from different depths were analyzed. Averaged autocorrelation functions of fOCT biospeckle signals coming from layers at different depths of the leaf were calculated. From the correlation, half-width half maximum (HWHM) or the correlation length (CLs) was obtained. Longer CLs would indicate slower motion within the leaf and vice versa. Magnitude, SD, and temporal characteristics, CL, of the time varying biospeckle signal can reveal different information from those obtained by the conventional OCT, and they are proposed as measures to evaluate the changes in biological activities against O_3 stress on plants.

In the experiments, *Allium tuberosum,* commonly known as Chinese chives was exposed to different concentrations of O_3, and the effects to both back and front side of the leaf were observed to validate the developed fOCT based on biospeckle.

5.1 Conclusion

We proposed, developed, and applied the fOCT biospeckle imaging technique for monitoring environmental stress on plants well. The internal cell structure, specially mesophyll cell layer, within the Chinese chives leaf could clearly been seen in the fOCT biospeckle image, which was not clearly visible in conventional OCT cross-sectional image. Furthermore, internal vein structure, within the Koshihikari rice leaf could clearly been seen in the fOCT biospeckle image.

It was experimentally demonstrated that the influence of O_3 on each plant structure, e.g., epidermal and mesophyll cell layers, could be individually monitored even for short-term O_3 exposures. With O_3 exposure, variation of magnitude of biospeckle signal fluctuation coming from mesophyll cell layer could be visualized with more of the oval shaped mesophyll cells becoming unclear in contrast to the conventional OCT image. Due to strong reflection from epidermal layer, analysis for changes in magnitude of fOCT biospeckle signal was effective. In this study, we found that, epidermal layers of both surfaces of the leaf showed an increased fluctuation in biospeckle signal for the O_3 stress. Meanwhile, it showed a larger fluctuation against O_3 exposure on back side than those on front surface. Our experimental results indicate that the epidermal layer of back side of Chinese chives leaf is more sensitive to O_3 stress than the front surface.

However, analysis for magnitude of variation of biospeckle signal coming from more deeper layers, such as mesophyll cell layer, could not identify the changes with O_3 exposure due to averaging along lateral direction. Our second method, analysis for temporal characteristics of biospeckle signals coming from more deeper layers other than epidermal layer showed significant results with O_3 exposure. Since the temporal characteristic of a signal is

governed by its rate of change, changes in more deeper layers could be identified.

Increase of CL, i.e., slow fluctuation rate of biospeckle signal, in the upper epidermal layer could be seen within and after the O_3 exposure. In contrast, biospeckle fluctuation rate was increased within and even after O_3 exposure in the mesophyll cell layer and the layer below mesophyll cells. Analysis of the temporal characteristics of biospeckle signal coming from different layers could identify changes in biological activity with O_3 exposure. This study demonstrates that the direct exposure to O_3 affects differently the fOCT biospeckle signals coming from different layers of Chinese chives, even though the period of exposure O_3 is short, only a few hours.

Our study suggests possible applications of developed fOCT biospeckle imaging and signal analysis technique, for investigating the immediate impact of environmental factors. Specially for O_3 exposure, for a very short span of time such as a few hours, the proposed fOCT biospeckle was found to be effective which is not possible with conventional experimental methods and even with conventional OCT imaging. The fOCT based on biospeckle is found to be suitable for fast, non-destructive monitoring of environmental stresses on plants, which can potentially lead to significant time and cost saving, while conventional techniques require a destruction and subsequent analysis.

111

5.2 Future studies

The change in fluctuation of biospeckle coming from epidermal layer with O_3 exposure is a new discovery revealed from the fOCT technique. But, the biological phenomena causing this change in fluctuation is still unknown. Furthermore, the reason for different response from Chinese chive leaf front and back surface is unknown too. Therefore further studies required for understanding these things.

Apart from O_3 stress, other environment stresses such as CO_2, water, heavy metal stresses as well as plant types with genetics have to be studied with our new OCT technique.

The data question parameters such as line rate of camera, galvano-scanning mirror frequency, exposure time, number of frames used to generate SD (Biospeckle) image have to be studied further in future experiments.

References

[1]   Díaz-de-Quijano M, Schaub M, Bassin S, Volk M, Peñuelas J, (2012) "Ozone visible symptoms and reduced root biomass in the subalpine species Pinus uncinata after two years of free-air ozone fumigation," Environmental Pollution 169 250–7.

[2]   Huang D et al. (1991) "Optical coherence tomography," Science 254 1178–81

[3]   Fercher A F, (1996) "Optical coherence tomography," Journal of Biomedical Optics 1 157–73.

[4]   Drexler W, Morgner U, Ghanta R K, Kärtner F X, Schuman J S, Fujimoto J G, (2001) "Ultrahigh-resolution ophthalmic optical coherence tomography," Nature Medicine 7 502–7.

[5]   Wojtkowski M, Leitgeb R, Kowalczyk A, Bajraszewski T, Fercher A F, (2002) "In vivo human retinal imaging by Fourier domain optical coherence tomography," Journal of Biomedical Optics 7 457–63.

[6]   Gambichler T, Moussa G, Sand M, Sand D, Altmeyer P, Hoffmann K, (2005) "Applications of optical coherence tomography in dermatology," Journal of Dermatological Science 40 85–94.

[7]   Hettinger J W, Mattozzi M D L P, Myers W R, Williams M E, Reeves A, Parsons R L, Haskell R C, Petersen D C, Wang R, Medford J I, (2000) "Optical coherence microscopy. A technology for rapid, in vivo, non-destructive visualization of plants and plant cells," Plant Physiology 123 3–15.

[8]   Reeves A, Parsons R L, Hettinger J W and Medford J I, (2002) "In vivo three-dimensional imaging of plants with optical coherence microscopy," Journal of Microscopy 208 177–89.

[9]   Boccara M, Schwartz W, Guiot E, Vidal G, Paepe R D, Dubois A, Boccara A C, (2007) "Early chloroplastic alterations analysed by optical coherence

tomography during a harpin-induced hypersensitive response," The Plant Journal 50 338–46.

[10]   Maheswari R U, Takaoka H, Homma R, Kadono H and Tanifuji M, (2002) "Implementation of optical coherence tomography (OCT) in visualization of functional structures of cat visual cortex," Optics Communications 202, 47–5.

[11]   Maheswari R U, Takaoka H, Kadono H, Homma R, Tanifuji M, (2003) "Novel functional imaging technique from brain surface with optical coherence tomography enabling visualization of depth resolved functional structure in vivo," Journal of Neuroscience Methods 124 83–92.

[12]   Chen Y, Aguirre A D, Ruvinskaya L, Devor A, Boas D A, Fujimoto J G, (2009) "Optical coherence tomography (OCT) reveals depth-resolved dynamics during functional brain activation," Journal Neuroscience Methods 178 162–73.

[13]   Braga R A, Dupuy L, Pasqual M, Cardoso R R, (2009) "Live biospeckle laser imaging of root tissue," European Biophysics Journal 38 679–86.

[14]   Kurenda A, Adamiak A, Zdunek A, (2012) "Temperature effect on apple biospeckle activity evaluated with different indices," Postharvest Biology and Technology 67 118–23.

[15]   Aizu Y, Asakura T, (1996) "Trends in Optics," (San Diego: Academic Press) pp27–49.

[16]   Ansari M D Z, Nirala A K, (2013) "Biospeckle activity measurement of Indian fruits using the methods of cross-correlation and inertia moments," Optik 124 2180–86.